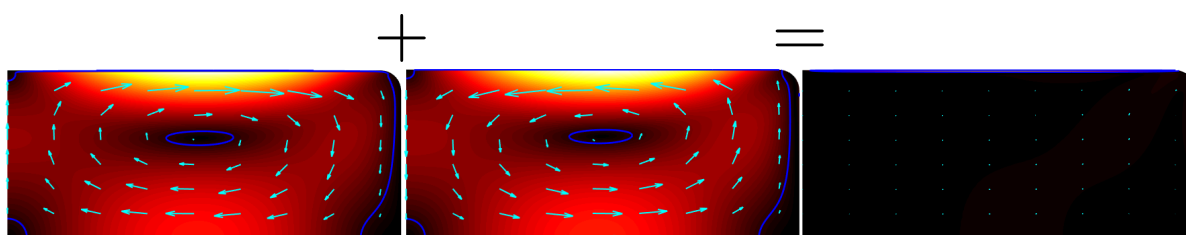Master thesis

Theoretical microfluidics: combined acoustic streaming and electroosmosis

Bjørn G. Winckelmann
s153418

Supervisor: Henrik Bruus

Department of Physics
Technical University of Denmark

25 June 2020

ii

Front page figure illustrates the combination of acoustic streaming and AC electroosmosis. This leads to an essentially vanishing steady streaming pattern in the fluid.

Abstract

Acoustofluidics offer label-free and gentle mechanical particle handling in micrometer sized fluid channels. This handling of particles by ultrasonic waves has been termed acoustophoresis. However, generation of standing acoustic waves in microchannels is accompanied by acoustic streaming. Larger particles are focused along pressure nodes or anti-nodes due to the acoustic radiation force from acoustic waves scattering off of them, while sub-micron particles typically get dragged around by the acoustic streaming. This will typically set a lower limit for the diameters of the particles available for acoustic handling.

The phenomena of electroosmosis is often used for pumping fluid through small channels in microfluidic systems. Under regular experimental conditions, electroosmotic streaming can reach amplitudes comparable to those of acoustic streaming. Furthermore, both phenomena are dominated by stresses, generated at the fluid/solid boundaries of the fluid channels. This leads to the question of whether or not electroosmosis could be used to control or suppress the streaming in acoustofluidic setups.

In this thesis, we analyse theoretically the capability of basic DC and AC electroosmosis to suppress typical acoustic streaming patterns. This is done through a series of analytical and numerical calculations. For the relatively simple phenomena of DC electroomosis, we suggest possible electrode geometries for effective streaming suppression. For the case of AC electroosmosis, a multi-mode approach is used to generate streaming patterns opposite to typical acoustic streaming in a simple fluid channel cross section.

Resumé

Akustofluidik tillader mærkningsfri og blid mekanisk manipulation af partikler i mikrometer størrelse væskekanaler. Denne håndtering af partikler med ultralydsbølger kaldes akustoforese. Generering af stående trykbølger i mikrokanaler vil dog altid medføre akustiske strømninger. Større partikler fokuseres langs tryknoder eller antinoder på grund af den akustiske strålingskraft genereret af akustiske bølgers brydning, imens partikler under en mikrometer i diameter typisk trækkes rundt af de akustiske strømninger. Dette sætter typisk en nedre grænse for diameteren af partikler, man kan håndtere akustisk.

Fænomenet elektroomose bliver ofte brugt til at pumpe væsker gennem små kanaler i mikrofluide systemer. Under almindelige eksperientielle forhold kan elektroomotiske strømninger opnå hastigheder, der er sammenlignelige med typiske akustiske strømningshastigheder. Endvidere domineres begge fænomener af spændinger, der genereres ved væskegrænsen i væskekanalerne. Dette leder os til spørgsmålet om, hvorvidt elektroosmose kan anvendes til at kontrollere eller undertrykke akustiske strømninger i akustofluide systemer.

I denne these analyserer vi teoretisk evnen af basal DC og AC elektroosmose til at undertrykke typiske akustiske strømninger. Dette gøres gennem en række analytiske og numeriske udregninger. For det relativt simple fænomen DC elektroomose foreslås mulige elektrodegeometrier til anvendelse af effektiv strømningsundertrykkelse. For AC electroosmose foreslås en multi-mode tilgang til at generere strømninger af modsat retning til typiske akustiske strømninger i et simpelt væskekanaltværsnit.

Preface

This master's thesis is submitted in partial fulfilment of obtaining the degree of Master of Science and Engineering in Physics and Nanotechnology at the Technical University of Denmark. The thesis corresponds to 30 ECTS points, and the work was carried out from February 2020 till June 2020 at the Department of Physics in the group of Theoretical Microfludics (TMF) headed by Professor Henrik Bruus.

I would like to thank my supervisor Professor Henrik Bruus for guiding me through not only the work presented in this thesis but my entire master's degree. A big thanks also goes out to past and present members of TMF whose previous work built a large part of the foundation for this project.

Bjørn G. Winckelmann
Department of Physics
Technical University of Denmark
25 June 2020

Contents

List of Figures

List of Tables

List of symbols

Symbol	Description	Unit/value
c_{fl}	speed of sound in fluid	m s^{-1}
c_α	concentration of ionic species α	m^{-3}
c_0	Bulk concentration of ions	m^{-3}
$C(u)$	Relative convergence parameter for the physical field u	
d_0	Wall displacement amplitude	m
$\boldsymbol{D}$	Electric displacement	C m^{-2}
D_α	Diffusivity of ionic species α	m^2 s^{-1}
e	Elementary charge	C
$\hat{\boldsymbol{e}}_i$	Unit vector i	
$\boldsymbol{E}$	Electric field	V m^{-1}
$\boldsymbol{f}_{\text{b}}$	Body force density	N m^{-3}
f	Frequency	s^{-1}
F	Source term	
i	Imaginary unit	
$\boldsymbol{J}$	Flux of field variable	
$\boldsymbol{J}_\alpha$	Flux of ion species α	m^{-2} s^{-1}
k_{B}	Boltzmann constant	J K^{-1}
$\hat{\boldsymbol{n}}$	Surface outward normal vector	
p	Pressure	N m^{-2}
$\boldsymbol{r}$	Position vector	m
$\boldsymbol{s}_0$	Equilibrium position of fluid channel wall	m
$\boldsymbol{s}_1$	First-order displacement of fluid channel wall	m
t	Time	s
T	Temperature	K
u	General field	
$\hat{u}_n$	n'th basis function for general field	
u_{ref}	Reference solution for general field	
$\boldsymbol{v}$	Velocity vector	m s^{-1}
Z_α	Valence of ionic species α	

β	Dimensionless viscosity ratio	
Γ_{fl}	Viscous damping factor	
ϵ_0	Vacuum permittivity	F m^{-1}
ϵ	Electric permittivity	F m^{-1}
η	Dynamic viscosity	Pa s
δ	Viscous boundary layer thickness	m
λ_{D}	Debye length	m
ν	Ionic concentration difference	m^{-3}
ν_0	Kinematic viscosity	kg m^{-1} s^{-1}
μ_α	Ionic mobility of species α	m^2 (V s)$^{-1}$
κ_{s}	Isentropic compressibility	Pa^{-1}
ρ	Mass density of fluid	kg m^{-3}
ρ_{el}	Electric charge density	C m^{-3}
ρ_0	Equilibrium mass density of fluid	kg m^{-3}
ζ	Wall potential	V
$\boldsymbol{\sigma}$	Cauchy stress tensor	N m^{-2}
σ_{el}	Electric surface charge density	C m^{-2}
ϕ	Electric potential	V
ω	Angular frequency	s^{-1}
∂_i	Partial derivative with respect to i	m^{-1}
$\boldsymbol{\nabla}$	Nabla or gradient operator	m^{-1}
$\boldsymbol{\nabla}\cdot$	Divergence operator	m^{-1}
∇^2	Laplace operator	m^{-2}
Ω	Computational domain	
$\partial\Omega$	Domain boundary	
$\langle\cdot\cdot\rangle$	Time-averaged	
$\perp$	Perpendicular to fluid channel boundary	
$\parallel$	Parallel to fluid channel boundary	
$\sim$	Similar to	
$\approx$	Approximately equals to	
$\propto$	Proportional to	
$\mathrm{Re}\{(\cdot)\}$	Real part of $(\cdot)$	
$\mathrm{Im}\{(\cdot)\}$	Imaginary part of $(\cdot)$	
$\mathcal{O}[(\cdot)]$	Of order $(\cdot)$	

1 | Introduction

1.1 Acoustofluidics

Acoustofluidics is a rapidly growing field of research based on the integration of acoustics and microfluidics in lab-on-a-chip designs. Acoustic waves are used for label-free and efficient particle handling with high bio-compatibility. The principle has found many applications within the field of biotechnology and healthcare, where many advances are based on the separation and purification of biological microparticles such as cells, viruses, bacteria, and microvesicles. Experimental applications include enrichment of circulating cancer cells [1], rapid sepsis diagnostics by detection of blood bacteria [2], seperation of lipids from blood [3], and many more.

System designs for particle migration by ultrasound, termed acoustophoresis, are usually based on elongated fluid channels with cross section dimensions of a few hundred micrometer. Acoustic waves with wavelengths comparable to the chamber dimensions are thus oscillating in the MHz regime. Piezoelectric transducers driven by AC sources are used to generate these high frequency waves through two main principles. The first principle is based on coupling into resonant vibrational modes of either the fluid channel or the entire microsystem. Here, the entire piezoelectric transducer is set into vibrations. This method of actuation is termed bulk acoustic waves (BAW). Another principle relies on interdigitated electrodes deposited on a piezoelectric substrate used to generate surface acoustic waves (SAW) that travel mainly along the surface of the material towards a fluid chamber placed on top. The method of actuation will not be a focus of this thesis, but the presented acoustics will mostly resemble that of a BAW design.

A typical strategy for BAW designs is to establish standing wave modes in the fluid channels. Whenever acoustic waves propagate in a fluid, acoustic streaming will inevitably follow from non-linear effects. In microchannels, the streaming is usually generated due to stresses in the fluid in a viscous boundary layer close the surface (so-called boundary driven streaming). A thorough and state-of-the-art study concerning the origins acoustic streaming has recently been conducted by Bach and Bruus [4, 5]. A sketch of a typical BAW design is shown in figure 1.1. Here, the pressure forms a standing half-wave along the width of the chamber. This pressure mode is accompanied by four streaming rolls in the bulk of the fluid generated from the top and bottom boundaries of the chamber. The acoustics presented in this thesis will follow this configuration.

Two competing forces of non-linear origin act on particles suspended in the fluid. One
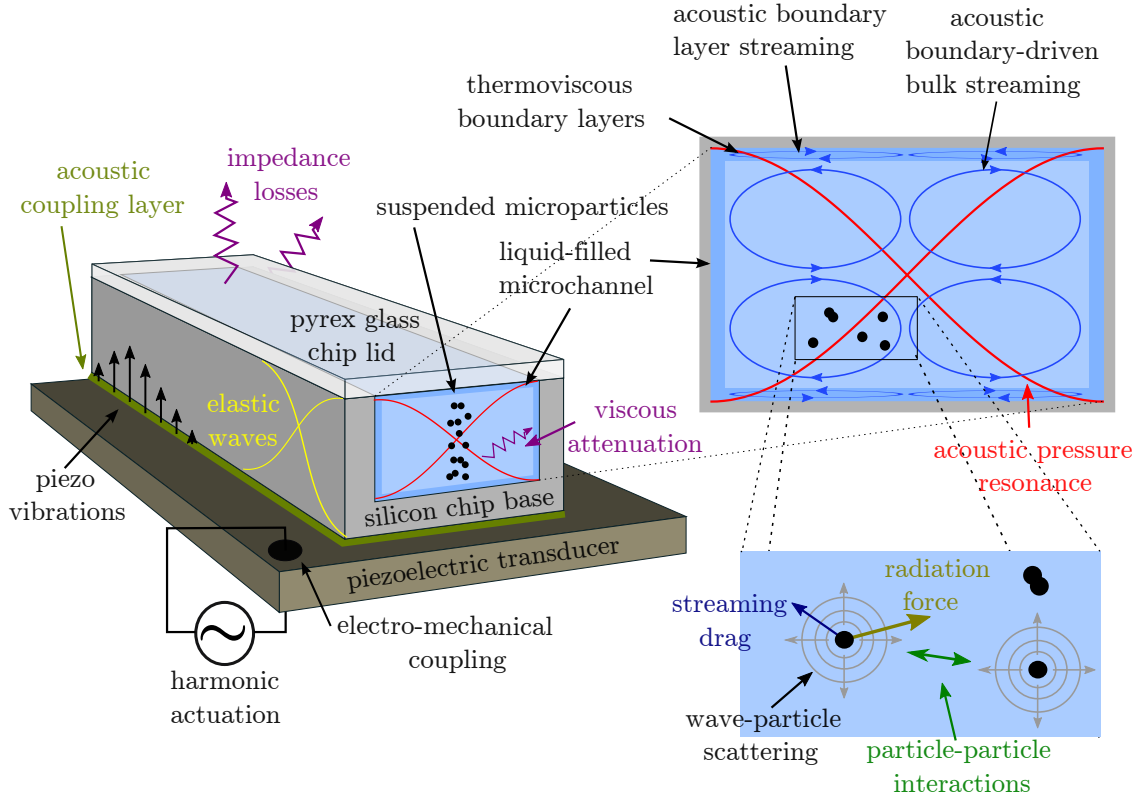
Figure 1.1: Conceptual drawing of an acoustophoretic device adapted from [6]. AC voltage is applied to a piezoelectric transducer, generating vibrations that travel into the microfluidic channel glued on top. This generates standing pressure waves accompanied by acoustic streaming, which is illustrated on a cross section of the channel. Both phenomena act on microparticles suspended in the fluid through the acoustic radiation force and the viscous drag force, respectively.

is the viscous Stokes drag from the acoustic streaming, which scales linearly with the particle radius a. This force typically causes the particles to swirl around the chamber. The other force is the acoustic radiation force caused by acoustic waves scattering off of the suspended particles. This force scales with the cube of the radius a^3, and it pushes the suspended particles towards pressure nodes or anti-nodes depending on their acoustical properties [7]. The motion of small particles, approximately below 1 μm, will typically be dominated by acoustic streaming due to the different scalings. For acoustophoretic devices, this is often undesirable because it counteracts the acoustic focusing of the radiation force. A key question of technological relevance becomes whether or not we can suppress this undesired streaming. This has directed our attention towards the well-known phenomena of electroosmosis.
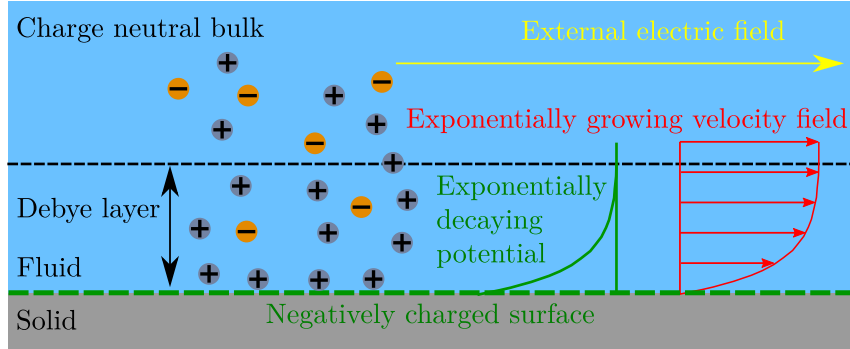
Figure 1.2: Conceptual drawing of electroosmosis. An ionic solution is present on top of a negatively charged surface. The negative surface charges draw positively charged ions towards the surface, which screen off the surface potential, resulting in a thin Debye layer with a positive electric charge density. An externally applied potential can be used to generate stresses in the fluid through this charge density. This generates an exponentially growing flow from the boundary.

1.2 Electroosmosis

The walls of a fluid chamber will usually become electrically charged due to surface reactions. If ions are suspended in the fluid, those of opposite sign to the surface charges will accumulate in a thin layer near the wall and screen out the potential from the surface charge. This layer is termed the Debye layer, and its width is typically of the order of nanometer. If an external electric field is applied parallel to the wall, the Coulomb force will act on the charge density, resulting in stresses in the fluid. These drive a flow from the Debye layer, which will extend into the bulk of the fluid. A conceptual drawing of electroosmosis is shown in figure 1.2

The surface charge can also be manipulated by external electrodes. This can either be done with AC or DC sources. The process of inducing stresses in the fluid by external AC sources is called induced charge electroosmosis (ICEO). Conventional electroosmosis based on the natural occurrence of surface charges as well as ICEO are typically used to create micropumps for lab-on-a-chip systems [8][9][10][11]. These pumps are very convenient as they deliver high pressures with no moving parts.

1.3 Motivation: combined acoustics and electroosmosis

In typical experimental setups, it turns out that electroosmotic flows and acoustic streaming are typically of the same order of magnitude $\sim 100\,\mu\mathrm{m/s}$. The desire to avoid acoustic streaming, and the similar boundary driven nature of the two flows, naturally raised the question of whether or not electroosmotic effects could be used to suppress acoustic streaming.

Extensive work on both phenomena has already been conducted in Professor Henrik

Bruus's group Theoretical Microfluidics (TMF). The main focus of this thesis is the electroosmotic flow and in particular, how it combines with acoustic streaming. As mentioned, electroosmotic flows can be generated by means of either DC or AC sources. Furthermore, different levels of non-linearities and model complexities can be—and have been—applied to the separate phenomena of electroosmosis. The goal of this thesis is not to exhaust a single model of electroosmosis but rather to make an overview of the two main principles (AC and DC), and how well they solve the stated problem of streaming suppression. Since author had prior knowledge of acoustics, there will be a predominant focus on electroosmosis in this thesis. Energy will be spend on understanding the basic theories of electroomosis, whereas acoustics is presented more as an overview. To our knowledge, this is the first study of electroosmosis for the purpose of acoustic streaming suppression. A review of the combination of acoustics and other microfluidic techniques for the purpose of particle handling can be found in [12], and a study focusing on the combination of acoustics with magnetophoresis is given in [13]. Other attempts at acoustic streaming suppression include geometric shape-optimisation [14] and the use of inhomogeneous fluids [15].

1.4 Outline of the thesis

Chapter 2: Theory
The general theories of fluid dynamics and electroosmosis are presented. The applied strategy for doing acoustofluidic calculations with viscous boundary layers is stated, and the theories of Debye layers and electroosmotic flows are outlined. Effective boundary layer theories for both phenomena are presented.

Chapter 3: Numerical simulations
The finite element method used in the commercial software COMSOL Multiphysics is summarised. Standard simulations of acoustics and electroosmosis are presented to illustrate the effective theories and basic but important points.

Chapter 4: Combined acoustics and DC electroosmosis
DC electroosmosis is combined with acoustic streaming. Several examples of streaming suppresion of increased realism are presented as proofs of concept. An optimisation algorithm is applied to determine effective designs. We discuss some disadvantages and experimental complications of the method.

Chapter 5: Induced-charge electroosmosis
The theory of AC, or induced charge, electroosmosis is presented. The theory is linearised, and an effective slip velocity for the linearised theory is derived. The effective boundary conditions are shown to circumvent numerical analysis of the thin Debye layer. The derived effective theory is then applied to analyse the generation of induced charge electroosmosis. A promising solution for streaming suppression is derived analytically and compared to numerics. Finally, the full non-linear phenomena is analysed numerically.

Chapter 6: Combined ICEO and acoustics
The combination of ICEO and acoustics is discussed, and the capability of ICEO to suppress acoustic streaming is evaluated briefly.

Chapter 7: Conclusion and outlook

2 | Theory

In this chapter, the theoretical framework of the thesis is presented. Several different theories are used to describe the complex microfluidic systems under consideration in this thesis. All of them have in common that we assume all underlying molecular dynamics to be smoothened out on the length scales of our interest. Instead, we will be considering average quantities of molecules and ions in small volume elements. With this, the macroscopic properties of fluids, solids, and electric polarisation are assumed to be perfectly continuous, which is known as the continuum hypothesis. Basic theories of fluid dynamics and electroosmosis are adopted from [16].

2.1 Fluid dynamics

Our fluid at the point r for time t is characterized by its mass density $\rho(r, t)$ and the velocity field $v(r, t)$. Assuming conservation of mass in an arbitrary but stationary volume element Ω in the fluid, leads to a local formulation governed by the continuity equation

$$\partial_t \rho + \boldsymbol{\nabla} \cdot (\rho \boldsymbol{v}) = 0. \tag{2.1}$$

In the same way, the conservation of momentum can be locally formulated through the Navier–Stokes equation. We will only consider Newtonian fluids such that

$$\partial_t(\rho \boldsymbol{v}) = \boldsymbol{\nabla} \cdot \boldsymbol{\sigma} - \boldsymbol{\nabla} \cdot (\rho \boldsymbol{v} \boldsymbol{v}) + \boldsymbol{f}_{\mathrm{b}}, \tag{2.2a}$$

$$\boldsymbol{\sigma} = \eta \big[\boldsymbol{\nabla} \boldsymbol{v} + (\boldsymbol{\nabla} \boldsymbol{v})^T \big] + \eta \big[(\beta - 1) \boldsymbol{\nabla} \cdot \boldsymbol{v} \big] \boldsymbol{I} - p \boldsymbol{I}. \tag{2.2b}$$

Here $p(r, t)$ is the pressure of the fluid, and $\boldsymbol{f}_{\mathrm{b}}$ is a body force density present in the fluid. This system of equations contains 4 equations and 5 independent fields (if the body-force is given). To close the system of equations, one usually assumes some constitutive relation between the pressure and the density

$$p = p(\rho). \tag{2.3}$$

2.2 Acoustofluidics

2.2.1 Pertubation theory

We will consider acoustic actuation of the microsystems presented in this thesis, where the systems are vibrated harmonically at a single frequency f. The physical fields governing

the fluid in the systems are split up in the following way. Initial zeroth-order fields describe the fluid in its steady state without external influences. First-order harmonic fields will establish in response to the actuation, and weaker—but still important—second-order fields arise due to the non-linear terms of the Navier–Stokes equation. Mathematically, this is formulated as

$$\boldsymbol{v}(\boldsymbol{r},t) = \boldsymbol{0}\ \ + \tilde{\boldsymbol{v}}_1(\boldsymbol{r},t) + \boldsymbol{v}_2(\boldsymbol{r},t), \tag{2.4a}$$

$$p(\boldsymbol{r},t) = p_0 + \tilde{p}_1(\boldsymbol{r},t) + p_2(\boldsymbol{r},t), \tag{2.4b}$$

$$\rho(\boldsymbol{r},t) = \rho_0 + \tilde{\rho}_1(\boldsymbol{r},t) + \rho_2(\boldsymbol{r},t), \tag{2.4c}$$

where the first-order fields denoted with $\sim$ are in phasor notation

$$\tilde{\boldsymbol{A}}_1(\boldsymbol{r},t) = \mathrm{Re}\left\{\boldsymbol{A}_1(\boldsymbol{r})\,\mathrm{e}^{-\mathrm{i}\omega t}\right\}, \qquad \omega = 2\pi f, \tag{2.5}$$

with $\boldsymbol{A}_1$ being the complex amplitude. Inserting Eq. (2.4) into Eq. (2.1) and Eq. (2.2) with no body force and keeping terms to first order, one finds the following equations for the spatial development of the first-order fields

$$0 = \boldsymbol{\nabla}\cdot\boldsymbol{v}_1 - \mathrm{i}\omega\kappa_s p_1, \tag{2.6a}$$

$$\boldsymbol{0} = \boldsymbol{\nabla}\cdot\boldsymbol{\sigma}_1 + \mathrm{i}\omega\rho_0\boldsymbol{v}_1, \tag{2.6b}$$

with the stress-tensor notation

$$\boldsymbol{\sigma}_k = \eta\left[\boldsymbol{\nabla}\boldsymbol{v}_k + (\boldsymbol{\nabla}\boldsymbol{v}_k)^T\right] + \left[(\beta-1)\boldsymbol{\nabla}\cdot\boldsymbol{v}_k\right]\boldsymbol{I} - p_k\boldsymbol{I}. \tag{2.7}$$

Here, we have defined the isentropic compressibility κ_s, which is a measure of the relative compression of the fluid per pressure under adiabatic conditions. This can be related to the speed of sound in the fluid c_{fl} through

$$\kappa_s = \frac{1}{\rho_0}\left(\frac{\partial\rho}{\partial p}\right)_s = \frac{1}{\rho_0 c_{\mathrm{fl}}^2}. \tag{2.8}$$

When keeping terms to second order, we will find terms with two multiplied first-order fields. We use that

$$\tilde{\boldsymbol{A}}_1(\boldsymbol{r},t)\tilde{\boldsymbol{B}}_1(\boldsymbol{r},t) = \frac{1}{2}\mathrm{Re}\left\{\boldsymbol{A}_1(\boldsymbol{r})\boldsymbol{B}_1^*(\boldsymbol{r})\right\} + \frac{1}{2}\mathrm{Re}\left\{\boldsymbol{A}_1(\boldsymbol{r})\boldsymbol{B}_1(\boldsymbol{r})\,\mathrm{e}^{-\mathrm{i}2\omega t}\right\}. \tag{2.9}$$

With this, the first-order fields constitute steady and second-harmonic driving terms for the second-order fields. The second-order fields are divided into two parts

$$\boldsymbol{A}_2(\boldsymbol{r},t) = \boldsymbol{A}_2(\boldsymbol{r}) + \mathrm{Re}\left\{\boldsymbol{A}_2^{(2\omega)}(\boldsymbol{r})\,\mathrm{e}^{-\mathrm{i}2\omega t}\right\}, \tag{2.10}$$

and equations for the separate components can then be found. The effects we are interested in happen on the timescale of several milliseconds, and the considered frequencies are in the MHz regime. Thus, we are only interested in the time-averaged second-order fields. Time-averaging over an oscillation period T is denoted by

$$\langle\boldsymbol{A}\rangle = \int_0^T \boldsymbol{A}\,\mathrm{d}t, \tag{2.11}$$

and the governing equations for the time-averaged second-order response can be written as

$$0 = \boldsymbol{\nabla} \cdot (\boldsymbol{v}_2 + \kappa_s \langle p_1 \boldsymbol{v}_1 \rangle), \tag{2.12a}$$

$$\boldsymbol{0} = \boldsymbol{\nabla} \cdot \boldsymbol{\sigma}_2 - \rho_0 \boldsymbol{\nabla} \cdot \langle \boldsymbol{v}_1 \boldsymbol{v}_1 \rangle. \tag{2.12b}$$

The applied boundary condition is the so-called no-slip condition, where the fluid is assumed to be strictly at rest with respect to the surrounding walls of solid. The rest position of the boundary between fluid and solid is denoted by $\boldsymbol{s}_0$, and the small harmonic displacement from equilibrium of the wall induced by the mechanical actuation is written as

$$\tilde{\boldsymbol{s}}_1(\boldsymbol{s}_0, t) = \operatorname{Re} \left\{ \boldsymbol{s}_1(\boldsymbol{s}_0) \, \mathrm{e}^{-\mathrm{i}\omega t} \right\}. \tag{2.13}$$

The no-slip boundary condition for an oscillating wall is then formulated as

$$\boldsymbol{v}(\boldsymbol{s}_0 + \tilde{\boldsymbol{s}}_1) = \partial_t (\boldsymbol{s}_0 + \tilde{\boldsymbol{s}}_1) = \operatorname{Re} \left\{ -\mathrm{i}\omega \boldsymbol{s}_1 \, \mathrm{e}^{-\mathrm{i}\omega t} \right\} = \operatorname{Re} \left\{ \boldsymbol{V}_1^0(\boldsymbol{s}_0) \, \mathrm{e}^{-\mathrm{i}\omega t} \right\}, \tag{2.14}$$

where $\boldsymbol{V}_1^0(\boldsymbol{s}_0) = -\mathrm{i}\omega \boldsymbol{s}_1$ has been introduced. Taylor expanding to second order yields the following boundary conditions for the first-order and the time-averaged second-order velocity fields

$$\boldsymbol{v}_1(\boldsymbol{s}_0) = \boldsymbol{V}_1^0(\boldsymbol{s}_0), \tag{2.15a}$$

$$\boldsymbol{v}_2(\boldsymbol{s}_0) = -\langle (\boldsymbol{s}_1 \cdot \boldsymbol{\nabla}) \boldsymbol{v}_1 \rangle \big|_{\boldsymbol{s}_0}. \tag{2.15b}$$

The boundary condition for the surrounding solid is continuous normal stress

$$\boldsymbol{\sigma}^{(s)} \cdot \hat{\boldsymbol{n}} = \boldsymbol{\sigma}_1 \cdot \hat{\boldsymbol{n}}, \tag{2.16}$$

with $\boldsymbol{\sigma}^{(s)}$ being the solid stress tensor. In this thesis, the motion of the surrounding solid will not be considered explicitly.

2.2.2 Effective boundary layer theory

The no-slip boundary condition causes the velocity of the fluid to abruptly go towards zero near the wall. It turns out that this happens in a thin boundary layer of lengthscale $\delta = \sqrt{2\nu_0/\omega}$, where $\nu_0 = \eta/\rho_0$ is the kinematic viscosity of the fluid. In the MHz regime, this viscosity dominated layer is of the order of $500\,\mathrm{nm}$ in water. For devices containing water channels with typical length scales of hundreds of micrometer, this layer poses a large computational task while doing numerical calculations. Following Bach and Bruus [4], the effects of the viscous boundary layer for slightly curved walls can be taken into account through effective boundary conditions on the physical fields in the bulk of the fluid. We introduce a local coordinate system at the wall through the capital letters (X, Y, Z), with X and Y being parallel to the boundary, and Z pointing into the fluid normal to the wall. We will also use $\parallel$ and $\perp$ to denote parallel and perpendicular with respect to the wall. To first order, the bulk of the fluid is described by the first-order pressure through

$$\nabla^2 p_1 + k_\mathrm{c}^2 p_1 = 0, \qquad \text{where} \quad k_\mathrm{c} = k_0 \left(1 + \mathrm{i} \frac{1}{2} \Gamma_\mathrm{fl} \right). \tag{2.17}$$

Here, $k_0 = \omega/c_{\text{fl}}$ is the ordinary wave number, and the viscous damping parameter Γ_{fl} is defined by

$$\Gamma_{\text{fl}} = (1 + \beta)\eta\kappa_s\omega. \tag{2.18}$$

The effective boundary condition on the first-order pressure field, which takes into account the effects of the thin viscous boundary layer, is given by

$$\partial_\perp p_1 = \frac{\mathrm{i}\omega\rho_0}{1 - \mathrm{i}\Gamma_{\text{fl}}}\left(V_{1Z}^0 - \frac{\mathrm{i}}{k_{\text{s}}}\boldsymbol{\nabla}\cdot\boldsymbol{V}_1^0\right) - \frac{\mathrm{i}}{k_{\text{s}}}\left(k_{\text{c}}^2 + \partial_\perp^2 p_1\right), \qquad \text{for} \quad \boldsymbol{r} = \boldsymbol{s}_0. \tag{2.19}$$

Here, we have defined the complex wavenumber

$$k_{\text{s}} = \frac{1 + \mathrm{i}}{\delta}. \tag{2.20}$$

The effective boundary condition on the solid stress is found to be

$$\boldsymbol{\sigma}^{(s)} \cdot \hat{\boldsymbol{e}}_Z = -p_1\hat{\boldsymbol{e}}_Z + \mathrm{i}k_{\text{s}}\eta\left(\boldsymbol{V}_1^0 + \frac{\mathrm{i}}{\omega\rho_0}\boldsymbol{\nabla}p_1\right). \tag{2.21}$$

Physical fields are split into the sum of a boundary layer field denoted by the superscript δ and a bulk field denoted by d. Furthermore, fields evaluated at the equilibrium position of the wall $\boldsymbol{s}_0$ are denoted with the superscript 0. The second-order acoustic bulk-streaming turns out to be well described by an incompressible Stokes flow with a slip velocity.

$$0 = \boldsymbol{\nabla}\cdot\boldsymbol{v}_2^{\text{d}}, \tag{2.22a}$$

$$\boldsymbol{0} = -\boldsymbol{\nabla}\left[p_2^{\text{d}} - \langle\mathcal{L}_{\text{ac}}^{\text{d}}\rangle\right] + \eta\nabla^2\boldsymbol{v}_2^{\text{d}} + \frac{\Gamma_{\text{fl}}\omega}{c_0^2}\langle\boldsymbol{S}_{\text{ac}}^{\text{d}}\rangle, \tag{2.22b}$$

$$\boldsymbol{v}_2^{\text{d}}(\boldsymbol{s}_0) = \boldsymbol{v}_{\text{slip}}^{\text{ac}}. \tag{2.22c}$$

Here, we have defined the fields

$$\langle\mathcal{L}_{\text{ac}}^{\text{d}}\rangle = \frac{1}{4}\kappa_s|p_1|^2 - \frac{1}{4}\rho_0|\boldsymbol{v}_1^{\text{d}}|^2, \qquad \langle\boldsymbol{S}_{\text{ac}}^{\text{d}}\rangle = \frac{1}{2}\text{Re}\left\{p_1\boldsymbol{v}_1^{\text{d}}\right\}. \tag{2.23}$$

$p_2^{\text{d}} - \langle\mathcal{L}_{\text{ac}}^{\text{d}}\rangle$ can be regarded as an effective pressure, and $\boldsymbol{f}_{\text{ac}} = \Gamma_{\text{fl}}\omega\langle\boldsymbol{S}_{\text{ac}}^{\text{d}}\rangle/c_0^2$ is an acoustic body force. We describe the slip velocity parallel to the boundary $\boldsymbol{v}_{\parallel,\text{slip}}^{\text{ac}}$ and the perpendicular component $v_{Z,\text{slip}}^{\text{ac}}$ by

$$\boldsymbol{v}_{\parallel,\text{slip}}^{\text{ac}} = (\boldsymbol{A}\cdot\hat{\boldsymbol{e}}_X)\hat{\boldsymbol{e}}_X + (\boldsymbol{A}\cdot\hat{\boldsymbol{e}}_Y)\hat{\boldsymbol{e}}_Y, \tag{2.24a}$$

$$\boldsymbol{A} = -\frac{1}{2\omega}\text{Re}\left\{\boldsymbol{v}_1^{\delta 0*}\cdot\boldsymbol{\nabla}\left(\frac{1}{2}\boldsymbol{v}_1^{\delta 0} - \mathrm{i}\boldsymbol{V}_1^0\right) - \mathrm{i}\boldsymbol{V}_1^{0*}\cdot\boldsymbol{\nabla}\boldsymbol{v}_1^{\text{d}} \tag{2.24b}$$

$$+ \left[\frac{2 - \mathrm{i}}{2}\boldsymbol{\nabla}\cdot\boldsymbol{v}_1^{\delta 0*} + \mathrm{i}\left(\boldsymbol{\nabla}\cdot\boldsymbol{V}_1^{0*} - \partial_\perp v_{1Z}^{\text{d}*}\right)\right]\boldsymbol{v}_1^{\delta 0}\right\},$$

$$v_{Z,\text{slip}}^{\text{ac}} = \frac{\delta}{2\omega}\text{Re}\left\{-k_0^2(1 - \mathrm{i})\boldsymbol{v}_1^{\delta 0}\cdot\boldsymbol{v}_1^{\text{d}0*} + \boldsymbol{\nabla}_\parallel\cdot\left[\boldsymbol{\nabla}\cdot\left\{-\frac{5}{4}\boldsymbol{v}_1^{\delta 0}\boldsymbol{v}_1^{\delta 0*}\right.\right.\right. \tag{2.24c}$$

$$+ \frac{1 + \mathrm{i}}{2}\left(\boldsymbol{V}_1^0\boldsymbol{v}_1^{\delta 0*} + \boldsymbol{v}_1^{\delta 0*}\boldsymbol{V}_1^0\right)\right\} + \left(\frac{1}{2\delta}v_{1Z}^{\delta 0*} + \frac{\mathrm{i}}{\delta}V_{1Z}^{0*} - (1 - \mathrm{i})\partial_\perp v_{1Z}^{d*}\right)\boldsymbol{v}_1^{\delta 0}$$

$$\left.\left.- \frac{\mathrm{i}}{\delta}v_{1Z}^{\delta 0*}\boldsymbol{V}_1^0\right]_\parallel\right\} + \frac{1}{2\omega}\text{Re}\left\{\mathrm{i}\boldsymbol{V}_1^{0*}\cdot\boldsymbol{\nabla}(\boldsymbol{v}_1^{\text{d}} + \boldsymbol{v}_1^{\delta 0}) - \frac{1 + \mathrm{i}}{\delta}V_{1Z}^{0*}\boldsymbol{v}_1^{\delta 0}\right\}_Z.$$

The long expression for the perpendicular component contains corrections of order $k_0\delta$ that are normally thought to be small enough to discard ($k_0\delta \sim 0.3\%$). However, for the acoustics simulations shown in this thesis, it turns out that the error in the bulk of the fluid caused by dropping these terms is significantly larger than $k_0\delta$. The reason for this is unknown.

2.3 Electroosmosis

2.3.1 Ionic currents

Electroosmosis is the motion of fluids relative to charged surfaces. The electric surface potential is generated by either surface charges due to chemical surface reactions or by external electrodes. An electric charge density is induced by separation of positive and negative ions dissolved in the fluid, when ions of opposite charge to the surface potential are attracted to screen away the incoming potential, while ions of similar charge are pushed away. The motion is induced by externally applied potentials that act on the charge density ρ_{el} accumulating near the charged surfaces, which generates a body force like the one included in Eq. (2.2a). The electric body force is simply expressed as

$$\boldsymbol{f}_{\text{b}} = \rho_{\text{el}}\boldsymbol{E}, \tag{2.25}$$

with $\boldsymbol{E}$ being the electric field.

The concentrations of ion species α will be denoted $c_\alpha(\boldsymbol{r}, t)$. Changes in ionic concentrations happen due to a combination of convection, diffusion, and electric current. Again, this can be formulated as a conservation law, resulting in the Nernst–Planck equation

$$\partial_t c_\alpha = -\boldsymbol{\nabla} \cdot \boldsymbol{J}_\alpha, \tag{2.26a}$$

$$\boldsymbol{J}_\alpha = c_\alpha \boldsymbol{v} - D_\alpha \boldsymbol{\nabla} c_\alpha - \mu_\alpha c_\alpha \boldsymbol{\nabla}\phi. \tag{2.26b}$$

Here, we have defined the ion mobility μ_α and the diffusion constant D_α for the ionic species α. We adopt a quasi-electrostatic description, where the charge movement is assumed to be slow enough that magnetic fields are negligible. The electric field can then be written as a gradient field

$$\boldsymbol{E} = -\boldsymbol{\nabla}\phi, \tag{2.27}$$

where ϕ is the electric potential. The governing equation for the electric field is Gauss's law, where we will only consider linearly polarisable and isotropic medias

$$\boldsymbol{\nabla} \cdot \boldsymbol{D} = \boldsymbol{\nabla} \cdot (\epsilon \boldsymbol{E}) = \rho_{\text{el}}. \tag{2.28}$$

Furthermore, we consider a constant electric permittivity ϵ, leading to the Poisson equation

$$\nabla^2 \phi = -\frac{1}{\epsilon}\rho_{\text{el}}. \tag{2.29}$$

Z_α will denote the valences of the species, and the electric charge density can be expressed as

$$\rho_{\text{el}}(\boldsymbol{r}, t) = e \sum_\alpha Z_\alpha c_\alpha(\boldsymbol{r}, t). \tag{2.30}$$

To simplify analysis, we consider the situation where only a single positive ion species denoted with a $+$ and a single negative ion species denoted with $-$ are present. Furthermore, their valences are assumed to follow $Z_+ = -Z_- = Z$, such that

$$\rho_{\text{el}} = Ze(c_+ - c_-).\tag{2.31}$$

2.3.2   The Debye layer

The accumulation of charge in an electrolyte near a charged wall is known as the Debye layer. Using a standard Cartesian (x, y, z) coordinate system, we consider a wall parallel to the xy-plane at $z = 0$ with a constant surface potential ζ. Over the wall, a solution of ions with a bulk concentration of c_0 is present, and we have the following boundary conditions at equilibrium

$$c_\pm(z = \infty) = c_0, \qquad \phi(z = \infty) = 0, \qquad \phi(z = 0) = \zeta.\tag{2.32}$$

We consider an equilibrium solution with no fluid flow or electric current, such that Eq. (2.26b) yields

$$\boldsymbol{J}_\pm = -D_\pm \boldsymbol{\nabla} c_\pm - \mu_\pm c_\pm \boldsymbol{\nabla} \phi = \boldsymbol{0},\tag{2.33}$$

or

$$c_\pm = c_0 \exp\left(-\frac{\mu_\pm}{D_\pm}\phi\right).\tag{2.34}$$

It is often used that

$$\mu_\pm = \pm\frac{ZeD_\pm}{k_{\text{B}}T},\tag{2.35}$$

where k_{B} is the Boltzmann constant and T is the temperature. Inserting these in Eq. (2.31), the electric charge density becomes

$$\rho_{\text{el}} = -2Zec_0 \sinh\left(\frac{Ze}{k_{\text{B}}T}\phi\right),\tag{2.36}$$

and the equation governing the equilibrium potential reads

$$\nabla^2\phi = \frac{2Zec_0}{\epsilon} \sinh\left(\frac{Ze}{k_{\text{B}}T}\phi\right).\tag{2.37}$$

For the one-dimensional case, this can be solved by the Gouy-Chapman solution

$$\phi(z) = \frac{4k_{\text{B}}T}{Ze}\operatorname{arctanh}\left[\tanh\left(\frac{Ze\zeta}{4k_{\text{B}}T}\right)\exp\left(-\frac{z}{\lambda_{\text{D}}}\right)\right],\tag{2.38}$$

where we have defined the Debye length

$$\lambda_{\text{D}} = \sqrt{\frac{\epsilon k_{\text{B}}T}{2(Ze)^2c_0}}.\tag{2.39}$$

For typical bulk concentrations of $c_0 = 1\,\text{mM}$ in water at $25°\text{C}$, the Debye length for monovalent ions is $\lambda_\text{D} = 9.7\,\text{nm}$. For sufficiently small surface potentials, where the electric energy is much lower than the thermal energy,

$$Ze\zeta \ll k_\text{B}T, \tag{2.40}$$

one can Taylor expand the right-hand side of Eq. (2.37) such that

$$\nabla^2\phi = \frac{1}{\lambda_\text{D}^2}\phi. \tag{2.41}$$

This is known as the Debye-Hückel approximation.

2.3.3 DC electroosmotic slip velocity

It is assumed that an external DC potential ϕ_ext is applied to the fluid chamber with an ionic solution, and charged walls. The external potential is designed such that it creates a constant electric field $\boldsymbol{E}_\text{ext}$ within the fluid. We expand our fields in equilibrium- and externally induced fields

$$p = p_\text{eq} + p_\text{ext}, \tag{2.42a}$$

$$c_\pm = c_{\pm,\text{eq}} + c_{\pm,\text{ext}}, \tag{2.42b}$$

$$\phi = \phi_\text{eq} + \phi_\text{ext}, \tag{2.42c}$$

$$\boldsymbol{v} = \boldsymbol{v}_\text{eq} + \boldsymbol{v}_\text{ext}. \tag{2.42d}$$

Here, we note that there is no flow in the equilibrium situation, such that $\boldsymbol{v} = \boldsymbol{v}_\text{ext}$. Typically, the externally applied electric fields in electroosmotic experiments are much smaller than the electric fields associated with the thin equilibrium Debye layers. Because of this, we will assume that the externally applied DC field does not influence the equilibrium configuration the ions particularly much, so that

$$\rho_\text{el} \approx \rho_\text{el,eq}, \tag{2.43}$$

where $\rho_\text{el,eq}$ is calculated from Eq. (2.36), and ϕ_eq is found from Eq. (2.37).

The flow under consideration is assumed to be in steady state, and we consider flow-velocities much lower than the speed of sound in the fluid, so the fluid can be considered incompressible. With this, the continuum and Navier–Stokes equations read

$$0 = \boldsymbol{\nabla}\cdot\boldsymbol{v}_\text{ext}, \tag{2.44a}$$

$$\rho(\boldsymbol{v}_\text{ext}\cdot\boldsymbol{\nabla})\boldsymbol{v}_\text{ext} = -\boldsymbol{\nabla}(p_\text{eq}+p_\text{ext}) + \eta\nabla^2\boldsymbol{v}_\text{ext} - \rho_\text{el,eq}\boldsymbol{\nabla}(\phi_\text{eq}+\phi_\text{ext}). \tag{2.44b}$$

The term $\rho_\text{el,eq}\boldsymbol{\nabla}\phi_\text{eq}$ is balanced by the equilibrium pressure gradient $\boldsymbol{\nabla}p_\text{eq}$. Further, we only consider velocities of up to approximately $100\,\text{µm}/s$. In the bulk of the fluid, changes happen on the length scale of approximately $d \approx 100\,\text{µm}$ such that $\nabla \sim d^{-1} \sim 10^4\,\text{m}^{-1}$. With this, the viscous term $\eta\nabla^2\boldsymbol{v}_\text{ext}$ is approximately two orders of magnitude larger than the non-linear term on the left-hand side. Near the wall of the fluid chamber, the viscous

term is even more dominant, and the non-linear term is dropped. Lastly, we drop the
ext subscript from the velocity and pressure fields, and the governing equations for the
electroosmotic flow read

$$0 = \boldsymbol{\nabla} \cdot \boldsymbol{v}, \tag{2.45a}$$

$$\boldsymbol{0} = -\boldsymbol{\nabla}p + \eta\nabla^2\boldsymbol{v} - \rho_{\text{el,eq}}\boldsymbol{\nabla}\phi_{\text{ext}}. \tag{2.45b}$$

The electric body force is only present in the thin Debye layer near the charged walls,
and it is customary to divide the problem into the length scale of the Debye layer and the
length scale of the bulk fluid. In the thin boundary layer, where the electric body force
is induced, viscous effects dominate over the pressure. Thus, we write the Navier–Stokes
equation in the Debye layer as

$$\boldsymbol{0} = \eta\nabla^2\boldsymbol{v} + \rho_{\text{el,eq}}\boldsymbol{E}_{\text{ext}} = \nabla^2(\eta\boldsymbol{v} - \epsilon\phi_{\text{eq}}\boldsymbol{E}_{\text{ext}}). \tag{2.46}$$

Directing the y-axis along the parallel component of the fluid flow with respect to the wall
with the Debye layer extending along the z direction, the incompressible condition yields
$\partial_y v_y + \partial_z v_z = 0$. Here, $\partial_y \sim d^{-1}$ and $\partial_z \sim \lambda_{\text{D}}^{-1}$, where d is the lowest length scale of
variation along the boundary. This means that

$$v_y \sim \frac{d}{\lambda_{\text{D}}}v_z \gg v_z, \tag{2.47}$$

as d is assumed to be much larger than the Debye layer thickness of approximately $10\,\text{nm}$.
One can then assume the velocity to be exclusively parallel to the boundary within the
Debye layer. Denoting $\phi_{\text{eq}}(\boldsymbol{s}_0) = \zeta$, and imposing the no-slip boundary condition, we find
the flow in the thin boundary layer to follow

$$\boldsymbol{v} = -\left(1 - \frac{\phi_{\text{eq}}}{\zeta}\right)\frac{\epsilon\zeta}{\eta}\boldsymbol{E}_{\text{ext}\|} = \left(1 - \frac{\phi_{\text{eq}}}{\zeta}\right)\boldsymbol{v}_{\text{slip}}^{\text{EO}}, \qquad \text{where} \quad \boldsymbol{v}_{\text{slip}}^{\text{EO}} = -\frac{\epsilon\zeta}{\eta}\boldsymbol{E}_{\text{ext}\|}. \tag{2.48}$$

This is exact in the case of a truly constant zeta potential and a constant parallel electric
field along an infinite translational invariant boundary. The solution is a good approx-
imation as long the surface potential $\zeta = \zeta(\boldsymbol{s}_0)$ varies over a length scale $d \gg \lambda_{\text{D}}$. In
this case $\nabla^2\phi_{\text{eq}} \approx \partial_\perp^2\phi_{\text{eq}}$, such that the equilibrium potential is well approximated by the
one-dimensional solution in Eq. (2.38) with a slowly varying ζ inserted. A standard Stokes
flow is present in the bulk of the fluid, where the electric body force has vanished. On the
length scale of the bulk, the equilibrium potential for practical purposes vanishes on the
wall of the fluid container. This means that from the perspective of the bulk fluid, the
velocity essentially goes to $\boldsymbol{v}_{\text{slip}}^{\text{EO}}$ at the wall. In the bulk of the fluid, the flow problem can
thus be solved as a Stokes flow with a slip velocity analogue to the acoustic streaming

$$0 = \boldsymbol{\nabla} \cdot \boldsymbol{v}, \tag{2.49a}$$

$$\boldsymbol{0} = -\boldsymbol{\nabla}p + \eta\nabla^2\boldsymbol{v}, \tag{2.49b}$$

$$\boldsymbol{v}(\boldsymbol{s}_0) = \boldsymbol{v}_{\text{slip}}^{\text{EO}}. \tag{2.49c}$$

3 | Numerical simulations

The mathematical models of acoustofluidic systems combined with electroosmotic effects include complicated systems of coupled equations. For many studies, we will therefore turn to numerical simulations. All simulations are carried out in COMSOL Multiphysics 5.4 [17], which is a commercial finite element software.

3.1 The finite element method

The equations used to describe physical fields in this thesis can all be written on the form of a conservation law

$$\boldsymbol{\nabla} \cdot \boldsymbol{J}[u(\boldsymbol{r}, t)] - F[\boldsymbol{r}, t] = 0. \tag{3.1}$$

Here, $\boldsymbol{J}$ is a generalised flux that is some functional of the physical field $u(\boldsymbol{r}, t)$. F is a generalised force that can generally also depend on $u(\boldsymbol{r}, t)$. This form of the equation is known as the *strong form*. The finite element method approximates the solution to this equation numerically. The spatial domain, in which we are trying to find the solution, is divided into a grid of N points. The points are combined with straight lines without overlapping, and the elements outlined by the lines are called mesh elements. The mesh elements that share the common vertex in the n'th point of the grid $\boldsymbol{r}_n$ form a mesh-cell. For each point $\boldsymbol{r}_n$, a test function $\hat{u}_n$ is formed. This is illustrated in figure 3.1. The test functions are piecewise polynomials of order p that are bounded on the mesh cells, and they are normalised such that $\hat{u}_n(\boldsymbol{r}_n, t) = 1$. These test functions are then used as basis
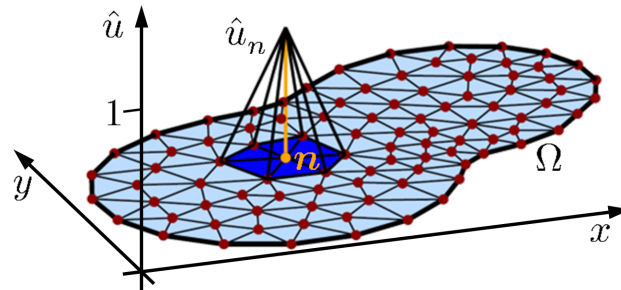

Figure 3.1: Typical finite element mesh for a 2D geometry. The test function $\hat{u}_n$ is defined on the mesh cell, which is shaded dark blue. Adopted from [18].

functions for our physical field

$$u(\boldsymbol{r}, t) = \sum_{n=1}^{N} C_n^{(u)} \hat{u}_n(\boldsymbol{r}, t), \tag{3.2}$$

where $C_n^{(u)}$ are constants. With this approximation, Eq. (3.1) may not be perfectly fulfilled, leading to a defect $d(\boldsymbol{r}, t)$ on the right-hand side

$$\boldsymbol{\nabla} \cdot \boldsymbol{J}[u(\boldsymbol{r}, t)] - F[\boldsymbol{r}, t] = d(\boldsymbol{r}, t). \tag{3.3}$$

The defect is minimised by insisting that the projection of all the basis functions on the defect $\int_{\Omega} \hat{u}_m d \, \mathrm{d}\boldsymbol{r}$ should vanish. This leads to the condition

$$\int_{\Omega} \hat{u}_m(\boldsymbol{r}, t)[\boldsymbol{\nabla} \cdot \boldsymbol{J}[u(\boldsymbol{r}, t)] - F(\boldsymbol{r}, t)] \, \mathrm{d}\boldsymbol{r} = 0. \tag{3.4}$$

This is known as the *weak form* of the equation. For linear operators $\boldsymbol{J}$, this can be formulated as

$$\sum_{n=1}^{N} C_n^{(u)} \int_{\Omega} \hat{u}_m(\boldsymbol{r}, t)(\boldsymbol{\nabla} \cdot \boldsymbol{J}[\hat{u}_n(\boldsymbol{r}, t)]) \, \mathrm{d}\boldsymbol{r} = \int_{\Omega} \hat{u}_m F(\boldsymbol{r}, t) \, \mathrm{d}\boldsymbol{r}. \tag{3.5}$$

This is on the form of a matrix equation, and by defining the components

$$(\boldsymbol{C})_n = C_n^{(u)}, \tag{3.6a}$$

$$(\boldsymbol{K})_{mn} = \int_{\Omega} \hat{u}_m(\boldsymbol{r}, t)\big(\boldsymbol{\nabla} \cdot \boldsymbol{J}[\hat{u}_n(\boldsymbol{r}, t)]\big) \, \mathrm{d}\boldsymbol{r}, \tag{3.6b}$$

$$(\boldsymbol{F})_m = \int_{\Omega} \hat{u}_m(\boldsymbol{r}, t) F(\boldsymbol{r}, t) \, \mathrm{d}\boldsymbol{r}, \tag{3.6c}$$

the problem is restated as

$$\boldsymbol{K}\boldsymbol{C} = \boldsymbol{F}, \tag{3.7}$$

where the coefficients $C_n^{(u)}$ are found through matrix inversion of $\boldsymbol{K}$. Using the product rule and Gauss's theorem, the weak form equation can be written as

$$\oint_{\partial\Omega} [\hat{u}_m \hat{\boldsymbol{n}} \cdot \boldsymbol{J}] \, \mathrm{d}A + \int_{\Omega} [(-\boldsymbol{\nabla}\hat{u}_m) \cdot \boldsymbol{J} - \hat{u}_m F] \, \mathrm{d}\boldsymbol{r} = 0. \tag{3.8}$$

With this, Neumann boundary conditions can be implemented as $\hat{\boldsymbol{n}} \cdot \boldsymbol{J} = N(\boldsymbol{r}, t)$. Other boundary conditions such as Dirichlet can also be implemented through Lagrange multipliers.

Table 3.1: Parameters used for the basic acoustics simulations [21].

ρ_0	$997\,\mathrm{kg/m^3}$	c_{fl}	$1496.7\,\mathrm{m/s}$
η	$0.890\,\mathrm{mPa\,s}$	β	3.1256
κ_{s}	$447.7\,\mathrm{TPa^{-1}}$	f	$1.993\,\mathrm{MHz}$

3.2 Basic setup

To heavily reduce computational footprints, we will only simulate two-dimensional geometries. The geometries will be models of fluid channel cross sections like the one shown figure 1.1, sometimes including surrounding solids. The essential assumptions are that the channels are very elongated and that no significant change in the physical fields happen along them. Basic flow calculations are shown in the proceedings, and demonstrations of the effective boundary conditions are included. Throughout the thesis, a right-handed Cartesian (y, z) coordinate system is used. Further, a local right-handed Cartesian (Y, Z) coordinate system is used at the boundaries of the fluid channels. Since we are in 2D, only a single parallel unit vector and a perpendicular unit vector pointing into the fluid are needed. These are denoted by $\hat{\boldsymbol{e}}_\parallel$ and $\hat{\boldsymbol{e}}_\perp$, respectively. These coordinate systems are illustrated in figure 3.2.

The computational strategy is to initially calculate the first-order acoustic fields for the acoustics simulations and the equilibrium potential for electroosmotic simulations. In a second step, the streaming is calculated based on the fields found in the initial calculation.

3.2.1 Acoustics simulations

The basis for the initial simulations of this thesis will be a fluid cross section similar to one which has previously been extensively studied by Muller and Bruus [19][20][21][22]. It is a simple rectangular channel of dimensions $H_{\mathrm{ch}} \times W_{\mathrm{ch}} = 160\,\mu\mathrm{m} \times 375\,\mu\mathrm{m}$. For all simulations in this thesis, the fluid channel is centered in $(y, z) = (0, 0)$. The simulated equations and geometry are illustrated in figure 3.2 (a), and the finite element meshes used for full and effective simulations are shown in 3.2 (b). The required mesh for the effective simulation is much coarser, because the thin boundary layer is taken into account analytically. The fluid in the chamber is simulated as water at 25°C, and the basic parameters used for acoustics simulations are given in table 3.1.

The acoustic actuation of the chamber is put in artificially in order to not simulate the solid mechanics of the surroundings. For water, the width of the given cross section can support standing half-waves for actuation frequencies close to $f = 2\,\mathrm{MHz}$. The actuation is put in as a resonant boundary condition on $\boldsymbol{s}_1$ and is adopted from an analytical example in [4]. The top and bottom boundaries are kept stationary, while the sides are actuated by

$$\boldsymbol{s}_1(y = \pm W_{\mathrm{ch}}/2, z) = d_0 \cos\left(\sqrt{-(1+\mathrm{i})\frac{\delta}{H_{\mathrm{ch}}}}\, k_0 z\right), \qquad f = f_{\mathrm{res}} = \frac{c_0}{2W_{\mathrm{ch}}}\left(1 - \mathrm{i}\frac{1}{2}\Gamma_{\mathrm{bl}}\right).$$

(3.9)

The results of this typical acoustics simulation are also shown in figure 3.2. The figure
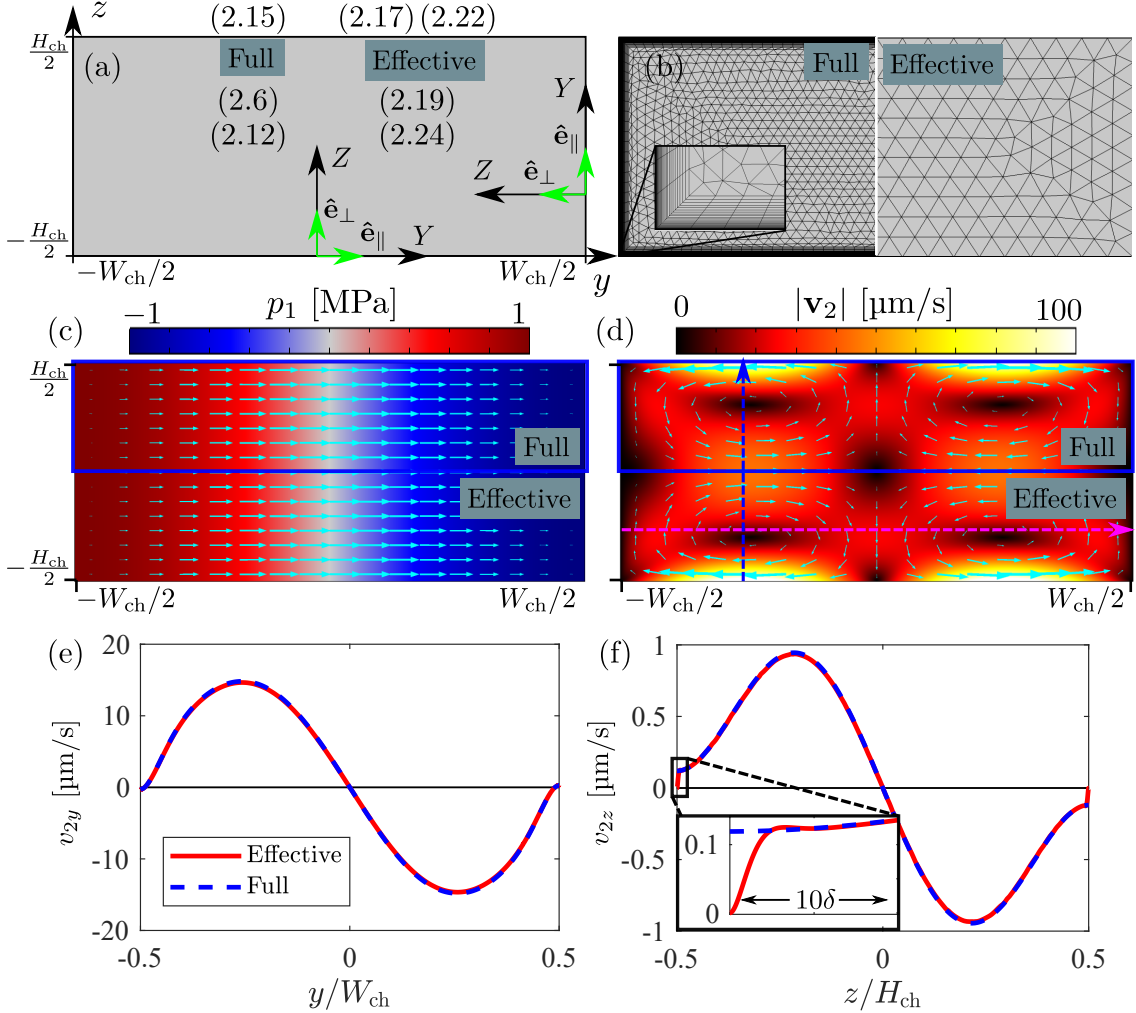
Figure 3.2: Standard solution of a closed cavity acoustic half-wave resonance with second-order streaming. (a) cross section of the fluid channel of dimensions $H_{ch} \times W_{ch}$. Equations implemented in the bulk are written inside the geometry, while boundary conditions are written outside. The local coordinate system used at the fluid boundary in the thesis is illustrated at two of the boundaries. (b) finite element meshes for full and effective theory calculations. (c) field plots of the acoustic pressure p_1. The cyan coloured arrows on top of the pressure field illustrate $\boldsymbol{v}_1$. (d) $\boldsymbol{v}_2$ field plots. Cyan coloured arrows are of $\boldsymbol{v}_2$. (e) v_{2y} calculation from the effective and the full theory along the magenta dashed arrow shown in (d). (f) v_{2z} shown along the blue dashed arrow. A zoom-in close to the boundary illustrates the rapid growth of the velocity field near a boundary in the full theory.
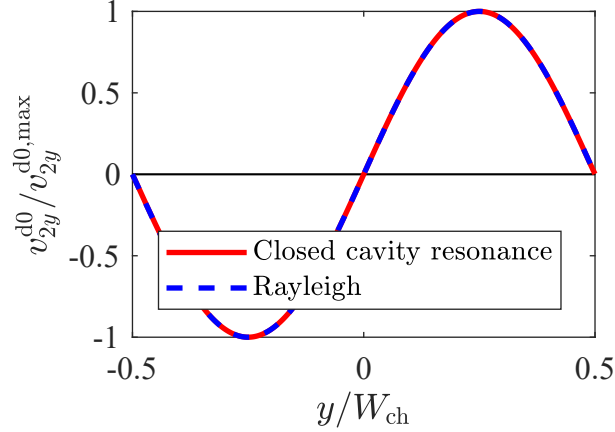
Figure 3.3: Closed cavity slip velocity compared to the Rayleigh slip velocity. The closed cavity slip velocity is remarkably similar to the one found for an infinite half-plane, even for a single half-wave resonance.

illustrates the full simulation alongside a simulation with the effective boundary conditions described in Eq. (2.19) and Eq. (2.24). A zoom-in on the boundary layer illustrates the difference in boundary conditions for the full and effective theory. A very rapid growth in the amplitude of the acoustic streaming is seen at the boundary of the chamber for the full simulation to satisfy the no-slip boundary condition. The effective theory takes this growth into account analytically and assumes it to happen immediately on the boundary. This thin layer with an abrupt change in the physical fields is present to both first- and second order. Due to the vast difference in required mesh elements, numerical calculations with the effective theory are significantly faster than the full theory. In 2D, a typical simulation like the one shown in figure 3.2 takes of the order of 5 s with the effective theory and 30 s with the full theory. The effective theory has even allowed us to do full system 3D models of acoustofluidic systems [23]. The fit between the full and the effective theory is very precise, and the effective theory is used in all remaining simulations including acoustics, unless we want to explicitly illustrate the boundary layer streaming.

The acoustic streaming associated with this standard half-wave mode is driven by a conveyor-belt effect on the top and bottom boundaries, which turns out to be similar to one found in a classical calculation by Lord Rayleigh [24]. He considered a timely and spatially harmonic standing pressure wave above an infinite half-plane. Assuming the spatial period $2\pi/k_0$ to be much longer than the viscous boundary layer thickness, terms to lowest order in $k_0\delta$ are calculated. If the half-plane boundary is situated in $z = 0$, the flow problem for $z > 0$ is defined by

$$p_1(y,z) = \mathrm{i}\rho_0 c_{\mathrm{fl}} u_0 \sin(k_0 y), \qquad \boldsymbol{s}_1(y, z = 0) = \mathbf{0}, \qquad (3.10)$$

where u_0 is the amplitude of the spatially and timely harmonic first-order velocity field. By splitting the equations for the first- and second-order fields into different length scales (boundary layer and bulk fluid), one can find a slip velocity parallel to the boundary given

by

$$\boldsymbol{v}_2^{\mathrm{d}}(y, z = 0) = \boldsymbol{v}_{2,\mathrm{slip}}^{\mathrm{Rayleigh}} \equiv \frac{3}{8}\frac{u_0^2}{c_{\mathrm{fl}}}\sin(2k_0 y)\hat{\boldsymbol{e}}_y. \tag{3.11}$$

The normalised $v_{2y}^{\mathrm{d}}(\boldsymbol{s}_0)$ at the bottom boundary of the chamber from the standard acoustics simulation is shown alongside the Rayleigh slip velocity at $k_0 = \pi/W_{\mathrm{ch}}$ in figure 3.3. We see that the parallel component of the closed cavity slip velocity follows the same form as the Rayleigh solution. The slip velocity on the sides of the chamber and the perpendicular component on the top and bottom boundaries are all around two orders of magnitudes lower than $v_{2y}^{\mathrm{d}}(\boldsymbol{s}_0)$ from the top and bottom boundaries.

3.2.2 Electroosmotic simulations

We now turn to the electroosmotic flow. To illustrate the validity of the boundary condition shown in Eq. (2.48), a simple simulation is set up with the electroosmotic slip velocity and electric body force, respectively. The geometry is identical to the previous simulation illustrated in figure 3.2. The boundary conditions on the potential are set to

$$\phi_{\mathrm{eq}}(y, z = -H_{\mathrm{ch}}/2) = V_0 \exp\left[-\left(\frac{4y}{W_{\mathrm{ch}}}\right)^2\right], \tag{3.12a}$$

$$\phi_{\mathrm{eq}}(y, z = H_{\mathrm{ch}}/2) = \phi_{\mathrm{eq}}(y = \pm W_{\mathrm{ch}}/2, z) = 0, \tag{3.12b}$$

where $V_0 = 1$ mV. The no-slip boundary condition is implemented on all boundaries except for the one at $z = -H_{\mathrm{ch}}/2$ for the slip-velocity simulation, where Eq. (2.48) is implemented. A constant external electric field is applied as

$$\boldsymbol{E}_{\mathrm{ext}} = -\frac{E_0}{\sqrt{2}}(\hat{\boldsymbol{e}}_y + \hat{\boldsymbol{e}}_z), \tag{3.13}$$

where $E_0 = (1\,\mathrm{V}/W_{\mathrm{ch}})$. The positive ion is modelled as Na^+, and the negative ion is Cl^-. Again, a temperature of 25°C is assumed. Whenever a fluid is modelled, the fluid is taken to be water, and its electric permittivity is denoted ϵ_{f}. When the surrounding solid is simulated, its electric properties are taken to be those of pyrex glass, and the permittivity is denoted ϵ_{s}. Parameters used for the steady electroosmotic simulations are given in table 3.2, and the results of the simulations are illustrated in figure 3.4. For the electroosmotic simulations, equally course meshing can be used in the bulk of the fluid for the full and the effective theory, while the solutions with the electric body force need a thin boundary layer mesh at the surrounding solid walls.

Table 3.2: Parameters used for the basic electroosmotic simulations [16].

D_+	$1.33 \times 10^{-9}\,\mathrm{m}^2/\mathrm{s}$	c_0	$1\,\mathrm{mM}$
D_-	$2.03 \times 10^{-9}\,\mathrm{m}^2\mathrm{s}$	λ_{D}	$9.71\,\mathrm{nm}$
μ_+	$5.19 \times 10^{-8}\,\mathrm{m}^2/(\mathrm{V} \times \mathrm{s})$	ϵ_{f}	$80\epsilon_0$
μ_-	$-7.91 \times 10^{-8}\,\mathrm{m}^2/(\mathrm{V} \times \mathrm{s})$	ϵ_{s}	$4.6\epsilon_0$[25]
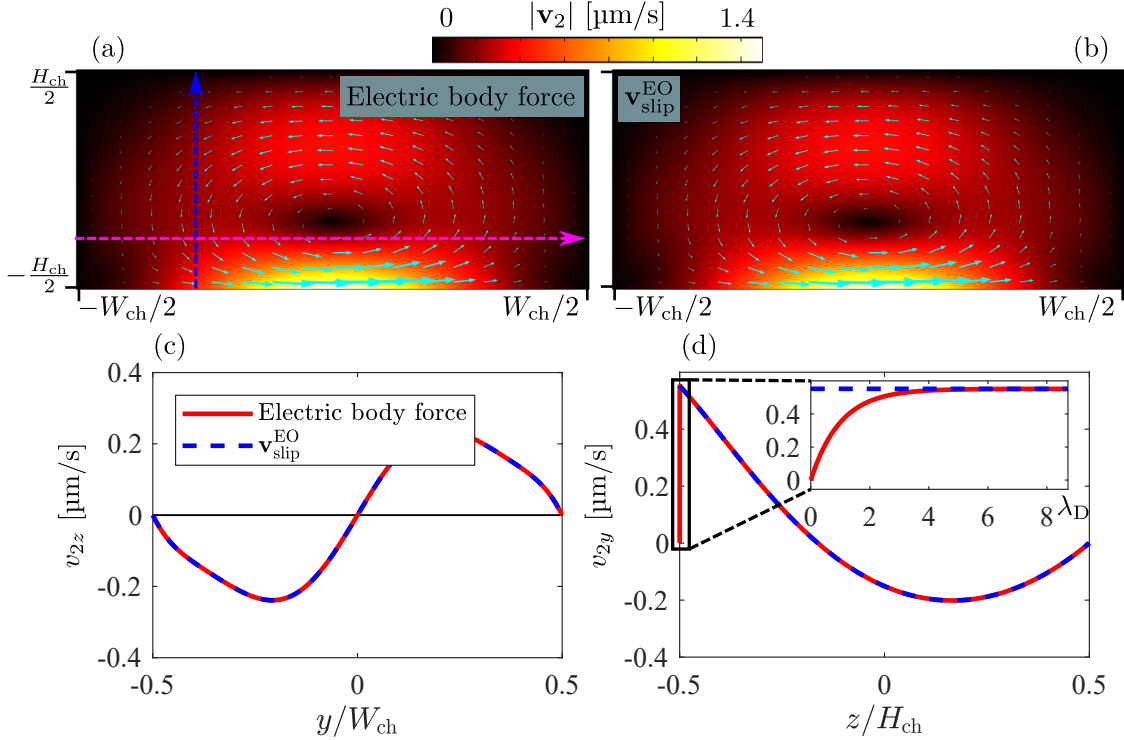
Figure 3.4: Electroosmotic flow solution with comparison between slip velocity and electric body force implementation. (a) Field plot of the steady velocity field $\boldsymbol{v}_2$ calculated with the electric body force. (b) Calculation with the electroosmotic slip velocity. (c) Plot of the vertical streaming component along the magenta dashed arrow for the two implementations. (d) The horizontal streaming components shown along the blue dashed arrow. A zoom-in on the boundary displays the rapid growth in the velocity for the full theory with the electric body force confined to the thin Debye layer.

For the electric field with equally large components parallel and perpendicular to the boundary, the parallel component still dominates completely, and the two solutions are almost identical. The electroosmotic slip velocity will be used in the proceeding work.

3.3 Convergence tests

The simulations need to include enough mesh elements to properly resolve the details of the physical fields. To ensure that a stable solution has been reached, one should perform some sort of convergence test. Since increasing mesh sizes increase computational footprint, it is desirable to look for a compromise between mesh size and precision. We define a relative convergence parameter by

$$C(u) = \sqrt{\frac{\int_{\Omega} |u - u_{\text{ref}}|^2 \, \mathrm{d}\boldsymbol{r}}{\int_{\Omega} |u_{\text{ref}}|^2 \, \mathrm{d}\boldsymbol{r}}}. \tag{3.14}$$

Here, u refers to a given solution for the given field, whereas u_{ref} is a reference solution for comparison. The reference solution is ideally an exact solution that one can use to test their simulation. For cases where no analytical solutions can be found, one can instead use the best possible solution your computer can give. The relative convergence parameters should converge continuously towards the reference solution with increasing numbers of mesh elements. We are looking for exponential convergences, and in this thesis a relative convergence within 1% is aimed for.

Whenever we simulate new set of equations, a convergence test is ran to explore the required mesh size. Typically, a characteristic length scale of the system under consideration is used to scale the size of mesh elements e.g. an acoustic wavelength or the boundary layer thicknesses. If this characteristic length scale is changed in a future simulation, the mesh can be refined correspondingly. Furthermore, all new simulations are checked qualitatively, to see whether or not anomalies such as discontinuous derivatives in the fields, which could be caused by numerical errors, are present in the physical fields. If the solutions contain these sorts of problems, the meshes can be locally refined.

A convergence test for the acoustics simulations is illustrated in figure 3.5. Here, the maximum mesh element size in the bulk of the fluid could have been scaled with respect to the acoustic wavelength. Instead, it was scaled as δ/N to check for reasonable agreement with previous work [19]. In any case, all simulations with acoustics will be of the half-wave mode shown above. For the full acoustics simulations, fourth-order polynomials are used to resolve $\boldsymbol{v}_1$ and $\boldsymbol{v}_2$, whereas third-order polynomials are used for the pressure fields p_1 and p_2. For the effective theory, third-order polynomials resolve the velocity fields, and second-order polynomials are used for the pressure fields. We notice how the second-order pressure field converges much slower than the remaining fields in the effective simulation. We will not worry too much about this, since we cannot use p_2 explicitly, and it more so serves as a Lagrange multiplier for the problem. To reach precision of approximately 1% for the remaining fields, $N = 0.05$ was chosen for the full theory and $N = 0.02$ was chosen for the effective simulations. The boundary layer for the full theory was resolved with 15 boundary layers in the convergence test with the first layer of thickness $\delta/5$ and a scaling factor per layer of 1.1. For full simulations shown in the thesis (acoustics as well as electroosmotic), 25 boundary layers were implemented for safety, because tiny numerical defects were sometimes observed at the end of the boundary layers.
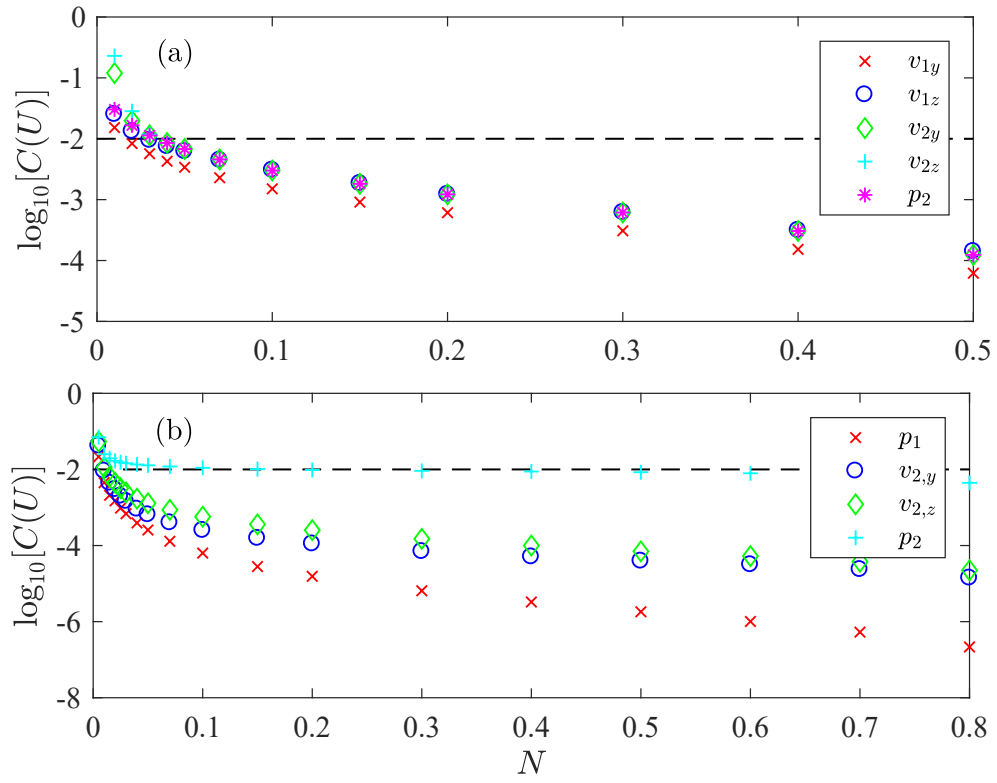
Figure 3.5: Convergence test for acoustics simulations. The relative convergence on logarithmic scale is shown for both the effective fields (b) and the fully simulated fields (a).

4 | Combined acoustics and DC electroosmosis

We have seen that both acoustic streaming and DC electroosmosis can be described as linear Stokes flows with slip velocities. Since the governing equations are linear in the velocity vectors, the two theories seem to trivially combine to a single Stokes flow with two separate slip velocities. This will hold true as long as first-order acoustic effects are uncoupled from the ionic motion. Due to the tiny diameters of ions, viscous drag forces will vastly dominate their motion compared to the acoustic radiation force. One concern would be whether or not ions would start moving out of phase with the oscillating fluid, which could disturb the equilibrium configuration of the ions at the wall or polarise the bulk. Assuming that only viscous drag is important, Newton's second law for a dissolved ion with velocity $\boldsymbol{u}$ relative to the fluid is given by

$$m_{\text{ion}}\partial_t\boldsymbol{u} = -6\pi\eta a\boldsymbol{u}, \tag{4.1}$$

where the ion is modelled as a perfect sphere of radius a. With an initial relative velocity $\boldsymbol{u}_0$, we find that

$$\boldsymbol{u} = \boldsymbol{u}_0\exp\left(-\frac{6\pi\eta a}{m_{\text{ion}}}t\right), \tag{4.2}$$

meaning that the ion comes to rest with respect to the fluid on a timescale of $\tau = \frac{m_{\text{ion}}}{6\pi\eta a}$. When ions are dissolved in water, they are typically surrounded closely by a layer of water molecules that are attracted to the ions due to their polarity. Thus, we will consider the weight and radius of a so-called hydrated ion [26]. To overestimate the typical timescale, we consider a fairly low hydrated ionic radius of $a = 0.2\,\text{nm}$, and a high hydration number of 10 water molecules. The typical timescale for a sodium ion coming to rest in water at room temperature would then be around

$$\tau = \frac{m_{\text{Na}^+} + 10\,m_{\text{H}_2\text{O}}}{6\pi\eta a} \approx 10^{-13}\,\text{s}. \tag{4.3}$$

For pressure waves of frequencies in the MHz regime, the ions will essentially appear to perfectly follow the fluid. Thus, the ions in the Debye layer should closely follow the motion of the fluid in the layer, which essentially just vibrates harmonically with the wall to fulfil the no-slip boundary condition. At the timescales of our interest, the behaviour of the ions at the fluid/solid boundary can be evaluated from the average position $\boldsymbol{s}_0$, and we expect

no coupling between the phenomena. The time-averaged fluid flows in the microfluidic systems under consideration will thus simply be described by Eq. (4.4a) and Eq. (4.4b) with an acoustic and an electroosmotic slip velocity. Since the flow is to second order, and since the gradient term in Eq. (4.4b) can be regarded as an effective pressure gradient, we write the governing flow equations as

$$0 = \boldsymbol{\nabla} \cdot \boldsymbol{v}_2, \tag{4.4a}$$

$$\boldsymbol{0} = -\boldsymbol{\nabla} p_2 + \eta \nabla^2 \boldsymbol{v}_2 + \frac{\Gamma_{\text{fl}} \omega}{c_0^2} \langle \boldsymbol{S}_{\text{ac}}^{\text{d}} \rangle, \tag{4.4b}$$

$$\boldsymbol{v}_2(\boldsymbol{s}_0) = \boldsymbol{v}_{\text{slip}}^{\text{ac}} + \boldsymbol{v}_{\text{slip}}^{\text{EO}}. \tag{4.4c}$$

4.1   Suppressing acoustic streaming

For single acoustic mode operation in fluid channels with elongated rectangular cross-sections, the acoustic body force $\boldsymbol{f}_{\text{ac}} = \Gamma_{\text{fl}} \omega \langle \boldsymbol{S}_{\text{ac}}^{\text{d}} \rangle / c_0^2$ will be vanishingly small. In this case, acoustic streaming is almost exclusively generated due to the relative motion between the fluid and surrounding solid [5]. The streaming in the bulk thus appears due to the slip velocity, and if we could control the electroosmotic slip velocity at will, it would become a mathematically trivial task to cancel acoustic streaming by setting $\boldsymbol{v}_{\text{slip}}^{\text{EO}} = -\boldsymbol{v}_{\text{slip}}^{\text{ac}}$. The electroosmotic slip velocity is only suited for counteracting the parallel component of the acoustic slip velocity. Luckily, this is usually the dominant one for resonance modes in microchannels. As illustrated previously, the typical acoustic slip velocity will resemble that of the classical Rayleigh streaming calculation even for a half-wave mode in the cross section of our model system. This means that the leading source of acoustic streaming is the parallel slip velocity on the top and bottom boundaries of the chamber. In the following simulations, we assume that a constant external electric field has been applied horizontally across the cross-section of our standard fluid channel

$$\boldsymbol{E}_{\text{ext}} = E \hat{\boldsymbol{e}}_y. \tag{4.5}$$

Thus, we should be able to suppress the majority of the streaming by applying

$$\zeta(y, z = \pm H_{\text{ch}}/2) = A \frac{\eta}{\epsilon_{\text{f}} E} \left| \boldsymbol{v}_{\text{slip}}^{\text{Rayleigh}} \right|, \tag{4.6}$$

where A is a dimensionless parameter varied to minimise the streaming. A parametric sweep is set up, where the average value of the steady velocity amplitude in the chamber $|\boldsymbol{v}_2|_{\text{avg}}$ is calculated for each value of A. The resulting curve is shown alongside field plots from the solution with the lowest average streaming amplitude in figure 4.1. It is illustrated how the perpendicular component of $\boldsymbol{v}_2$ at the wall (the perpendicular slip velocity) is unchanged for changing values of A. This will always leave a bit of streaming in the chamber, albeit the streaming can be greatly reduced. The lowest average streaming at $A = 0.972$ has an amplitude of $0.7\,\mu\text{m/s}$ (for the effective theory). Compared to the standard simulation of $A = 0$, where we find an average streaming of $28.5\,\mu\text{m/s}$, the streaming is reduced by more than an order of magnitude.
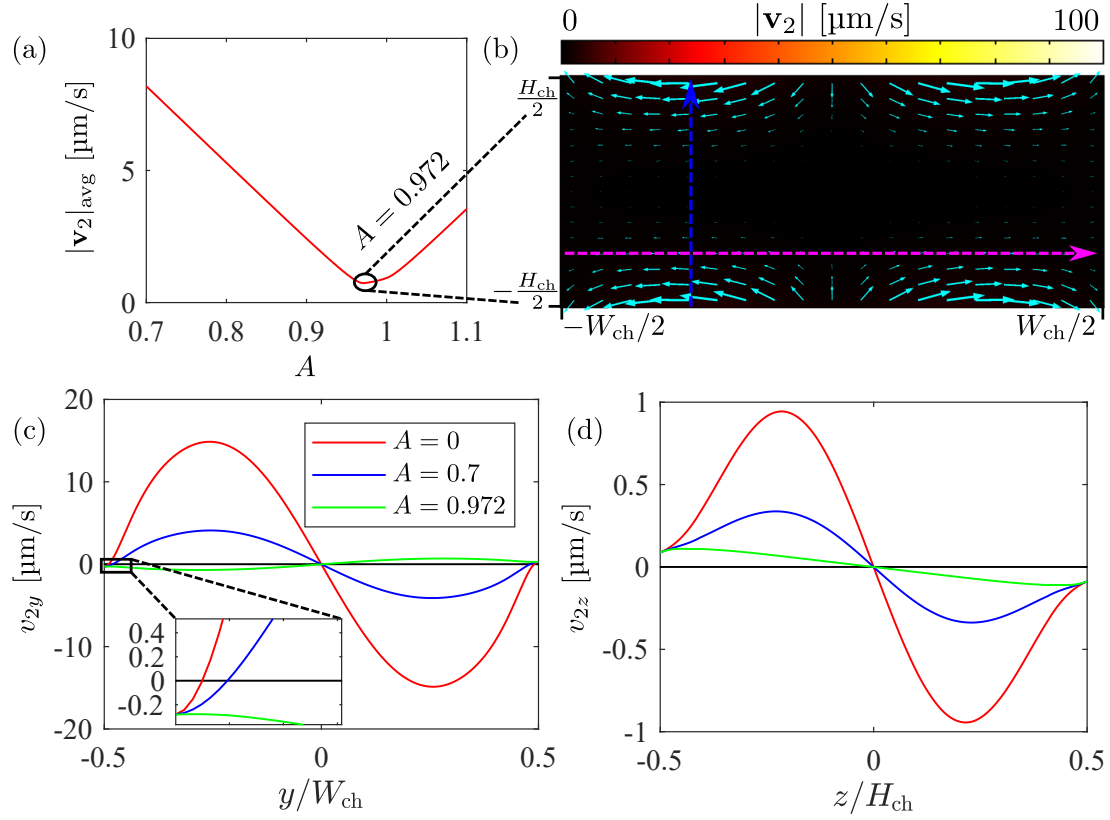
Figure 4.1: Acoustic streaming stop with idealised electroosmotic counter flow rolls. (a) average streaming amplitude $|\boldsymbol{v}_2|_{\text{avg}}$ plotted against A from Eq. (4.6). (b) field plot of the steady velocity field $\boldsymbol{v}_2$. A large reduction from the pure acoustics solution is seen. (c) horizontal streaming components along the magenta dashed arrow in (b) for varying values of A. It is illustrated how the perpendicular slip velocity remains unchanged. (d) the vertical streaming components shown along the blue dashed arrow.

4.2 External electrodes

We now turn to the problem of shaping the ionic layer at the chamber walls by external means. This is done by placing electrodes in the surrounding solid to the fluid channel. The idea is to utilise the Debye-screening of the electric potential penetrating into the fluid chamber to generate a more desirable streaming pattern. To simplify the initial analysis, we consider the situation where no chemically generated surface charges are present at the fluid/solid boundary. All applied potentials (like the chemical zeta potential) are with respect to the charge neutral bulk of the fluid.

4.2.1 Perfect conductor model

When an electric potential penetrates into an ionic solution, it rapidly vanishes as it gets screened by the ions. This is reminiscent of the electronic screening at metallic surfaces and inspires the idea of modelling the ionic solution as a perfect conductor, when seen from the solid. We consider a solid/fluid interface positioned at $z = 0$ with the fluid above at $z > 0$. The solid below at $z < 0$ is characterised by the permittivity ϵ_s, the equilibrium electric potential ϕ_{eq}^s, and it contains no free charges. In the fluid above, we use ϵ_f, ϕ_{eq}^f, and we have a free charge-density described by Eq. (2.36). If we assume that the externally applied potential varies on a length-scale $d \gg \lambda_D$, then $\partial_y^2 \sim d^{-2}$ will be much smaller than $\partial_z^2 \sim \lambda_D^{-2}$ in the Poisson equation inside the fluid, such that $\nabla^2 \approx \partial_z^2$. Thus, the solution for the potential inside the fluid can again be approximated by the one-dimensional solution in Eq. (2.38), where we insert a slowly varying zeta potential

$$\zeta(y) = \phi_{eq}^f(y, z = 0) = \phi_{eq}^s(y, z = 0). \tag{4.7}$$

The boundary condition for the potential at the solid/fluid interface with no surface charges is

$$\epsilon_s \partial_z \phi_{eq}^s \big|_{z=0} = \epsilon_f \partial_z \phi_{eq}^f \big|_{z=0}. \tag{4.8}$$

Still working with $\nabla^2 \phi_{eq}^f \approx \partial_z^2 \phi_{eq}^f$, the total charge accumulated per area in the fluid above the wall $\sigma_{el,eq}$ is approximately given by

$$\sigma_{el,eq} = \int_0^\infty \rho_{el,eq} dz \approx -\epsilon_f \int_0^\infty \partial_z^2 \phi_{eq}^f dz = \epsilon_f \partial_z \phi_{eq}^f \big|_{z=0} = -\frac{2k_B T \epsilon_f}{\lambda_D Z e} \sinh\left(\frac{Z e \zeta(y)}{2 k_B T}\right), \tag{4.9}$$

where the expression in Eq. (2.38) has been inserted. The Debye layer is almost infinitesimally thin on the length scales of the devices we are interested in describing, and the accumulated charge above the wall looks a lot like a true surface charge. Inserting Eq. (4.9) into Eq. (4.8) yields

$$\partial_z \phi_{eq}^s \big|_{z=0} = \frac{1}{\epsilon_s} \sigma_{el,eq}, \tag{4.10}$$

which is equivalent to the boundary condition used for perfectly conducting surfaces with a boundary to a dielectric media of permittivity ϵ_s. Analogue to a metal, where electrons screen off incoming electric waves in a very thin layer at the surface of the metal, we have the same effect with ions at the solid/fluid interface.

Choosing $z = 0$ as the solid/fluid interface was arbitrary, and from Eq. (4.8) and Eq. (4.9) the zeta potential at an arbitrarily directed but flat wall at $\boldsymbol{r} = \boldsymbol{s}_0$ can be written as

$$\zeta(\boldsymbol{s}_0) = -\frac{2k_B T}{Z e} \text{arcsinh}\left(\frac{Z e \lambda_D}{2 k_B T} \frac{\epsilon_s}{\epsilon_f} \partial_\perp \phi_{eq}^s(\boldsymbol{s}_0)\right). \tag{4.11}$$

This expression can in turn be used as the boundary condition for ϕ_{eq}^s

$$\phi_{eq}^s(\boldsymbol{s}_0) = -\frac{2k_B T}{Z e} \text{arcsinh}\left(\frac{Z e \lambda_D}{2 k_B T} \frac{\epsilon_s}{\epsilon_f} \partial_\perp \phi_{eq}^s(\boldsymbol{s}_0)\right). \tag{4.12}$$

With this, we can estimate $\zeta(\boldsymbol{s}_0)$ without resolving the thin Debye layer on the fluid side of the geometry. Inserting Eq. (4.11) into the expression for the electroosmotic slip velocity at a flat wall at $\boldsymbol{s}_0$, we find

$$\boldsymbol{v}_{\text{slip}}^{\text{EO}} = \frac{2k_B T \epsilon_{\text{f}}}{Ze\eta} \text{arcsinh}\left(\frac{Ze\lambda_D}{2k_B T} \frac{\epsilon_{\text{s}}}{\epsilon_{\text{f}}} \partial_\perp \phi_{\text{eq}}^{\text{s}}(\boldsymbol{s}_0) \right) \boldsymbol{E}_{\text{ext}\parallel}. \tag{4.13}$$

We will refer to this as the effective model in this chapter. In case one wants to perform analytical evaluations of the potential at the fluid/solid boundary, one can apply a further simplification for certain cases. $\partial_\perp \phi_{\text{eq}}^{\text{s}}(\boldsymbol{s}_0)$ will of course depend on the value of $\zeta(\boldsymbol{s}_0)$ in general. With V_0 being the voltage applied to an external electrode, we will expect the normal derivative to scale approximately as

$$\partial_\perp \phi_{\text{eq}}^{\text{s}}(\boldsymbol{s}_0) \sim \frac{V_0 - \zeta(\boldsymbol{s}_0)}{d}. \tag{4.14}$$

Assuming that $\zeta(\boldsymbol{s}_0) \ll V_0$, we can expect $\partial_\perp \phi_{\text{eq}}^{\text{s}}(\boldsymbol{s}_0)$ to change very little by artificially truncating $\zeta(\boldsymbol{s}_0)$ to zero in the calculation of $\phi_{\text{eq}}^{\text{s}}$. In this case, we can use the following boundary condition on the potential on the solid side

$$\phi_{\text{eq}}^{\text{s}}(\boldsymbol{s}_0) = 0, \tag{4.15}$$

while the zeta potential to be used in the expression for the electroosmotic slip velocity is still found from Eq. (4.11). This allows for the use of image theory, which is illustrated in an example in the following. This model is referred to as the perfect conductor model in this chapter.

Eq. (2.48) with a full calculation of the Debye layer inside the fluid channel is compared to Eq. (4.13) with the boundary condition $\phi_{\text{eq}}^{\text{s}}(\boldsymbol{s}_0) = \zeta(\boldsymbol{s}_0)$ on the equilibrium potential. For the latter, no electric potential is calculated inside the fluid channel, and no boundary layers are needed in the finite element mesh. A simulation is set up where the standard fluid channel of dimensions $H_{\text{ch}} \times W_{\text{ch}} = 160\,\mu\text{m} \times 375\,\mu\text{m}$ is etched into a block of pyrex of dimensions $H_{\text{s}} \times W_{\text{s}} = 1\,\text{mm} \times 2\,\text{mm}$. A single cylindrical electrode of radius $R = 5\,\mu\text{m}$ is placed centrally beneath the fluid chamber. The edge-to-edge distance between the electrode and the fluid/solid boundary is denoted z_0. We assume no electric fields to be present in the surroundings of the devices in this thesis. On the outer boundary of the pyrex facing towards the surrounding environment, we assume no free charge accumulation, which will be formulated as

$$\hat{\boldsymbol{n}} \cdot \boldsymbol{D} = 0. \tag{4.16}$$

A constant horizontal external electric field is assumed to be applied across the fluid channel

$$\boldsymbol{E}_{\text{ext}} = -E\,\hat{\boldsymbol{e}}_y, \qquad E = 1\,\text{V}/W_{\text{ch}}. \tag{4.17}$$

This external electric field will be applied to all the following simulations of this chapter. The geometry and the boundary conditions used on the electric potential for the compared simulations are shown in figure 4.2. Solutions were found for these implementations for
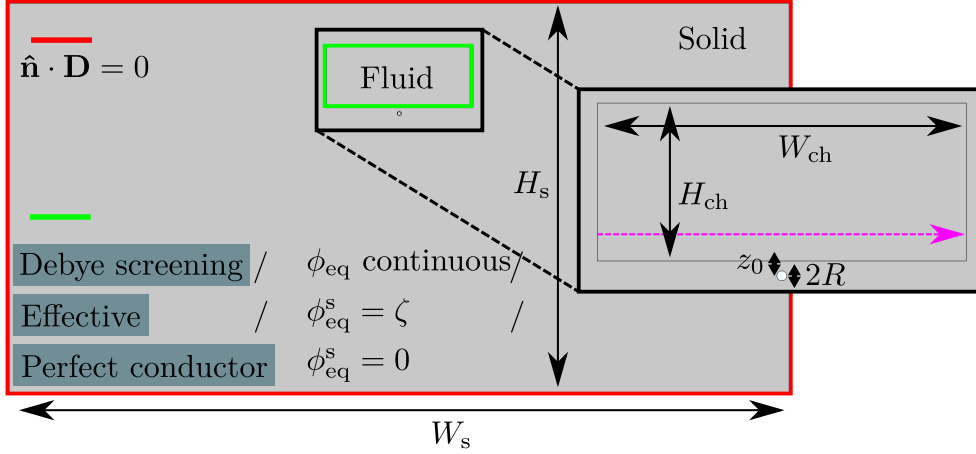
Figure 4.2: Geometry for the effective ζ-potential boundary condition test. The applied boundary conditions for the electric potential and the geometrical definitions are shown. The magenta dashed arrow illustrates the path along which v_{2y} is plotted in figure 4.3.

varying values of z_0. For each solution, the average value of the streaming amplitude $|\boldsymbol{v}_2|_\mathrm{avg}$ was found, and the relative difference between the methods was calculated

$$\frac{|\boldsymbol{v}_2|_\mathrm{avg}^\mathrm{eff} - |\boldsymbol{v}_2|_\mathrm{avg}^\mathrm{full}}{|\boldsymbol{v}_2|_\mathrm{avg}^\mathrm{full}}, \tag{4.18}$$

with full denoting the full model of the Debye screening and eff denoting the effective model. The relative error stemming from assuming the boundary condition $\phi_\mathrm{eq}^\mathrm{s}(\boldsymbol{s}_0) = 0$ was also tested. Selected solutions for the horizontal streaming component along the magenta dashed arrow in figure 4.2 are shown in figure 4.3 to illustrate the precision of the effective boundary condition.

We notice that the solutions are remarkably similar, even when the distance between the cylindrical electrode and the surface is only 10 nm and thus similar to the Debye length. Even for the perfect conductor model where we set $\phi_\mathrm{eq}^\mathrm{s}(\boldsymbol{s}_0) = 0$, a modest 2% relative difference is found in the average value of the streaming. The effective boundary condition with $\phi_\mathrm{eq}^\mathrm{s}(\boldsymbol{s}_0) = \zeta(\boldsymbol{s}_0)$ yields relative errors below 0.1% for all tested values of z_0. The model cannot be expected to hold, if the electrode introduces details in the physical fields on length scales comparable to 10 nm. However, at this short distance between the fluid/solid boundary and the wire, the radius of the wire partially determines the length scale of variation for the potential, which makes the effective model valid at these small distances. The simulation suggests that we may reach a 1% agreement already around $z_0 = 30$ nm for the perfect conductor model. In the following work, the distances between the fluid and the electrode boundaries are always greater than 1 μm, where a very high precision is seen for both effective models.

With the solid/fluid boundary modelled as a perfect conductor, we can use image theory to approximate the potential to check if our numerical implementation seems valid. A typical textbook calculation reveals that the potential around an infinite line-charge under
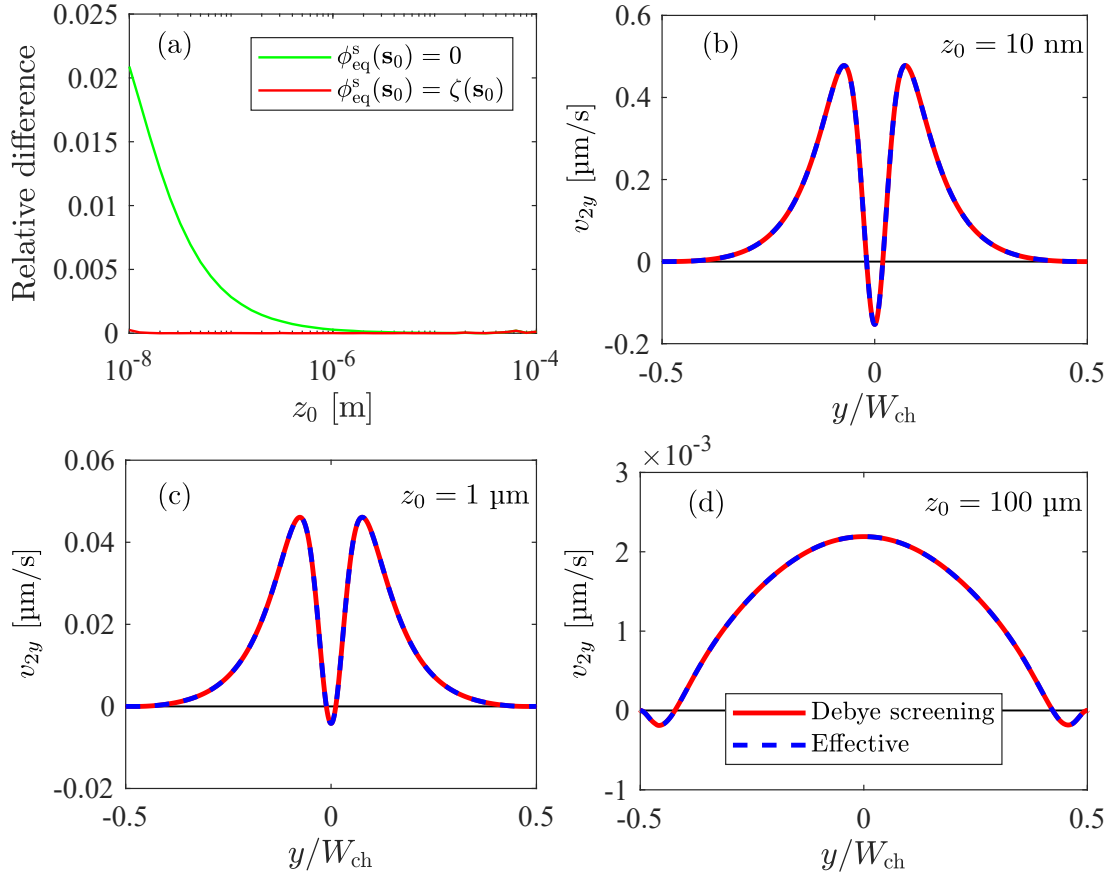
Figure 4.3: Test of effective boundary conditions for an external cylindrical electrode. The fields in (b)-(d) are plotted along the magenta dashed arrow shown in figure 4.2. (a) the relative difference between the full simulations including Debye screening and the effective model of the ζ potential. The perfect counductor model is tested too. (b) v_{2y} plotted for the $z_0 = 10\,\text{nm}$ solutions. (c) $z_0 = 1\,\mu\text{m}$ solutions. (d) $z_0 = 100\,\mu\text{m}$ solutions.

a semi-infinite and perfectly conducting plane forms cylindrical equipotential surfaces. From this, the potential around a cylindrical wire of potential V_0 centered in $(y, z) = (0, -(z_0 + R))$ with a semi-infinite conducting half-space at $z = 0$ is found to be

$$\phi(y, z) = \frac{V_0}{2\text{arccosh}(\frac{z_0+R}{R})} \ln\left[\frac{y^2 + \left(z - \sqrt{(z_0+R)^2 - R^2}\right)^2}{y^2 + \left(z + \sqrt{(z_0+R)^2 - R^2}\right)^2}\right]. \tag{4.19}$$

At $z = 0$, the z-derivative of this yields

$$\partial_z \phi(y, 0) = \frac{-2V_0}{\text{arccosh}(\frac{z_0+R}{R})} \frac{\sqrt{(z_0 + R)^2 - R^2}}{y^2 + (z_0 + R)^2 - R^2}. \tag{4.20}$$

In figure 4.4, this is compared to the normal derivatives of the electric potential at the bottom boundary found with the full and the effective model in the previous study of the
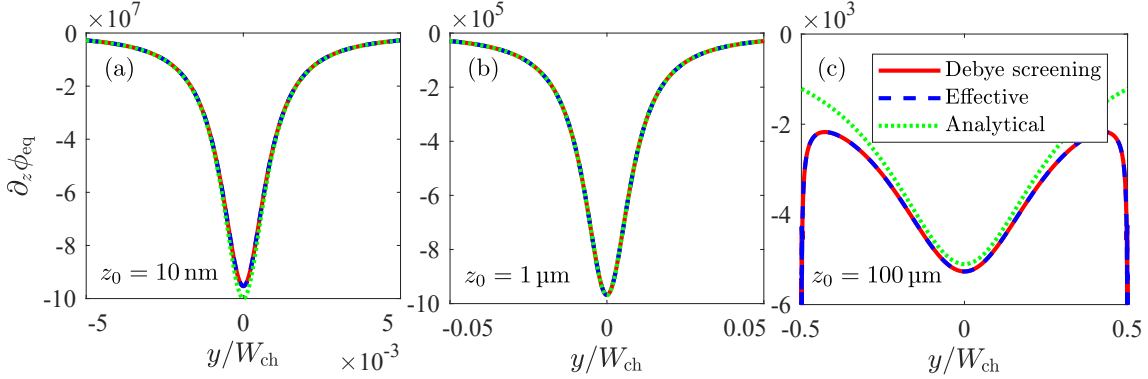
Figure 4.4: Boundary plots of the normal derivative of the equilibrium potential. The fields are plotted along the bottom boundary of the fluid chamber shown in figure 4.2. (a) $z_0 = 10\,\mathrm{nm}$ solutions. (b) $z_0 = 1\,\mu\mathrm{m}$ solutions. (c) $z_0 = 100\,\mu\mathrm{m}$ solutions.

effective theory. For $z_0 = 10\,\mathrm{nm}$, there is a slight mismatch between the numerical models and the analytical expression. The effective solution is seen to follow the full solution closely. For $z_0 = 1\,\mu\mathrm{m}$, all three solutions are almost identical, because the boundary appears essentially semi-infinite, while the distance between the wire and the fluid/solid boundary is still large enough for the perfect conductor boundary condition to be valid. For $z_0 = 100\,\mu\mathrm{m}$, the analytical solution does not fit as well with the numerical models anymore, because the finite bounds of the fluid chamber become important. However, the center peak value is still quite precise.

The effective boundary condition in Eq. (4.11) was also tested in a similar simulation with a rectangular electrode of dimensions $H_{\mathrm{elec}} \times W_{\mathrm{elec}} = 4\,\mu\mathrm{m} \times 10\,\mu\mathrm{m}$. The result of this test is shown in figure 4.5. We notice a similar convergence pattern to the previous test. The initial convergence of the perfect conductor model is a little worse than for the cylindrical wire, which is not surprising given that a rectangular wire has a larger surface at distance z_0 to the fluid/solid boundary. The relative error between the effective model and the full model is again negligible for all tested distances.

4.2.2   System optimisation

To probe for the most viable system designs to stop acoustic streaming, a series of numerical simulations with varying geometries are performed. A COMSOL script is set up to be ran through Matlab, and for each calculation a probe is taken of the average value for $|\boldsymbol{v}_2|$ in the fluid channel. This value is then minimised by changing the positioning of wires and the amplitudes of applied voltages. The minimisation process is automated by using the Matlab function *fminsearchcon* [27], which is an extension to Matlab's standard function *fminsearch*, which allows you to apply bounds and conditions to minimisation parameters. The minimisation method is a direct iterative simplex based method that does not use numerical or analytical gradients. For each iteration, a simplex of dimension $N + 1$ (with N being the number of minimisation parameters) is defined in parameter space $\mathbb{R}^N$, and

(a)

(b)
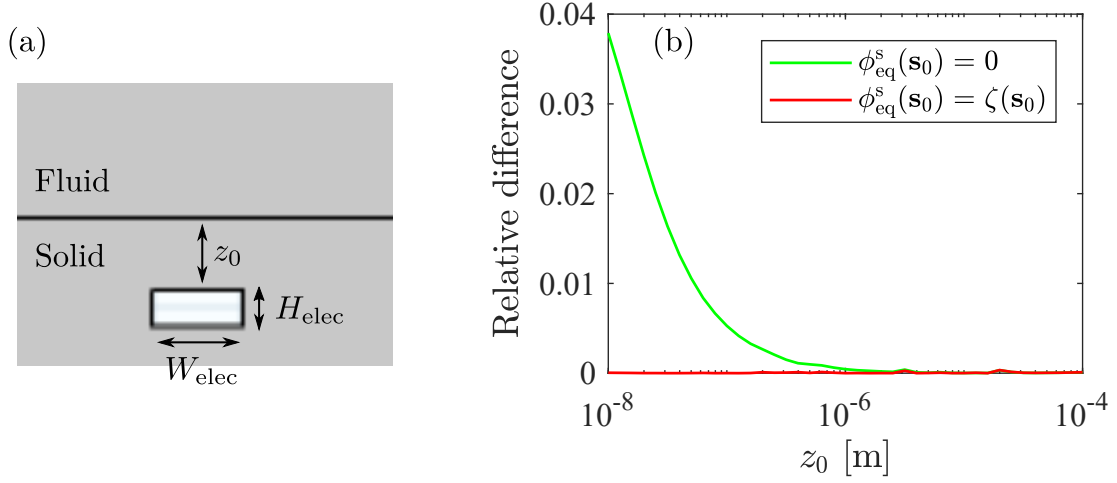
Figure 4.5: Effective boundary condition test for external rectangular wire. (a) Geometry of the simulation. (b) Relative difference in the average streaming $|\boldsymbol{v}_2|_{\text{avg}}$ between the effective models and the full boundary conditions with Debye screening.

the function that you are trying to optimise is evaluated in each vertex. Several test points are generated, and based on the function values at these test points, a new simplex is defined for the next iteration. The method is described in [28].

To model the potential extending from the electrodes, a rectangular geometry of the surrounding solid is implemented of dimensions $H_s \times W_s = 1.5 \, \text{mm} \times 4 \, \text{mm}$. The standard fluid channel cross section with the basic acoustics implemented is centralised in the solid. 1, 2 , and 3 cylindrical wires of radius R are used for each of the four streaming rolls. The setup has two axes of symmetry, and these are used to reduce the size of the simulations. Only one fourth of the setup is thus simulated, and the symmetry axes are supplied with boundary conditions to reflect the symmetries of the physical fields. The geometry alongside the applied boundary conditions are illustrated in figure 4.6. The wires are all aligned for each quarter, and the distance from the bottom of the fluid channel and the wires is denoted z_0. The distance from the vertical centreline to the edge of the first wire is called y_0, and the separation between each wire is called L. The applied potentials at the simulated wires are denoted V_1, V_2 and V_3. R, z_0, y_0, L, V_1, V_2, and V_3 all act as optimisation parameters. When we exclude the chemical zeta potential, the potential should be anti-symmetric around the vertical centreline at $y = 0$. Since the boundary condition in Eq. (4.13) is implemented, the equilibrium potential ϕ_{eq}^s is only simulated in the surrounding solid. The potential is set to zero on the vertical centreline and to ζ at the fluid/solid boundary. Since the setup is symmetric around the horizontal centreline, the normal derivative of the potential goes to zero here. Because the permittivity of the solid is a constant, this corresponds to the condition of no accumulated charge on a free surface

$$- \hat{\boldsymbol{n}} \cdot \epsilon_s \boldsymbol{\nabla} \phi_{\text{eq}}^s = \hat{\boldsymbol{n}} \cdot \boldsymbol{D} = 0. \tag{4.21}$$

(a)

(b)
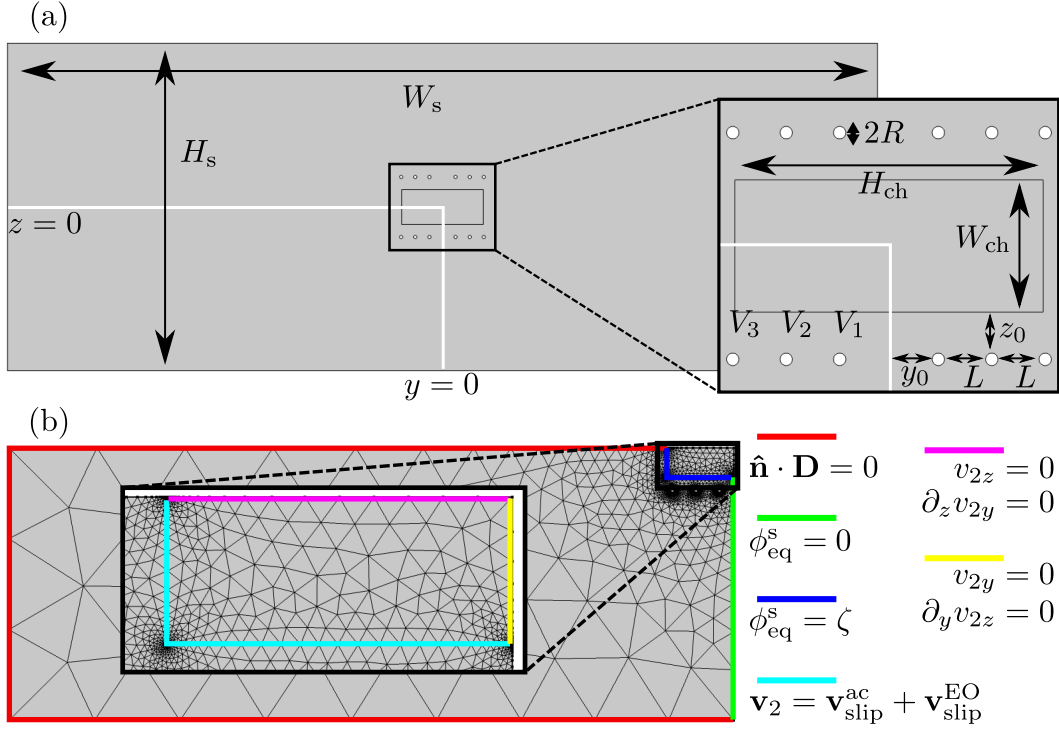
Figure 4.6: Geometry and boundary conditions for initial DC device optimisation. (a) full geometry shown, and the simulated quarter is cut out with white lines. 1, 2, or 3 cylindrical electrodes per quarter are implemented. In the figure, the example of 3 (in total 12) electrodes is shown. (b) mesh and boundary conditions applied to the simulations. The boundary conditions are illustrated with colour codes at the applied boundaries.

This boundary condition is also implemented on the surfaces facing towards the surrounding environment. Since the electric field is entirely horizontal, there is only an electroosmotic slip velocity on the top and bottom boundaries. From our previous discussion, we know that this should be sufficient to effectively suppress the streaming.

The optimal parameters and the corresponding value of the average streaming found for 1, 2, and 3 cylinders are shown in table 4.1. Field plots of the corresponding streaming solutions are shown in figure 4.7. The solution of the full geometry with 3 electrodes per quarter is also found for the optimised parameters. The solution for the full geometry finds an average streaming of $1.05\,\mu\text{m/s}$, which is identical to the solution utilising the geometric symmetries. A field plot of this solution is also shown in figure 4.7. Notably, with only a few electrodes we come quite close to the streaming reduction found for the idealised zeta potential control in the initial test. Even with a single electrode it is possible to reach a significant streaming reduction. The areas in which the streaming exceeds $3\,\mu\text{m/s}$ are illustrated on the field plots. These are seen to shrink for an increasing amount of cylindrical wires. Another way of evaluating the optimal setup could be to minimise the areas where the streaming exceeds a certain threshold. This principle was used in [14],

Table 4.1: Table of the optimal parameters found for the initial DC device optimisation test.

N_{elec}	V_1 [kV]	V_2 [kV]	V_3 [kV]	R [µm]	z_0 [µm]	y_0 [µm]	L [µm]	$|\boldsymbol{v}_2^{\text{d}}|_{\text{avg}}$ [µm/s]
1	13.395	-	-	4.25	61.48	84.78	-	1.38
2	22.197	0.113	-	1.22	71.47	88.29	80.06	1.12
3	25.043	0.004	0.002	1.20	75.83	90.87	63.17	1.05
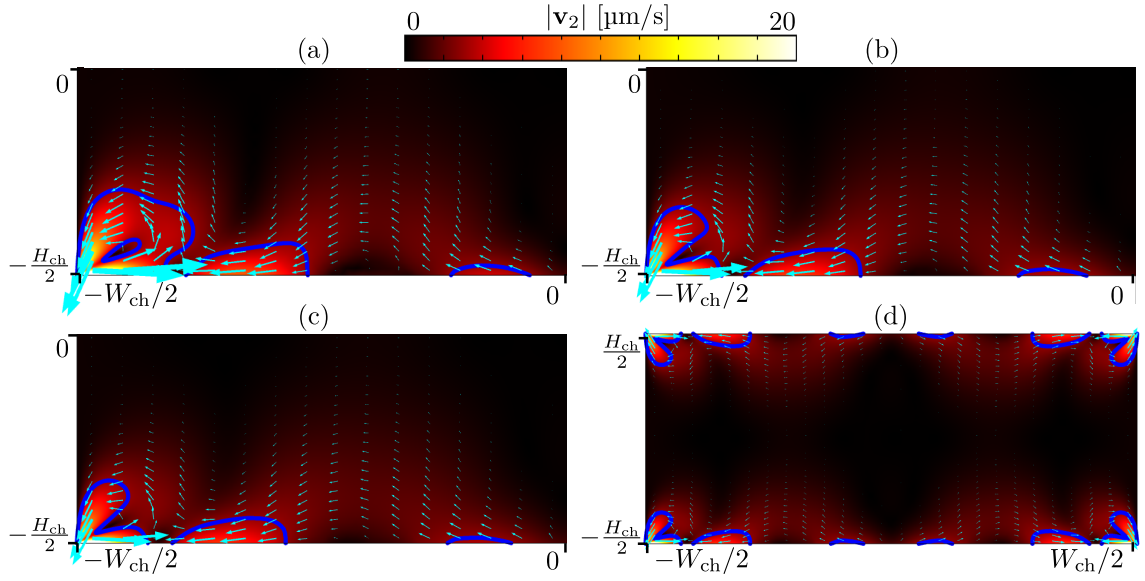
Figure 4.7: $\boldsymbol{v}_2$ field plots from the fluid of the initial optimised DC devices. The dark blue lines are contour lines for $|\boldsymbol{v}_2| = 3\,\text{µm/s}$. (a) single cylinder optimised solution. (b) double cylinder solution. (c) triple cylinder solution. (d) full geometry extension of (c).

where shape-optimisation was used to suppress acoustic streaming theoretically. Having small zones with a large streaming amplitude might not be that important in terms of particle handling, albeit it can cause large increases in the average streaming.

4.3 Practical considerations

We now discuss some of the problems with the design methods explored above. The main concerns will be how one would create a constant electric field across the fluid channel, how well we can manipulate streaming when a chemical zeta potential is present, and the very large amplitudes of applied external potentials in regards to the physical model and material properties.

4.3.1   Discussion of design weaknesses

In order to create an electric field going across the channel, one would have to deposit a set of electrodes on the sides of the channel. These electrodes would need to circumvent Debye screening in order to have the electric field penetrate through the bulk of the fluid. One way to go about this is to allow electrolysis to take place at the electrodes. However, electrolysis will generate unwanted gasses that you somehow have filter out of the chamber. Another problem with electrolysis is that it eventually leads to changes in pH, which changes the chemical properties of the surface of the solid, which in turn leads to changes in the chemical zeta potential.

One way of dealing with these problems has been to install anion exchange membranes at the electrodes [10]. A problem with this is that it is not necessarily an easy or cheap way of implementing the electroosmosis. It also leads to the question of how we would model the membranes acoustically.

Another idea is to use an electrode/electrolyte combination where the electrodes absorb one of the ion species, such as Cu electrodes with a $CuSO_4$ solution. This is often done in batteries, where the cation corresponds to the electrode material. However, this causes ramified growth on the electrodes, which would eventually compromise the structure of the chamber walls. An extensive model of this growth is presented in [29]. The process is quite complex, and the article does not discuss the amplitude of the potential extending into the bulk.

A relevant consideration in terms of the theoretical model is when the ionic concentrations become so large that steric effects must be taken into account. In the thin Debye layers, this actually happens at relatively low surface potentials. With a denoting the radius of an ion, the concentration surely cannot exceed a critical concentration of $c_{crit} = a^{-3}$. We consider a typical hydrated ion size of $a = 0.3$ nm. Assuming Eq. (2.34) to hold, the corresponding critical potential for $c_0 = 1$ mM of monovalent ions is found to be

$$\phi_{crit} = \frac{k_B T}{Ze} \ln\left(\frac{c_{crit}}{c_0}\right) = 11\, V_T, \qquad V_T = \frac{k_B T}{e}, \tag{4.22}$$

where we have defined the thermal voltage $V_T \approx 26$ mV at room temperature. Many models have been developed to take into account steric effects. A review is included in [30], where two simple models are also tested to explore steric effects at high voltages.

If we only want concentrations below approximately 1% of c_{crit}, where our model is still expected to hold, the surface potential should not exceed 160 mV. In the preceding simulations, the surface potentials have been below this but of the same order of magnitude. For a cylindrical wire, we can find an approximate expression for the peak amplitude of the surface potential with the perfect conductor model by using Eq. (4.11) with Eq. (4.20) inserted at $y = 0$

$$\zeta_{max} = \frac{2V_T}{Z} \operatorname{arcsinh}\left(\frac{Z\lambda_D}{2V_T} \frac{\epsilon_s}{\epsilon_f} \frac{2V_0}{\operatorname{arccosh}(\frac{z_0+R}{R})\sqrt{(z_0+R)^2 - R^2}}\right). \tag{4.23}$$

We select approximate values from the previous simulations, and for monovalent ions at 25°C and a cylinder of $R = 2\,\mu$m and $z_0 = 70\,\mu$m with $V_0 = 20$ kV applied, we find

$\zeta = 59\,\text{mV}$. So if we assume that we are able to generate a constant transverse external electric field of amplitude $1\,\text{V}/W_{\text{ch}}$ across the fluid channel, a surface potential of around 60 mV appears to be sufficient for suppressing typical acoustic streaming amplitudes. If transverse electric fields of this amplitude are practically difficult to generate, one would likely have to go into the steric regime to reach sufficient streaming amplitudes. However, the topics of steric effects, ramified growth, and ion selective membranes are beyond the scope of this thesis.

One last physical effect that we will mention is dielectric breakdown. For large enough electrical field strengths, all dielectric materials will eventually stop being dielectric and start conducting currents. This would likely compromise the experimental setup by Joule heating from electric discharges. For borosilicate glasses like pyrex, this happens around $20\,\text{MV/m}$ or $20\,\text{V/µm}$ [31]. This could prove to be an experimentally and theoretically relevant obstacle. The electric potentials needed to shape the ionic layers in the previous simulations were very large. From Eq. (4.9) we can estimate the perpendicular electrical field strength $|\boldsymbol{E}_\perp^{\text{s}}| = |\partial_\perp \phi_{\text{eq}}^{\text{s}}|$ needed at the edge of the solid to create a surface potential of 60 mV. For a pyrex/water interface at 25°C with monovalent ions in the water at bulk concentration $c_0 = 1\,\text{mM}$, and $\zeta = 60\,\text{mV}$, we find that $|\boldsymbol{E}_\perp^{\text{s}}| = 134\,\text{MV/m}$. This is much higher than the dielectric strength of pyrex, so some extra care must be taken to refine the design ideas using external wires. The needed field strength could potentially be lowered by applying larger transverse electric fields or by lowering the amplitude of the acoustic streaming. However, even if this was done, one would likely still have to counteract a chemical zeta potential at the fluid/solid boundary.

The chemical zeta potential varies with many parameters such as pH, temperature, bulk concentration of electrolytes, different types of electrolytes, and of course the type of solid surface. Silicate glass composites like pyrex generally have negative zeta potentials, which are reported to increase in amplitude for increasing pH values and decrease in amplitude for increasing bulk concentrations of electrolytes. To get an estimate of the values of the chemical zeta potential at $c_0 = 1\,\text{mM}$ for monovalent cations like sodium or potassium ions, we refer to the review article [32]. At pH values around 7, it is reported that zeta potentials for silicate glass composites are found to be somewhere around $-90\,\text{mV}$. To generate a surface potential of this amplitude, one would need $|\boldsymbol{E}_\perp^{\text{s}}| = 257\,\text{MV/m}$. In this thesis, we will not deal directly with this issue but only note a few potential possibilities for circumventing it. These may include increasing concentrations of ions, decreasing pH values, or using surface treatments to lower the surface potential [33][1]. Another option could be to change material from pyrex to e.g. fused silica. The review article [32] also mentions that zeta potentials of different types of silica glass do not vary significantly. The dielectric strength of fused silica is in the range of $470 - 670\,\text{MV/m}$, and the dielectric constant of fused silica is similar to that of pyrex at around 4.1 [31][2]. For further inspiration, one could consult the electrowetting literature, where dielectric breakdown is a large topic of discussion. A discussion of promising materials can be found in [34].

For now, we continue the analysis with pyrex and keep in mind that unreasonable

---

[1][33] presents an experimental and theoretical study of the effects of a surface coating on a silica surface. The observed reduction in the chemical surface potential for this coating is rather small.

[2]Measured at 1 MHz.
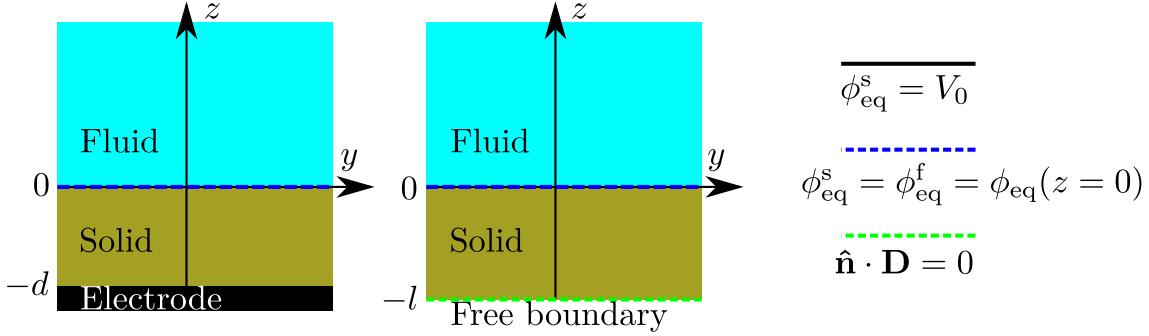
Figure 4.8: 1D example of a fluid/solid boundary with a chemical zeta potential. (a) electrode implemented in the solid beneath the fluid. (b) setup without external electrode.

potential values may be assessed by various optimisations to the design. Otherwise, one may have to use a more complicated models for the ionic behaviour to include steric effects. However, the problem of dielectric breakdown has to be dealt with in the design phase of any potential future experiments. In the proceeding, the chemical zeta potential is set to $\zeta_{\text{chem}} = -90\,\text{mV}$.

4.3.2 Including the chemical zeta potential

We now turn to the topic of counteracting the chemical zeta potential, while simultaneously creating a total surface potential to generate streaming rolls opposite to the Rayleigh streaming.

First, we need to consider the boundary condition at the fluid/solid interface. The chemical zeta potential does not materialise out of nothing. It stems from the chemical binding of charges on the fluid side of the interface. This means that there will be an actual surface charge $\sigma_{\text{el,chem}}$ on the boundary. Again, denoting the equilibrium potential in the fluid $\phi_{\text{eq}}^{\text{f}}$ and in the solid $\phi_{\text{eq}}^{\text{s}}$, the boundary conditions on the potential at the fluid/solid boundary in the presence of an actual surface charge $\sigma_{\text{el,chem}}$ created by surface chemistry, reads

$$-\epsilon_{\text{f}}\hat{\boldsymbol{n}} \cdot \boldsymbol{\nabla}\phi_{\text{eq}}^{\text{f}} + \epsilon_{\text{s}}\hat{\boldsymbol{n}} \cdot \boldsymbol{\nabla}\phi_{\text{eq}}^{\text{s}} = \sigma_{\text{el,chem}}, \qquad \text{for} \quad \boldsymbol{r} \in \boldsymbol{s}_0, \qquad (4.24\text{a})$$

$$\phi_{\text{eq}}^{\text{f}} = \phi_{\text{eq}}^{\text{s}} = \phi_{\text{eq}}(\boldsymbol{s}_0), \quad \text{for} \quad \boldsymbol{r} \in \boldsymbol{s}_0. \qquad (4.24\text{b})$$

Because our theory is formulated around a constant chemical surface potential ζ_{chem} and not the more physical $\sigma_{\text{el,chem}}$, things become slightly awkward. We begin with a 1D electrostatic example, where a solid/fluid interface at $z = 0$ and an electrode at $z = -d$ is considered as illustrated in figure 4.8 (a). Besides the boundary conditions in Eq. (4.24), we have

$$\phi_{\text{eq}}^{\text{s}}(z = -d) = V_0, \qquad (4.25\text{a})$$

$$\phi_{\text{eq}}^{\text{f}}(z \to \infty) = 0. \qquad (4.25\text{b})$$

In the solid at $-d < z < 0$, the potential is found from

$$\nabla^2 \phi_{\text{eq}}^{\text{s}} = 0 \quad \Rightarrow \quad \phi_{\text{eq}}^{\text{s}} = Az + B. \tag{4.26}$$

With Eq. (4.24b) and Eq. (4.25a) we get

$$\phi_{\text{eq}}^{\text{s}} = \phi_{\text{eq}}(z = 0) - [V_0 - \phi_{\text{eq}}(z = 0)]\frac{z}{d}. \tag{4.27}$$

In the fluid at $z > 0$, the potential is found with the boundary condition in Eq. (4.25b) to be

$$\nabla^2 \phi_{\text{eq}}^{\text{f}} = \frac{2Zec_0}{\epsilon_{\text{f}}} \sinh\left(\frac{Ze}{k_{\text{B}}T}\phi_{\text{eq}}^{\text{f}}\right) \quad \Rightarrow$$
$$\phi_{\text{eq}}^{\text{f}} = \frac{4k_{\text{B}}T}{Ze}\text{arctanh}\left[\tanh\left(\frac{Ze\phi_{\text{eq}}(z = 0)}{4k_{\text{B}}T}\right)\exp\left(-\frac{z}{\lambda_{\text{D}}}\right)\right]. \tag{4.28}$$

Denoting $\phi_{\text{eq}}(z = 0) = \zeta$, the last boundary condition in Eq. (4.24a) yields

$$\frac{2k_{\text{B}}T\epsilon_{\text{f}}}{Ze\lambda_{\text{D}}} \sinh\left(\frac{Ze\zeta}{2k_{\text{B}}T}\right) + \epsilon_{\text{s}}\frac{\zeta - V_0}{d} = \sigma_{\text{el,chem}}. \tag{4.29}$$

We wish to relate $\sigma_{\text{el,chem}}$ to the chemical zeta potential ζ_{chem}. This chemically generated potential should be unchanged if no conductor was placed beneath the fluid. Instead of a conductor at $z = -d$, we could just place a dielectric media characterised by ϵ_{s} beneath the fluid with an edge with no free charges at $z = -l$. At this edge we have the boundary condition $\hat{\boldsymbol{n}} \cdot \boldsymbol{D} = 0$. This is illustrated in figure 4.8 (b). In the solid we then find

$$\phi_{\text{eq}}^{\text{s}}(z) = \phi_{\text{eq}}(z = 0), \tag{4.30}$$

and again in the fluid

$$\phi_{\text{eq}}^{\text{f}} = \frac{4k_{\text{B}}T}{Ze}\text{arctanh}\left[\tanh\left(\frac{Ze\phi_{\text{eq}}(z = 0)}{4k_{\text{B}}T}\right)\exp\left(-\frac{z}{\lambda_{\text{D}}}\right)\right]. \tag{4.31}$$

Since there is no external electrode, $\phi_{\text{eq}}(z = 0) = \zeta_{\text{chem}}$, and Eq. (4.24a) yields

$$\sigma_{\text{el,chem}} = \frac{2k_{\text{B}}T\epsilon_{\text{f}}}{Ze\lambda_{\text{D}}} \sinh\left(\frac{Ze\zeta_{\text{chem}}}{2k_{\text{B}}T}\right). \tag{4.32}$$

Inserting this in Eq. (4.29), we find that

$$\zeta = \frac{2k_{\text{B}}T}{Ze}\text{arcsinh}\left[\frac{Ze\lambda_{\text{D}}}{2k_{\text{B}}T}\frac{\epsilon_{\text{s}}}{\epsilon_{\text{f}}}\frac{(V_0 - \zeta)}{d} + \sinh\left(\frac{Ze\zeta_{\text{chem}}}{2k_{\text{B}}T}\right)\right]. \tag{4.33}$$

For the case illustrated in figure 4.8 (a) we had

$$\partial_z \phi_{\text{eq}}^{\text{s}} = -\frac{V_0 - \zeta}{d}, \tag{4.34}$$

and Eq. (4.33) can also be expressed as

$$\zeta = \frac{2k_{\mathrm{B}}T}{Ze}\mathrm{arcsinh}\left[\sinh\left(\frac{Ze\zeta_{\mathrm{chem}}}{2k_{\mathrm{B}}T}\right) - \frac{Ze\lambda_{\mathrm{D}}}{2k_{\mathrm{B}}T}\frac{\epsilon_{\mathrm{s}}}{\epsilon_{\mathrm{f}}}\partial_z\phi_{\mathrm{eq}}^{\mathrm{s}}\right]. \tag{4.35}$$

Next, we consider a general geometry with a solid/fluid boundary at $\boldsymbol{s}_0$. We still assume no free charge accumulation at the surfaces facing the surrounding environment. The electric potential in the solid is determined by

$$\nabla^2\phi_{\mathrm{eq}}^{\mathrm{s}} = 0, \tag{4.36}$$

and the solution with no external electrodes would still just be $\phi_{\mathrm{eq}}^{\mathrm{s}}(\boldsymbol{r}) = \zeta_{\mathrm{chem}}$. This follows from the uniqueness theorems of the Laplace equation, since all boundary conditions on the closed domain of the surrounding solid are either Dirichlet or Neumann. With a constant chemical zeta potential at the boundary of the fluid channel, the solution for the electric field in the fluid is essentially one-dimensional, because the Debye layer is much smaller than the chamber dimensions. The charge per area accumulating over a given area of the wall is then still

$$\sigma_{\mathrm{el,chem}} = \frac{2k_{\mathrm{B}}T\epsilon_{\mathrm{f}}}{Ze\lambda_{\mathrm{D}}}\sinh\left(\frac{Ze\zeta_{\mathrm{chem}}}{2k_{\mathrm{B}}T}\right). \tag{4.37}$$

If an external electrode applies an electric potential that varies on a length scale $d \gg \lambda_{\mathrm{D}}$ along the boundary, the electric potential in the fluid still approximately follows the Gouy-Chapman solution

$$\phi_{\mathrm{eq}}^{\mathrm{f}} = \frac{4k_{\mathrm{B}}T}{Ze}\mathrm{arctanh}\left[\tanh\left(\frac{Ze\zeta(\boldsymbol{s}_0)}{4k_{\mathrm{B}}T}\right)\exp\left(-\frac{Z}{\lambda_{\mathrm{D}}}\right)\right], \tag{4.38}$$

where Z again denotes the locally perpendicular coordinate pointing into the fluid. Inserting Eq. (4.37) and Eq. (4.38) into Eq. (4.24a) then leads to

$$\zeta(\boldsymbol{s}_0) = \frac{2k_{\mathrm{B}}T}{Ze}\mathrm{arcsinh}\left[\sinh\left(\frac{Ze\zeta_{\mathrm{chem}}}{2k_{\mathrm{B}}T}\right) - \frac{Ze\lambda_{\mathrm{D}}}{2k_{\mathrm{B}}T}\frac{\epsilon_{\mathrm{s}}}{\epsilon_{\mathrm{f}}}\partial_\perp\phi_{\mathrm{eq}}^{\mathrm{s}}(\boldsymbol{s}_0)\right]. \tag{4.39}$$

This is implemented in the electroosmotic slip velocity, and $\phi_{\mathrm{eq}}^{\mathrm{s}}$ is calculated with the boundary condition

$$\phi_{\mathrm{eq}}^{\mathrm{s}}(\boldsymbol{s}_0) = \frac{2k_{\mathrm{B}}T}{Ze}\mathrm{arcsinh}\left[\sinh\left(\frac{Ze\zeta_{\mathrm{chem}}}{2k_{\mathrm{B}}T}\right) - \frac{Ze\lambda_{\mathrm{D}}}{2k_{\mathrm{B}}T}\frac{\epsilon_{\mathrm{s}}}{\epsilon_{\mathrm{f}}}\partial_\perp\phi_{\mathrm{eq}}^{\mathrm{s}}(\boldsymbol{s}_0)\right]. \tag{4.40}$$

More elaborate models can be applied, where surface reactions are taken into account to determine electric surface charges $\sigma_{\mathrm{el,chem}}$. Thorough work on this topic can e.g. be found in [33].

4.3.3   Electrode array design

In our next design idea, we take into account that it would likely be easier for fabrication processes to make rectangular electrodes rather than cylindrical ones. In order to reduce

Table 4.2: Table of the optimal parameters found for the DC device optimisation test with a array of 18 rectangular electrodes. The setups $A - F$ are illustrated in figure 4.9.

Setup	A	B	C	D	E	F
V_{sin} [V]	-	616	-	-	-	632
V_0 [V]	-	-	-	1498	-	1507
$|\mathbf{v}_2|_{\text{avg}}$ [µm/s]	28.5	1.28	66.8	2.07	68.1	2.35

the amplitudes of the applied potentials as much as possible, it would also be beneficial to decrease the distance between electrodes and the fluid chamber. The optimised solutions shown above all had distances between electrodes and the fluid/solid boundary comparable to the width of the chamber. This was of course because the potential had to spread out over the entire boundary to counteract the acoustic streaming. If electrodes are situated closer to the boundary, more electrodes would be needed to generate a desirable shape of the surface potential.

We attempt a design with two arrays of 18 rectangular electrodes of dimension $H_{\text{elec}} \times W_{\text{elec}} = 4\,\text{µm} \times 10\,\text{µm}$ with $10\,\text{µm}$ spacing between neighbouring electrodes. Similar to the previous optimisation simulations illustrated in figure 4.6, the fluid channel is etched centrally into a pyrex cross section of dimensions $W_{\text{s}} = 1.5\,\text{mm} \times 4\,\text{mm}$. The arrays of electrodes are placed centrally $5\,\text{µm}$ beneath and above the fluid channel, respectively. With the applied chemical zeta potential, the problem is still symmetric along the horizontal centreline at $z = 0$. This symmetry axis was used in the simulations, and a zoom-in on the fluid channel of the simulated geometry is illustrated in figure 4.9. In order to counteract both the chemical zeta potential and the Rayleigh-like acoustic streaming rolls, we want to create a wall potential, which looks like a sinusoidal curve with a constant elevation. A direct optimisation method like the Matlab *fminsearch* is not suited to minimise 18 parameters, when every function evaluation takes several seconds. Instead, the applied electrode potentials were set to follow

$$V_n = V_0 + V_{\text{sin}} \sin\left((18 - (2n - 1))\pi \frac{2W_{\text{elec}}}{W_{\text{ch}}} \right), \qquad n = 1, 2, ..., 18. \qquad (4.41)$$

Here, V_1 is applied to the leftmost electrode in the geometry, V_2 is applied to the neighbouring electrode, and so on. With this, only the two parameters V_0 and V_{sin} are varied. The applied external transverse electric field still follows the form in Eq. (4.17). First, no chemical zeta potential is included, and only the acoustic streaming has to be counteracted by V_{sin}. Next, no acoustics are included, and only the chemical zeta potential has to be counteracted by V_0. Lastly, all effects are included together. The optimised solutions are also shown in figure 4.9. The average streaming velocities with and without the external electrode potential are given in table 4.2.

An effective streaming reduction is achieved both with and without the chemical zeta potential. This is reflected both in the low average streaming velocity and in the very restricted areas where the velocity of the fluid exceeds $3\,\text{µm/s}$. Notably, the setup has trouble with reducing the streaming close to the top and bottom boundaries, although large areas in the bulk show very low streaming velocities, when the optimised potentials
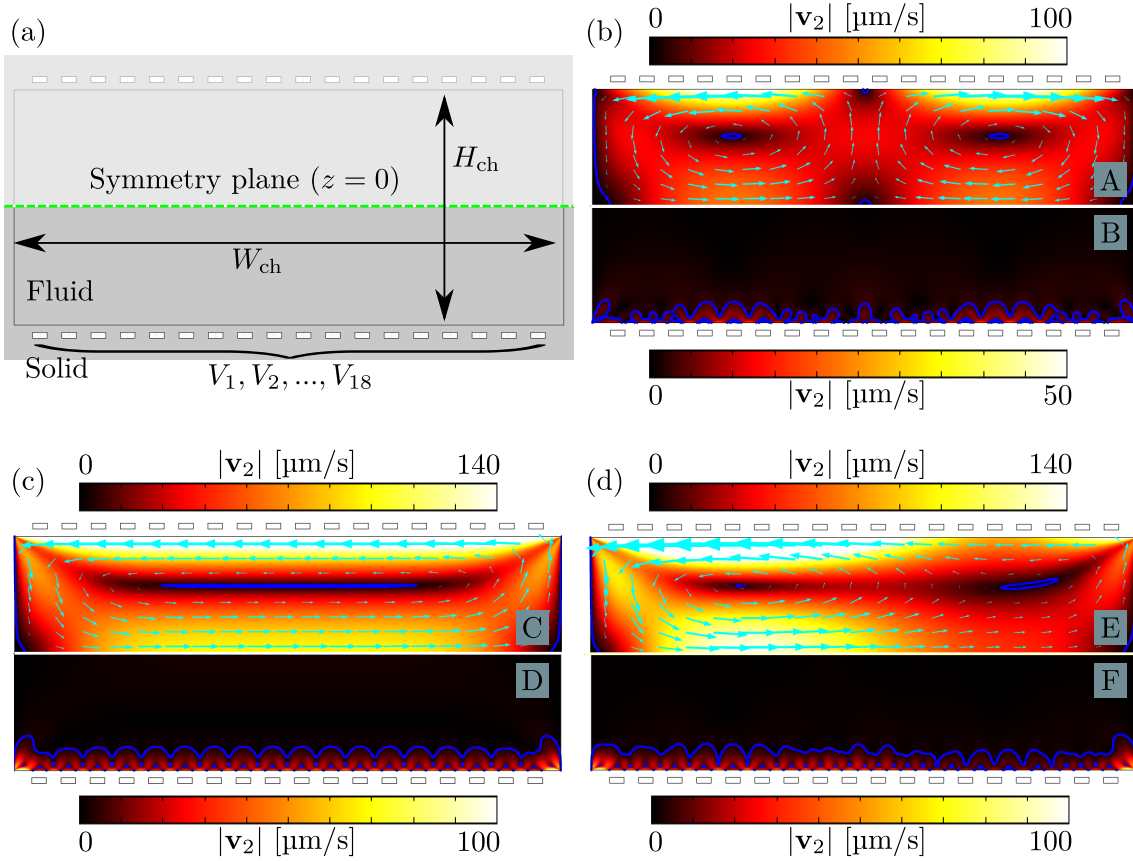
Figure 4.9: Optimisation of 18 rectangular electrode potentials. The blue lines mark contours for $|\boldsymbol{v}_2| = 3\,\mu\text{m/s}$. (a) fluid channel and surrounding electrodes of the simulated geometry. 18 evenly spaced rectangular electrodes are implemented above and beneath the channel, and a horizontal symmetry line at $z = 0$ is used to cut the geometry in half. (b) solutions without ζ_{chem} implemented. A shows the solution with no applied potential, and B is the solution with counter streaming generated by electroosmosis. (c) solutions without acoustics and only ζ_{chem} implemented. C has zero applied potential on the external electrodes, and D shows the optimised solution. (d) solutions with ζ_{chem} and acoustics with and without counter streaming from electroomosis.

are applied. Even though large streaming amplitudes are seen at the boundaries, the large areas with heavily restricted streaming could be interesting for experimental purposes.

One could likely increase the performance of a system like this by decreasing the chemical zeta potential, increasing the number of electrodes etc. The required applied voltages are still very high, but one could also place the electrodes even closer to the boundary. Some experiments with electroosmosis have e.g. separated the electrodes from the electrolyte by a thin layer of oxide [35]. This of course does not circumvent the problem of high electrical fields, as these scale with the distance between the wire and the fluid channel. In [9] they even made direct contact between the driving electrodes and the fluid in an AC electroosmotic setup. One could also look into this possibility in future work.

Instead of attempting a thorough optimisation scheme of systems based on direct current electroosmosis, we instead turn to the interesting phenomena of induced charge electroosmosis. This method in principle has some inherent advantages compared to DC electroosmosis, and it is thus worthwhile exploring it.

5 | Induced-charge electroosmosis

Induced charge electroosmosis (ICEO) is the principle of generating electroosmotic flows by purely capacitative means. To do this, AC potentials are utilised to bring about a harmonic pull and push motion of the ions, which generates a body force in the fluid due to viscous drag on the ions. While the phenomena may seem more complicated than DC electroomosis, since the ions are no longer in a simple equilibrium formation, it benefits from not having to exchange any charges at the electrodes to prevent screening. With this method, we can hope to circumvent the need of electrolysis or ramified growth.

Early work by Ajdari in 2000 suggested how the effect could be used for creating micropumps by utilising certain asymmetries in the applied potentials [8]. Micropumps were also realised experimentally and displayed flow velocities in the $100\,\mu\text{m/s}$ range [9]. This naturally makes ICEO interesting for the purpose of suppressing acoustic streaming. While common applications focus on pumping fluid along a channel, we will study the capabilities of the technique to pump fluid around in a cross section.

5.1 Governing equations

5.1.1 General case

The initial theoretical exploration is largely inspired by [36], which extends and clarifies the theory presented in [8]. We will not include any chemical zeta potential at the fluid/solid boundary in our treatment of ICEO. A brief discussion of this is given later. For now, we just imagine that the theoretical examples reflect microchannels where a surface treatment has removed chemically generated surface charges. We still assume a quasi-electrostatic treatment to be reasonable, so the electric field is governed by the Poisson equation. We also consider a simple ionic solution of a single monovalent cation with a corresponding monovalent anion. The ionic motion is still governed by the Nernst–Planck equation in Eq. (2.26a), but an equilibrium solution can no longer be assumed. The fluid flow is still of sufficiently low amplitude to ignore the non-linear advective term in the Navier–Stokes

equation. The full system of governing equations thus becomes

$$\partial_t c_\pm = -\boldsymbol{\nabla} \cdot (c_\pm \boldsymbol{v} - D_\pm \boldsymbol{\nabla} c_\pm - \mu_\pm c_\pm \boldsymbol{\nabla} \phi), \tag{5.1a}$$

$$\nabla^2 \phi = -\frac{1}{\epsilon_{\mathrm{f}}} \rho_{\mathrm{el}}, \tag{5.1b}$$

$$0 = \boldsymbol{\nabla} \cdot \boldsymbol{v}, \tag{5.1c}$$

$$\rho \partial_t \boldsymbol{v} = -\boldsymbol{\nabla} p + \eta \nabla^2 \boldsymbol{v} - \rho_{\mathrm{el}} \boldsymbol{\nabla} \phi. \tag{5.1d}$$

The fluid velocity fulfils the no-slip boundary condition. The boundary condition on the electric potential rises from external electrodes shaping some surface potential at the fluid boundary. Finally, a zero normal flux of ions is imposed at the walls. The full set of boundary conditions thus reads

$$\boldsymbol{v}(\boldsymbol{s}_0, t) = \boldsymbol{0}, \tag{5.2a}$$

$$\phi(\boldsymbol{s}_0, t) = V_{\mathrm{ext}}(\boldsymbol{s}_0, t), \tag{5.2b}$$

$$0 = \hat{\boldsymbol{n}} \cdot (-D_\pm \boldsymbol{\nabla} c_\pm - \mu_\pm c_\pm \boldsymbol{\nabla} \phi)\big|_{\boldsymbol{r}=\boldsymbol{s}_0}. \tag{5.2c}$$

The general system of equations is difficult to work with and offers little to no possibilities in terms of analytical work. Instead of going directly towards full numerical solutions, we start the analysis in a heavily simplified regime.

5.1.2 Linearised equations

We initially consider the case where only weak external potentials are applied. To reach experimentally relevant amplitudes for the streaming, we expect that it will be necessary to abandon these simplifying assumptions. Thus, it is likely that we eventually have to analyse the full set of equations in Eq. (5.1).

First, we simplify the equations by considering the case where $D_+ = D_- = D$, such that $\mu_+ = -\mu_- = \mu$. This could be a first approximation for a solution of KCl, where K$^+$ and Cl$^-$ have very similar diffusivities. Assuming that the applied potentials only slightly perturb the ionic densities, we write

$$c_\pm = c_0 + \delta c_\pm, \qquad \delta c_\pm \ll c_0. \tag{5.3}$$

This essentially brings us in the Debye-Hückel regime, requiring that $V_{\mathrm{ext}} \ll V_{\mathrm{T}}$. With this, we make the following approximation for the ionic flux expressions

$$c_\pm \boldsymbol{\nabla} \phi \approx c_0 \boldsymbol{\nabla} \phi. \tag{5.4}$$

Furthermore, we introduce the notation

$$\nu = c_+ - c_- = \delta c_+ - \delta c_-. \tag{5.5}$$

Subtracting the positive and the negative version of Eq. (5.1a) and inserting Eq. (5.1b), we find that

$$\partial_t \nu = \left[D\nabla^2 - D\frac{1}{\lambda_{\mathrm{D}}^2} - (\boldsymbol{v} \cdot \boldsymbol{\nabla}) \right] \nu. \tag{5.6}$$

Lastly, we work in the diffusive limit where

$$(\boldsymbol{v} \cdot \boldsymbol{\nabla}) \ll D\nabla^2 - \frac{D}{\lambda_{\mathrm{D}}^2}, \tag{5.7}$$

corresponding to $|v_\perp|/\lambda_{\mathrm{D}} + |\boldsymbol{v}_\parallel|/d \ll D/d^2$, where d is the typical length scale for variations parallel to the boundary. It is implicit in this scaling argument that ν still only exists in a thin layer (of length scale λ_{D}) at the boundary, and that the two terms on the right-hand side partially cancel each other. The linearised system of equations then becomes

$$\partial_t \nu = \left[D\nabla^2 - D\frac{1}{\lambda_{\mathrm{D}}^2} \right]\nu, \tag{5.8a}$$

$$\nabla^2 \phi = -\frac{Ze}{\epsilon_{\mathrm{f}}}\nu, \tag{5.8b}$$

$$0 = \boldsymbol{\nabla} \cdot \boldsymbol{v}, \tag{5.8c}$$

$$\rho\partial_t \boldsymbol{v} = -\boldsymbol{\nabla}p + \eta\nabla^2\boldsymbol{v} - Ze\nu\boldsymbol{\nabla}\phi. \tag{5.8d}$$

The positive and negative version of Eq. (5.2c) are also subtracted, and the low potential assumption is applied to reach

$$0 = \hat{\boldsymbol{n}} \cdot \left[\boldsymbol{\nabla}\nu + \frac{\epsilon_{\mathrm{f}}}{Ze\lambda_{\mathrm{D}}^2}\boldsymbol{\nabla}\phi \right]_{\boldsymbol{r}=\boldsymbol{s}_0}. \tag{5.9}$$

With this, the electrostatic problem in Eq. (5.8a) and Eq. (5.8b) can be solved with boundary conditions Eq. (5.2b) and Eq. (5.9) independent of the flow problem. In turn, the calculated electric body force can be inserted in the fluid dynamical equations in Eq. (5.8c) and Eq. (5.8d), which are solved with the no-slip boundary condition Eq. (5.2a). This is in essence similar to the way we treat the acoustic streaming calculations with a perturbation series.

5.1.3 External AC potential

When an external AC potential is applied of the form

$$V_{\mathrm{ext}}(\boldsymbol{s}_0, t) = \mathrm{Re}\{V_{\mathrm{ext}}(\boldsymbol{s}_0)\,\mathrm{e}^{-\mathrm{i}\omega t}\}, \tag{5.10}$$

the linearised electrostatic fields can be recast in phasor notation where

$$\nu(\boldsymbol{r}, t) = \mathrm{Re}\{\nu(\boldsymbol{r})\,\mathrm{e}^{-\mathrm{i}\omega t}\}, \qquad \phi(\boldsymbol{r}, t) = \mathrm{Re}\{\phi(\boldsymbol{r})\,\mathrm{e}^{-\mathrm{i}\omega t}\}. \tag{5.11}$$

With these, $\partial_t = -\mathrm{i}\omega$ in Eq. (5.8a). The electric body force then becomes

$$\begin{aligned}
\boldsymbol{f}_{\mathrm{b}} &= -Ze\,\mathrm{Re}\{\nu(\boldsymbol{r})\,\mathrm{e}^{-\mathrm{i}\omega t}\}\mathrm{Re}\{\boldsymbol{\nabla}\phi(\boldsymbol{r})\,\mathrm{e}^{-\mathrm{i}\omega t}\} \\
&= -\frac{Ze}{2}\big(\mathrm{Re}\{\nu(\boldsymbol{r})\boldsymbol{\nabla}\phi^*(\boldsymbol{r})\} + \mathrm{Re}\{\nu(\boldsymbol{r})\boldsymbol{\nabla}\phi(\boldsymbol{r})\,\mathrm{e}^{-\mathrm{i}2\omega t}\}\big).
\end{aligned} \tag{5.12}$$

This will give rise to a flow oscillating at double frequency 2ω alongside a steady streaming field, such that

$$\boldsymbol{v}(\boldsymbol{r}, t) = \boldsymbol{v}(\boldsymbol{r}) + \mathrm{Re}\{\boldsymbol{v}^{(2\omega)}(\boldsymbol{r})\,\mathrm{e}^{-\mathrm{i}2\omega t}\}, \tag{5.13a}$$

$$p(\boldsymbol{r}, t) = p(\boldsymbol{r}) + \mathrm{Re}\{p^{(2\omega)}(\boldsymbol{r})\,\mathrm{e}^{-\mathrm{i}2\omega t}\}. \tag{5.13b}$$

The oscillating velocity can be used to produce mixers in microsystems, but we will be interested in the time-averaged effect for particle sorting. To summarise, we calculate the time-averaged streaming induced by an AC source in the weakly non-linear regime by initially calculating the complex electrostatic phasors through

$$-\mathrm{i}\omega\nu = \left[D\nabla^2 - D\frac{1}{\lambda_{\mathrm{D}}^2}\right]\nu, \tag{5.14a}$$

$$\nabla^2\phi = -\frac{Ze}{\epsilon_{\mathrm{f}}}\nu, \tag{5.14b}$$

with the boundary conditions in Eq. (5.2b) and Eq. (5.9). With these, the time-averaged electric body force is determined, and the steady flow is calculated from

$$0 = \boldsymbol{\nabla}\cdot\boldsymbol{v}, \tag{5.15a}$$

$$\boldsymbol{0} = -\boldsymbol{\nabla}p + \eta\nabla^2\boldsymbol{v} - \frac{Ze}{2}\mathrm{Re}\{\nu\boldsymbol{\nabla}\phi^*\}, \tag{5.15b}$$

and the no-slip boundary condition. Here, $\boldsymbol{v} = \boldsymbol{v}(\boldsymbol{r})$ and $p = p(\boldsymbol{r})$ denote the time-averaged fluid fields.

   If one wanted to include a chemical zeta potential in the theory, it would lead to some initial equilibrium charge density

$$\nu = \nu_{\mathrm{eq}} + \nu_{\mathrm{ext}}. \tag{5.16}$$

The application of external fields would also drag the equilibrium ions to generate a flow oscillating at angular frequency ω. It is not clear if one could assume the time-averaged problem to be unaffected by this. Because the chemical zeta potential can be relatively large, the generated flow could couple into the time-averaged problem through the advective term in the Nernst–Planck equation. Further, when modulating the surface charge with an external AC-potential, one would reach the steric regime at lower applied peak-to-peak voltages, if a chemical zeta potential contributes to the charge density. In this thesis, we keep things simple and assume no chemical zeta potential to be present.

5.2   Effective boundary conditions

In [36] the problem of an infinite half-plane of fluid with a sinusoidal potential applied beneath a thin insulating layer is analysed. An external potential at the solid/fluid boundary at $z = 0$ follows the form

$$V_{\mathrm{ext}}(y, t) = \mathrm{Re}\{V_0\cos(qy)\,\mathrm{e}^{-\mathrm{i}\omega t}\}. \tag{5.17}$$

Based on Eq. (5.8) the oscillating flow component is analysed in the limit of $\lambda_\mathrm{D}/d \ll 1$, and it is illustrated how this leads to an effective slip velocity on the bulk streaming of the form

$$\boldsymbol{v}_\mathrm{slip}^{2\omega} \propto \cos(2\omega t + \vartheta) \sin(2qy)\, \hat{\boldsymbol{e}}_y, \tag{5.18}$$

similar to the classical Rayleigh streaming, where ϑ describes a phase difference. Unfortunately, it is also mentioned that the steady streaming is found to be of much lower amplitude than the oscillating flow. The expression for the time-averaged streaming is not shown in the article, and it is only stated that a complicated expression was determined and plotted against numerical simulations.

This work inspired the derivation of a more general time-averaged slip velocity for the linearised problem discussed in the following, where the assumption $\lambda_\mathrm{D}/d \ll 1$ is used for otherwise arbitrary wall potentials. The effective boundary conditions will only be derived for flat walls, but they could likely also be stated in curvilinear coordinates. An example of how this might be done can be found in the recent work from Bach and Bruus [4], where a complete treatment of the acoustic slip velocity is done in curvilinear coordinates. In the final stages of the thesis work, it was discovered that the effective slip velocity developed in the following is analogue to an already known theory from the ICEO literature.

5.2.1 Effective electrostatic theory

We will analyse problems where the applied potential varies on length scales d much larger than the Debye length, such that $\lambda_\mathrm{D}/d \ll 1$. The applied potential is also harmonically oscillating at an angular frequency ω, so Eq. (5.14) and Eq. (5.15) will be our starting point. When writing ν or ϕ, it is thus the complex and spatially dependent phasors we refer to. Further, $\boldsymbol{v}$ and p will refer to the time-averaged fluid fields.

Consider a wall parallel to the y-direction with z going perpendicular to the wall. The ionic concentration decays so rapidly in the perpendicular direction that $\nabla^2 \approx \partial_z^2$ in Eq. (5.8a) yielding

$$-\mathrm{i}\omega\nu = D\partial_z^2\nu - \frac{D}{\lambda_\mathrm{D}^2}\nu. \tag{5.19}$$

The externally applied potential is written as $V_\mathrm{ext}(y) = V_0 w(y)$, where $w(y)$ is some slowly varying (compared to λ_D) complex function of y. With this, the approximate solution for the ionic concentration difference is

$$\nu(y,z) = Cw(y)\,\mathrm{e}^{-\kappa_\mathrm{el}z}, \qquad \kappa_\mathrm{el} = \frac{1}{\lambda_\mathrm{D}}\sqrt{1 - \mathrm{i}\frac{\omega}{\omega_\mathrm{D}}}, \qquad \omega_\mathrm{D} = \frac{D}{\lambda_\mathrm{D}^2}, \tag{5.20}$$

where C is a constant. The phasor for the electric potential is determined by

$$\nabla^2\phi = -\frac{Ze}{\epsilon_\mathrm{f}}Cw(y)\,\mathrm{e}^{-\kappa_\mathrm{el}z}. \tag{5.21}$$

The solution will be the sum of a particular solution confined to the boundary $\phi^{\lambda_\mathrm{D}}$ and a homogeneous solution extending into the bulk ϕ^b. We find an approximate expression for

the particular solution by imposing $\nabla^2 \phi^{\lambda_D} \approx \partial_z^2 \phi^{\lambda_D}$. With this,

$$\partial_z^2 \phi^{\lambda_D} = -\frac{Ze}{\epsilon_f} C w(y) \, e^{-\kappa_{el} z} \Rightarrow \tag{5.22}$$

$$\phi^{\lambda_D} = -\frac{Ze}{\epsilon_f \kappa_{el}^2} C w(y) \, e^{-\kappa_{el} z}. \tag{5.23}$$

The bulk potential ϕ^b is in turn determined by

$$\nabla^2 \phi^b = 0. \tag{5.24}$$

The boundary condition in Eq. (5.9) reads

$$0 = \partial_z \nu \big|_{z=0} + \frac{\epsilon_f}{Ze\lambda_D^2} \partial_z (\phi^{\lambda_D} + \phi^b) \big|_{z=0}, \tag{5.25}$$

from which we find

$$\partial_z \phi^b \big|_{z=0} = C w(y) \frac{-i\frac{\omega}{\omega_D}}{\kappa_{el}} \frac{Ze}{\epsilon_f}. \tag{5.26}$$

The applied potential dictates that

$$\phi(y, z=0) = V_0 w(y) = \phi^b(y, z=0) - \frac{Ze}{\epsilon_f \kappa_{el}^2} C w(y). \tag{5.27}$$

Eliminating C from Eq. (5.26) and Eq. (5.27), we find that

$$\phi^b(y, z=0) = V_0 w(y) + i\frac{\omega_D}{\omega} \frac{1}{\kappa_{el}} \partial_z \phi^b \big|_{z=0}. \tag{5.28}$$

Since the choice of wall-placement at $z = 0$ was rather arbitrary, we will generally formulate this as

$$\phi^b(\boldsymbol{s}_0) = V_0 w(\boldsymbol{s}_0) + i\frac{\omega_D}{\omega} \frac{1}{\kappa_{el}} \partial_\perp \phi^b(\boldsymbol{s}_0). \tag{5.29}$$

ω_D is related to the timescale of the Debye layer formation. Thus, it makes sense that the bulk potential is dominant for $\omega_D/\omega \ll 1$, because the Debye layer cannot form before the potential switches sign. In this case, the quasi-electrostatic problem is almost unaffected by the pressence of the ions. In a sense, the ions are too slow to react to the rapidly changing potential. For high frequencies where $\omega \sim \omega_D$, the correction to the boundary condition on the electric bulk potential becomes very small

$$\left| i\frac{\omega_D}{\omega} \frac{1}{\kappa_{el}} \partial_\perp \phi^b(\boldsymbol{s}_0) \right| \sim (\lambda_D/d) \phi^b(\boldsymbol{s}_0). \tag{5.30}$$

The amplitude of this correction is then comparable to terms which were discarded in the derivation of the boundary condition. In this regime, we cannot expect the effective theory to hold, although the qualitative behaviour appears to be right. Thus, we will always assume $\omega \ll \omega_D$, which turns out to be the more relevant frequency regime regardless. For

Table 5.1: Parameters used for the initial test of effective ICEO boundary conditions.

$\lambda_{\mathrm{D}} = (\epsilon_{\mathrm{f}} k_{\mathrm{B}} T / 2(Ze)^2 c_0)^{1/2}$	$9.7\,\mathrm{nm}$	D	$10^{-9}\,\mathrm{m^2/s}$
$\omega_{\mathrm{D}} = D/\lambda_{\mathrm{D}}^2$	$10.6 \times 10^6\,\mathrm{rad/s}$	$\omega = 5 \times 10^{-4} \omega_{\mathrm{D}}$	$5.3 \times 10^3\,\mathrm{rad/s}$
V_0	$1\,\mathrm{mV}$	$H_{\mathrm{ch}} \times W_{\mathrm{ch}}$	$80\,\mathrm{\mu m} \times 100\,\mathrm{\mu m}$

lower frequencies where $\omega_{\mathrm{D}}/\omega \gg 1$, the Debye layer heavily influences the problem with a divergence for $\omega \to 0$, where no bulk potential will exist at all due to complete screening.

After calculating ϕ^{b}, we can find the constant C, and with this ν and $\phi^{\lambda_{\mathrm{D}}}$ readily follows. From Eq. (5.26) we have

$$Cw(\boldsymbol{s}_0) = \mathrm{i}\frac{\omega_{\mathrm{D}}}{\omega} \frac{\epsilon_{\mathrm{f}} \kappa_{\mathrm{el}}}{Ze} \partial_\perp \phi^{\mathrm{b}}(\boldsymbol{s}_0). \tag{5.31}$$

We still denote the direction perpendicular to (and the distance from) the boundary by a capital Z. With this, we write

$$\nu = \mathrm{i}\frac{\omega_{\mathrm{D}}}{\omega} \frac{\epsilon_{\mathrm{f}} \kappa_{\mathrm{el}}}{Ze} \partial_\perp \phi^{\mathrm{b}}(\boldsymbol{s}_0)\, \mathrm{e}^{-\kappa_{\mathrm{el}} Z}, \tag{5.32a}$$

$$\phi^{\lambda_{\mathrm{D}}} = -\mathrm{i}\frac{\omega_{\mathrm{D}}}{\omega} \frac{1}{\kappa_{\mathrm{el}}} \partial_\perp \phi^{\mathrm{b}}(\boldsymbol{s}_0)\, \mathrm{e}^{-\kappa_{\mathrm{el}} Z}. \tag{5.32b}$$

Like the previous effective boundary layer theories, this circumvents the need of resolving the very thin boundary layer numerically, since the rapidly decaying fields are found analytically.

5.2.2 Numerical validation of the effective electrostatic theory

The precision of the effective quasi-electrostatic theory is illustrated with an example. The electrostatic fields are calculated from both the effective and the full theory. A rectangular geometry of dimensions $H_{\mathrm{ch}} \times W_{\mathrm{ch}} = 80\,\mathrm{\mu m} \times 100\,\mathrm{\mu m}$ is used. An external potential is implemented with a somewhat random shape to test the theory with both phase differences and surface gradients. The external potential on the walls is given by

$$\phi\big(y, z = \pm\frac{H_{\mathrm{ch}}}{2}\big) = \mp V_0 \mathrm{e}^{\mathrm{i}\pi/3}, \quad \phi\big(y = -\frac{W_{\mathrm{ch}}}{2}, z\big) = V_0 \sin\big(\frac{y}{W_{\mathrm{ch}}}\big), \quad \phi\big(y = \frac{W_{\mathrm{ch}}}{2}, z\big) = -V_0. \tag{5.33}$$

The linearised Nernst–Planck equation for the full theory is implemented on its conventional conservation form

$$\boldsymbol{\nabla} \cdot \left(D\boldsymbol{\nabla}\nu + \frac{\epsilon_{\mathrm{f}} D}{Ze\lambda_{\mathrm{D}}^2} \boldsymbol{\nabla}\phi \right) + \mathrm{i}\omega\nu = 0, \tag{5.34}$$

because COMSOL handles this better.

Only the water with dissolved ions is simulated. The geometry alongside the applied equations and boundary conditions are illustrated in figure 5.1, and simulation parameters are stated in table 5.1.
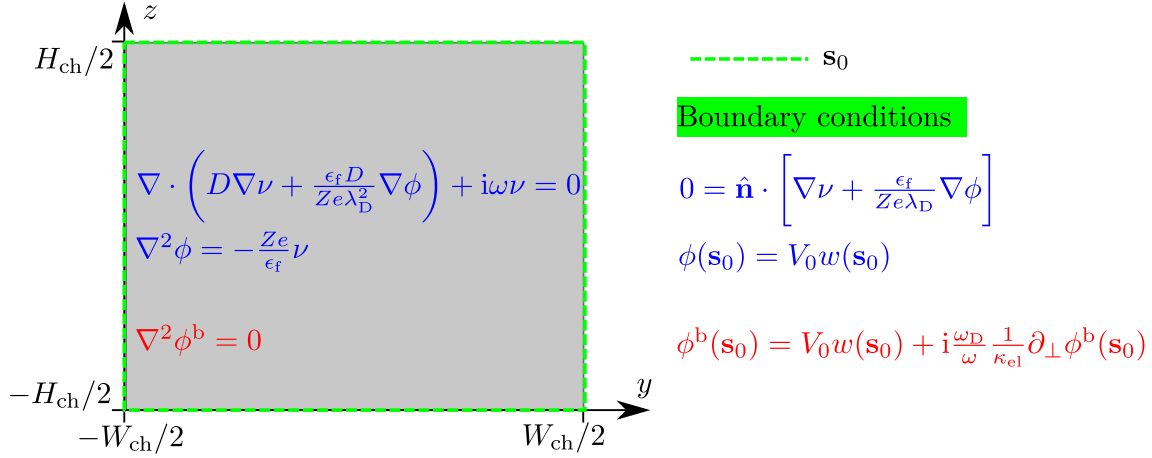
Figure 5.1: Geometry for effective ICEO boundary condition test. The applied equations and boundary conditions are stated. The full theory is written in blue, and the effective theory is the red equations.

The result of the simulation is shown in figure 5.2, where the applied finite element meshes are illustrated as well. While the required bulk meshes are similar for the full and the effective theory, the required boundary resolving differs significantly. For the full model, enough boundary layers are added to resolve the entire Debye layer. For the effective model, only a single boundary layer is added, which serves to enhance the precision of normal derivatives.

We notice that the full model and the effective model are very similar in the bulk of the fluid as expected. The effective model varies very little in the thin boundary layer, while the full model undergoes a rapid exponential change. This exponential change can be replicated by adding Eq. (5.32b) to the plot as shown in figure 5.2 (f). It is the knowledge of this exponential shape that allows us to derive an effective boundary condition on the fluid velocity $\boldsymbol{v}$ in the following.

The boundary conditions on the potential in Eq. (5.33) are actually inconsistent at the corners, which caused numerical defects for the full model. However, as long as a refinement of the corners of the finite element mesh was done, the errors were localised at the corners within a length scale of less than a micrometer. Inconsistent boundary conditions will also be chosen in an analysis that follows, and because of the very localised nature of the defects that this causes, we will not worry too much about the corners. Of course, the inconsistent boundary conditions are in a sense nonphysical but so is a perfectly sharp corner. We keep in mind that the inconsistencies in boundary conditions could be resolved locally at the corners with interpolation functions and rounded corners to make the potential continuous. This can be done in a way that keeps the same general shape of the physical fields in the fluid chamber. An example of this is in given when a full non-linear and time-dependent study is performed in the end of this chapter. For time-dependent calculations, numerical defects tend to propagate and increase in time, and the corners will thus be reassessed.
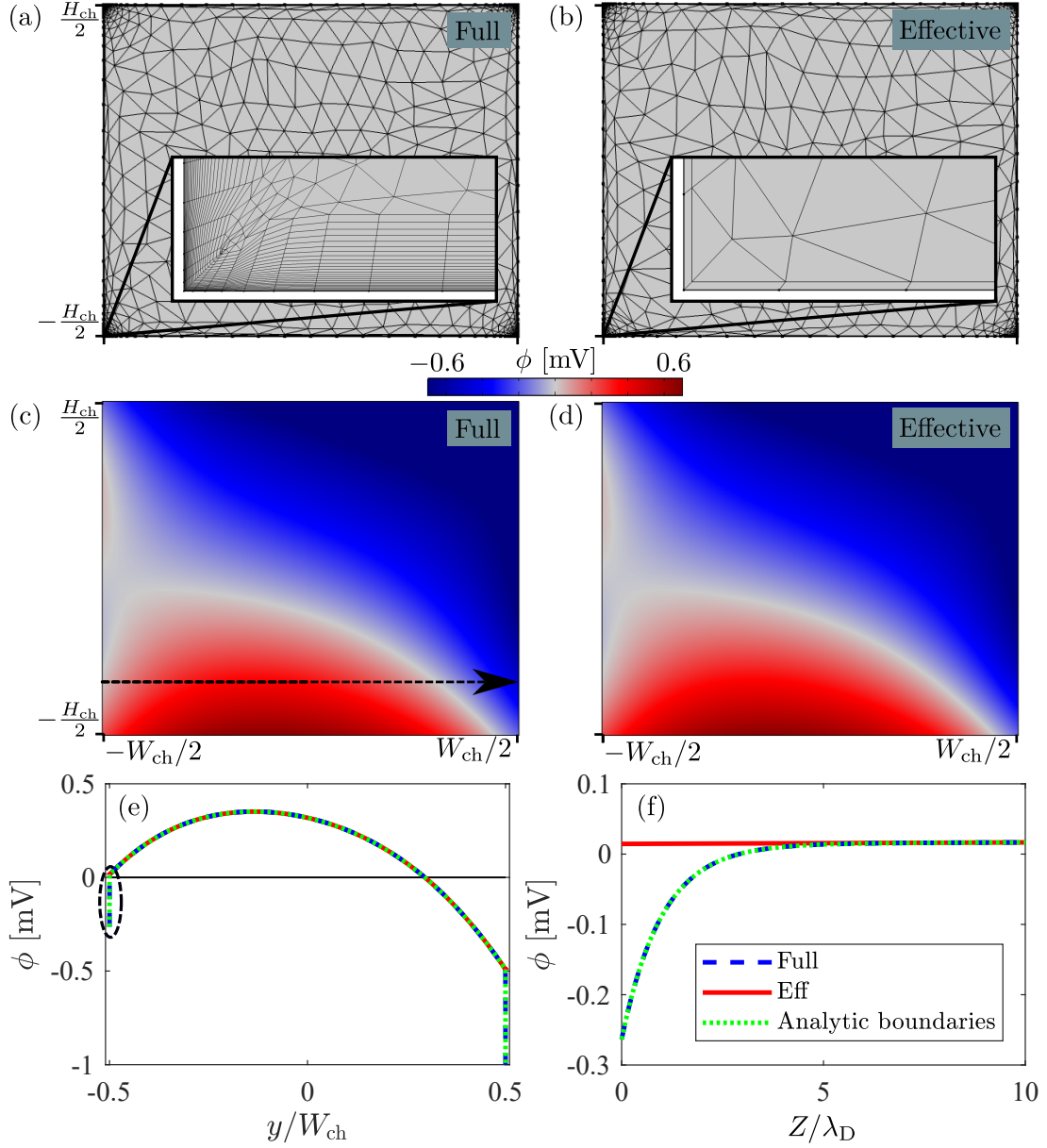
Figure 5.2: Result of the effective quasi-electrostatic boundary condition test for ICEO. (a) full model finite element mesh with the fully resolved Debye layer. (b) effective model mesh with a single boundary layer for normal derivative precision. (c) ϕ calculated with the full model. (d) ϕ^{b} calculated from the effective model. (e) ϕ and ϕ^{b} calculated with the full and the effective model, respectively, plotted along the black dashed arrow in (c). The effective solution with $\phi^{\lambda_{\mathrm{D}}}$ added from Eq. (5.32b) is plotted on top. (f) the fields shown close to the boundary (incircled in (e)).

5.2.3   Effective slip velocity

Since we can calculate the charge density $Ze\nu$ and the potential ϕ by only referencing to the bulk potential ϕ^{b}, we can also determine the electric body force from ϕ^{b}. Again, we consider a solid wall parallel to the y-axis at $z = 0$ with z extending perpendicularly into the fluid. The time-averaged electric body force $\langle \boldsymbol{f}_{\mathrm{b}} \rangle$ is split into a parallel y-component and a perpendicular z-component. We determine the time-averaged electric body force from

$$\langle \boldsymbol{f}_{\mathrm{b}} \rangle = -\frac{Ze}{2}\mathrm{Re}\big\{\nu\boldsymbol{\nabla}(\phi^{\mathrm{b}} + \phi^{\lambda_{\mathrm{D}}})^{*}\big\}. \tag{5.35}$$

Since the bulk potential ϕ^{b} varies on the length scale d, and ν decays perpendicular to the boundary on the length scale of λ_{D}, we can assume that $\boldsymbol{\nabla}\phi^{\mathrm{b}}$ varies very little in the perpendicular direction before $\nu\boldsymbol{\nabla}\phi^{\mathrm{b}*}$ decays close to zero. Therefore, we make the approximation

$$\nu(y, z)\boldsymbol{\nabla}\phi^{\mathrm{b}*}(y, z) \approx \nu(y, z)\boldsymbol{\nabla}\phi^{\mathrm{b}*}(\boldsymbol{s}_0). \tag{5.36}$$

With this, we find the following components for the electric body force

$$\begin{aligned}
\langle f_{\mathrm{b}y} \rangle = -&\frac{\epsilon_{\mathrm{f}}}{2}\mathrm{Re}\bigg\{\mathrm{i}\frac{\omega_{\mathrm{D}}}{\omega}\kappa_{\mathrm{el}}\partial_z\phi^{\mathrm{b}}(\boldsymbol{s}_0)\partial_y\phi^{\mathrm{b}*}(\boldsymbol{s}_0)\mathrm{e}^{-\kappa_{\mathrm{el}}z}\bigg\} \\
+&\frac{\epsilon_{\mathrm{f}}}{2}\mathrm{Re}\bigg\{\Big(\frac{\omega_{\mathrm{D}}}{\omega}\Big)^2\frac{\kappa_{\mathrm{el}}}{\kappa_{\mathrm{el}}^*}\partial_z\phi^{\mathrm{b}}(\boldsymbol{s}_0)\partial_y\partial_z\phi^{\mathrm{b}*}(\boldsymbol{s}_0)\mathrm{e}^{-2\mathrm{Re}\{\kappa_{\mathrm{el}}\}z}\bigg\},
\end{aligned} \tag{5.37a}$$

$$\begin{aligned}
\langle f_{\mathrm{b}z} \rangle = -&\frac{\epsilon_{\mathrm{f}}}{2}\mathrm{Re}\bigg\{\mathrm{i}\frac{\omega_{\mathrm{D}}}{\omega}\kappa_{\mathrm{el}}|\partial_z\phi^{\mathrm{b}}(\boldsymbol{s}_0)|^2\mathrm{e}^{-\kappa_{\mathrm{el}}z}\bigg\} \\
+&\frac{\epsilon_{\mathrm{f}}}{2}\mathrm{Re}\bigg\{\Big(\frac{\omega_{\mathrm{D}}}{\omega}\Big)^2\kappa_{\mathrm{el}}|\partial_z\phi^{\mathrm{b}}(\boldsymbol{s}_0)|^2\mathrm{e}^{-2\mathrm{Re}\{\kappa_{\mathrm{el}}\}z}\bigg\}.
\end{aligned} \tag{5.37b}$$

The steady flow $\boldsymbol{v} = \boldsymbol{v}(\boldsymbol{r})$ and pressure $p = p(\boldsymbol{r})$ are then determined from

$$0 = \boldsymbol{\nabla}\cdot\boldsymbol{v}, \tag{5.38a}$$

$$\boldsymbol{0} = \eta\nabla^2\boldsymbol{v} - \boldsymbol{\nabla}p + \langle\boldsymbol{f}_{\mathrm{b}}\rangle, \tag{5.38b}$$

$$\boldsymbol{v}(\boldsymbol{s}_0) = \boldsymbol{0}. \tag{5.38c}$$

We consider the fluid in a thin layer above the boundary $0 \leq z \lesssim 5\lambda_{\mathrm{D}}$. Here, the electric body force is present to drive the flow. The flow abruptly comes to a stop on the wall and grows to a value comparable to the bulk streaming at the end of this layer. The variation parallel to the boundary is always comparable to the variations in the bulk. Eq. (5.38a) then refinds the relation stated in Eq. (2.47), where $v_z \ll v_y$. We will assume that the normal component of the velocity field in the boundary layer is small enough that the normal component of Eq. (5.38b) becomes

$$\partial_z p = \langle f_{\mathrm{b}z} \rangle. \tag{5.39}$$

Integrating this, we find the following form of the pressure

$$
\begin{aligned}
p = & -\frac{\epsilon_{\mathrm{f}}}{2}\mathrm{Re}\left\{\mathrm{i}\frac{\omega_{\mathrm{D}}}{\omega}|\partial_z\phi^{\mathrm{b}}(\boldsymbol{s}_0)|^2\mathrm{e}^{-\kappa_{\mathrm{el}}z}\right\} \\
& +\frac{\epsilon_{\mathrm{f}}}{2}\mathrm{Re}\left\{\left(\frac{\omega_{\mathrm{D}}}{\omega}\right)^2\frac{\kappa_{\mathrm{el}}}{2\mathrm{Re}\{\kappa_{\mathrm{el}}\}}|\partial_z\phi^{\mathrm{b}}(\boldsymbol{s}_0)|^2\mathrm{e}^{-2\mathrm{Re}\{\kappa_{\mathrm{el}}\}z}\right\}.
\end{aligned}
\tag{5.40}
$$

Taking the divergence of Eq. (5.38b) and using Eq. (5.38a), we find that

$$
\nabla^2 p - \boldsymbol{\nabla}\cdot\langle\boldsymbol{f}_b\rangle = 0.
\tag{5.41}
$$

With the choice of p in Eq. (5.40), it is found that this is fulfilled to first order in λ_{D}/d

$$
\nabla^2 p - \boldsymbol{\nabla}\cdot\langle\boldsymbol{f}_b\rangle = \mathcal{O}([\lambda_{\mathrm{D}}/d]).
\tag{5.42}
$$

The parallel flow component v_y is determined from

$$
\eta\nabla^2 v_y \approx \eta\partial_z^2 v_y = \partial_y p - \langle f_{\mathrm{b}y}\rangle.
\tag{5.43}
$$

Eq. (5.37a) and Eq. (5.40) are inserted into this, yielding an expression which depends analytically on z through simple exponential functions. The expression is integrated twice, and the no-slip boundary condition is imposed to reach

$$
\begin{aligned}
v_y = & -\frac{\epsilon_{\mathrm{f}}}{\eta}\mathrm{Re}\{\partial_y\partial_z\phi^{\mathrm{b}}(\boldsymbol{s}_0)\partial_z\phi^{\mathrm{b}*}(\boldsymbol{s}_0)\}\mathrm{Re}\left\{\left[1-\mathrm{e}^{-2\mathrm{Re}\{\kappa_{\mathrm{el}}\}z}\right]\left(\frac{\omega_{\mathrm{D}}}{\omega}\right)^2\frac{\kappa_{\mathrm{el}}}{(2\mathrm{Re}\{\kappa_{\mathrm{el}}\})^3}\right\} \\
& +\frac{\epsilon_{\mathrm{f}}}{\eta}\mathrm{Re}\{\partial_y\partial_z\phi^{\mathrm{b}}(\boldsymbol{s}_0)\partial_z\phi^{\mathrm{b}*}(\boldsymbol{s}_0)\}\mathrm{Re}\left\{\left[1-\mathrm{e}^{-\kappa_{\mathrm{el}}z}\right]\left(\frac{\omega_{\mathrm{D}}}{\omega}\right)\frac{\mathrm{i}}{\kappa_{\mathrm{el}}^2}\right\} \\
& +\frac{\epsilon_{\mathrm{f}}}{2\eta}\mathrm{Re}\left\{\left[1-\mathrm{e}^{-2\mathrm{Re}\{\kappa_{\mathrm{el}}\}z}\right]\left(\frac{\omega_{\mathrm{D}}}{\omega}\right)^2\frac{\kappa_{\mathrm{el}}}{\kappa_{\mathrm{el}}^*(2\mathrm{Re}\{\kappa_{\mathrm{el}}\})^2}\partial_z\phi^{\mathrm{b}}(\boldsymbol{s}_0)\partial_y\partial_z\phi^{\mathrm{b}*}(\boldsymbol{s}_0)\right\} \\
& -\frac{\epsilon_{\mathrm{f}}}{2\eta}\mathrm{Re}\left\{\left[1-\mathrm{e}^{-\kappa_{\mathrm{el}}z}\right]\left(\frac{\omega_{\mathrm{D}}}{\omega}\right)\frac{\mathrm{i}}{\kappa_{\mathrm{el}}}\partial_z\phi^{\mathrm{b}}(\boldsymbol{s}_0)\partial_y\phi^{\mathrm{b}*}(\boldsymbol{s}_0)\right\}.
\end{aligned}
\tag{5.44}
$$

In the bulk of the fluid $z \gtrsim 5\lambda_{\mathrm{D}}$, the electric body force has decayed to essentially zero. At the same time, the velocity field in Eq. (5.44) has underwent a rapid increase, as the exponential functions have decayed. The bulk velocity does not vary significantly on the length scale of the boundary layer, and the rapid growth of the velocity field in the boundary layer almost happens right on the boundary, when seen from the bulk. The velocity field is continuous, so the velocity in Eq. (5.44) for $z \to \infty$ can approximately constitute the velocity of the bulk fluid on the solid boundaries. The choice of coordinates was again arbitrary, and the flow in the bulk of the fluid is determined by

$$
0 = \boldsymbol{\nabla}\cdot\boldsymbol{v},
\tag{5.45a}
$$

$$
\boldsymbol{0} = \eta\nabla^2\boldsymbol{v} - \boldsymbol{\nabla}p,
\tag{5.45b}
$$

$$
\boldsymbol{v}(\boldsymbol{s}_0) = \boldsymbol{v}_{\mathrm{slip}}^{\mathrm{ICEO}},
\tag{5.45c}
$$

where the ICEO slip velocity is given by

$$
\begin{aligned}
\boldsymbol{v}_{\text{slip}}^{\text{ICEO}} = \hat{\boldsymbol{e}}_{\parallel} &\left[\frac{\epsilon_{\text{f}}}{\eta} \text{Re}\{\partial_{\parallel}\partial_{\perp}\phi^{\text{b}}(\boldsymbol{s}_0)\partial_{\perp}\phi^{\text{b}*}(\boldsymbol{s}_0)\}\text{Re}\left\{ \left(\frac{\omega_{\text{D}}}{\omega}\right)\frac{\text{i}}{\kappa_{\text{el}}^2} - \left(\frac{\omega_{\text{D}}}{\omega}\right)^2 \frac{\kappa_{\text{el}}}{(2\text{Re}\{\kappa_{\text{el}}\})^3} \right\} \right. \\
&+ \frac{\epsilon_{\text{f}}}{2\eta}\text{Re}\left\{ \left(\frac{\omega_{\text{D}}}{\omega}\right)^2 \frac{\kappa_{\text{el}}}{\kappa_{\text{el}}^*(2\text{Re}\{\kappa_{\text{el}}\})^2}\partial_{\perp}\phi^{\text{b}}(\boldsymbol{s}_0)\partial_{\parallel}\partial_{\perp}\phi^{\text{b}*}(\boldsymbol{s}_0) \right\} \\
&\left. - \frac{\epsilon_{\text{f}}}{2\eta}\text{Re}\left\{ \left(\frac{\omega_{\text{D}}}{\omega}\right)\frac{\text{i}}{\kappa_{\text{el}}}\partial_{\perp}\phi^{\text{b}}(\boldsymbol{s}_0)\partial_{\parallel}\phi^{\text{b}*}(\boldsymbol{s}_0) \right\} \right].
\end{aligned}
\tag{5.46}
$$

Hence, we only need to calculate the electric potential in the bulk to determine the flow in the bulk of the chamber.

5.2.4 Numerical validation of the effective slip velocity

The simulation shown in subsection 5.2.2 is extended to calculate the flow as well. The parameters and meshing remain the same, so the electric field illustrated in 5.2 is used to calculate the streaming. The time-averaged streaming is calculated with the effective model in Eq. (5.45) and Eq. (5.46) as well as with the full model in Eq. (5.15) and the no-slip condition.

The results of the simulation are shown in figure 5.3. Line plots of the velocity field is plotted in the bulk and at the boundary of the fluid. It is also illustrated how well we can determine the pressure and body force at the boundaries. Again, a very strong agreement is seen between the effective and the full simulation. The Debye layer velocity field calculated in Eq. (5.44) is plotted near the boundary on top of the effective and the full calculation of the velocity field. We notice how it follows the full calculation until around $Z \approx 5\lambda_{\text{D}}$, after which it reaches a constant value equal to the initial value of the effective model. This offset on the slip velocity in the effective model makes it fall straight onto the full calculation outside of the Debye layer $Z \gtrsim 5\lambda_{\text{D}}$.

The total solving time for the given simulation is around 6 seconds for the effective theory and 30 seconds for the full theory. For 3D simulations, the discrepancy would be much larger. For full system 3D simulations, an effective boundary layer theory may even act as enabling rather than just an improvement in computational footprint, as was the case for the effective acoustic streaming theory.
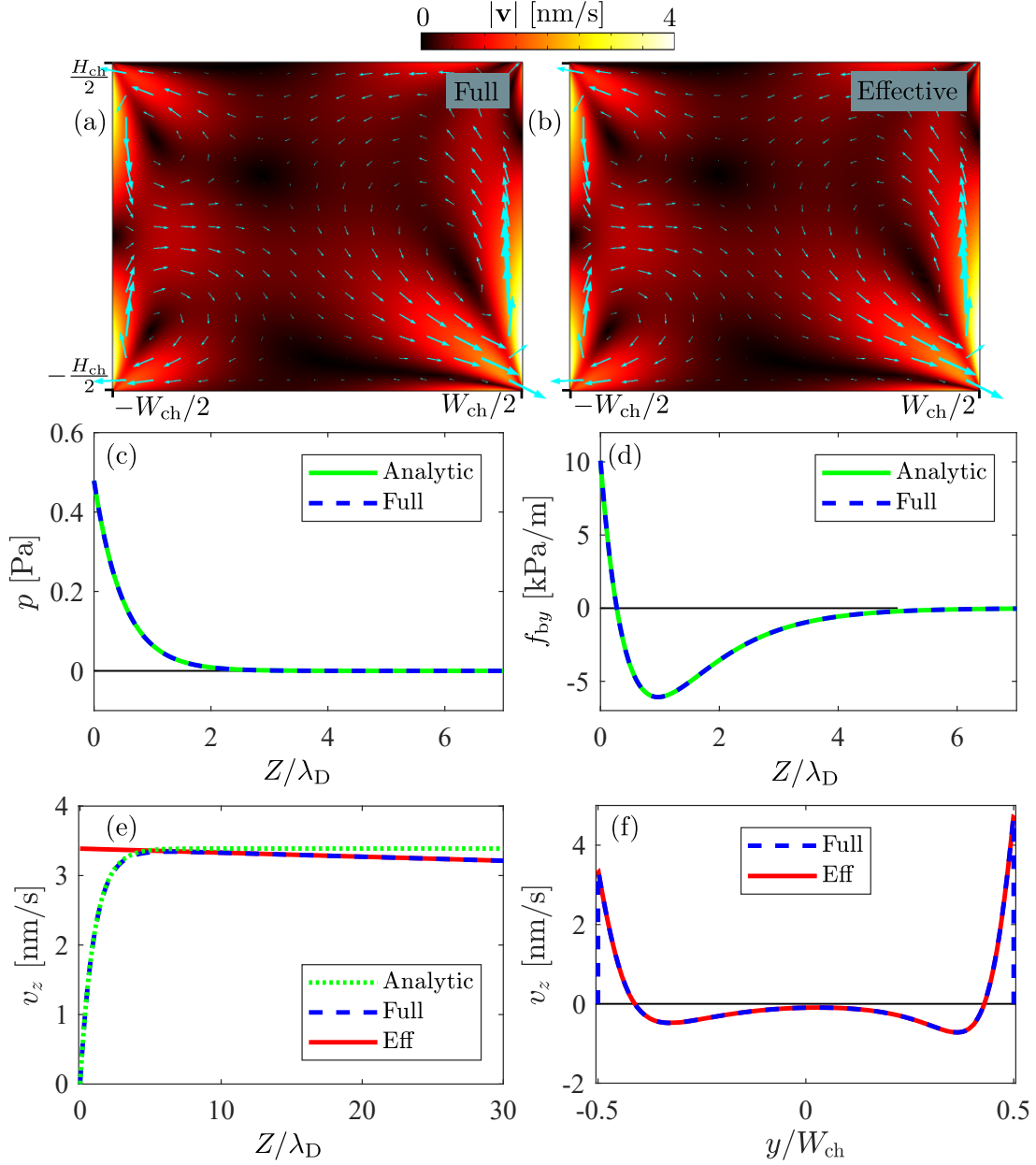
Figure 5.3: Result of the effective slip velocity test for ICEO. (a) field plot of the velocity field calculated from the full model. (b) effective model velocity field. (c)-(f) are plotted along the black dashed arrow in figure 5.2 (c). (c)-(e) are plotted only in the thin Debye layer. (c) pressure calculated with the full model plotted against the analytical expression. (d) the parallel body force component f_{by} plotted for the full calculation against the analytical expression. (e) v_z plotted for the full and the effective model. On top is shown the analytical expression for v_z in the thin boundary layer, which is seen to reach a constant level around $Z \approx 5\lambda_D$. (f) v_z calculated with the full and the effective model.

5.2.5   Simplified slip velocity

We have now derived and numerically confirmed an effective boundary layer theory for the time-averaged ICEO streaming. However, the relative importance of the separate terms were not evaluated. We will state the slip velocity as the sum of the following three terms

$$
\begin{aligned}
\boldsymbol{v}_{\text{slip}}^{\text{ICEO}} = \hat{\boldsymbol{e}}_{\parallel} \bigg[& \frac{\epsilon_{\text{f}}}{\eta} \left(\frac{\omega_{\text{D}}}{\omega} \right) \text{Re}\{\partial_{\parallel}\partial_{\perp}\phi^{\text{b}}(\boldsymbol{s}_0)\partial_{\perp}\phi^{\text{b}*}(\boldsymbol{s}_0)\} \text{Re}\left\{ \frac{\text{i}}{\kappa_{\text{el}}^2} \right\} \\
& + \frac{\epsilon_{\text{f}}}{2\eta} \left(\frac{\omega_{\text{D}}}{\omega} \right)^2 \text{Re}\left\{ \frac{\kappa_{\text{el}}}{(2\text{Re}\{\kappa_{\text{el}}\})^2} \left(\frac{\partial_{\perp}\phi^{\text{b}}(\boldsymbol{s}_0)\partial_{\parallel}\partial_{\perp}\phi^{\text{b}*}(\boldsymbol{s}_0)}{\kappa_{\text{el}}^*} - \frac{\text{Re}\{\partial_{\perp}\phi^{\text{b}}(\boldsymbol{s}_0)\partial_{\parallel}\partial_{\perp}\phi^{\text{b}*}(\boldsymbol{s}_0)\}}{\text{Re}\{\kappa_{\text{el}}^*\}} \right) \right\} \\
& - \frac{\epsilon_{\text{f}}}{2\eta} \text{Re}\left\{ \left(\frac{\omega_{\text{D}}}{\omega} \right) \frac{\text{i}}{\kappa_{\text{el}}} \partial_{\perp}\phi^{\text{b}}(\boldsymbol{s}_0)\partial_{\parallel}\phi^{\text{b}*}(\boldsymbol{s}_0) \right\} \bigg].
\end{aligned}
$$

$$(5.47)$$

For the first term, inserting $\kappa_{\text{el}} = \sqrt{1 - \text{i}\omega/\omega_{\text{D}}}/\lambda_{\text{D}}$ yields

$$
\frac{\epsilon_{\text{f}}}{\eta} \left(\frac{\omega_{\text{D}}}{\omega} \right) \text{Re}\{\partial_{\parallel}\partial_{\perp}\phi^{\text{b}}(\boldsymbol{s}_0)\partial_{\perp}\phi^{\text{b}*}(\boldsymbol{s}_0)\} \text{Re}\left\{ \frac{\text{i}}{\kappa_{\text{el}}^2} \right\} = \frac{\epsilon_{\text{f}}}{\eta} \frac{2\lambda_{\text{D}}^2}{1 + (\frac{\omega}{\omega_{\text{D}}})^2} \text{Re}\{\partial_{\parallel}\partial_{\perp}\phi^{\text{b}}(\boldsymbol{s}_0)\partial_{\perp}\phi^{\text{b}*}(\boldsymbol{s}_0)\}.
$$

$$(5.48)$$

To evaluate the second term, we use that two complex numbers $z_1 = a_1 + \text{i}b_1$ and $z_2 = a_2 + \text{i}b_2$ satisfy

$$
\frac{z_1}{z_2} - \frac{\text{Re}z_1}{\text{Re}z_2} = \frac{b_2(a_2b_1 - a_1b_2) + \text{i}(b_1a_2^2 - a_1b_2a_2)}{a_2(a_2^2 + b_2^2)}.
$$

$$(5.49)$$

Inserting

$$
\begin{aligned}
a_1 &= \text{Re}\{\partial_{\perp}\phi^{\text{b}}(\boldsymbol{s}_0)\partial_{\parallel}\partial_{\perp}\phi^{\text{b}*}(\boldsymbol{s}_0)\}, \\
b_1 &= \text{Im}\{\partial_{\perp}\phi^{\text{b}}(\boldsymbol{s}_0)\partial_{\parallel}\partial_{\perp}\phi^{\text{b}*}(\boldsymbol{s}_0)\}, \\
a_2 &= \text{Re}\{\kappa_{\text{el}}^*\} = \frac{\sqrt{(1 + \omega^2/\omega_{\text{D}}^2)^{1/2} + 1}}{\sqrt{2}\lambda_{\text{D}}} \approx \frac{1}{\lambda_{\text{D}}}, \\
b_2 &= \text{Im}\{\kappa_{\text{el}}^*\} = \frac{\sqrt{(1 + \omega^2/\omega_{\text{D}}^2)^{1/2} - 1}}{\sqrt{2}\lambda_{\text{D}}} \approx \frac{1}{2\lambda_{\text{D}}} \frac{\omega}{\omega_{\text{D}}},
\end{aligned}
$$

$$(5.50)$$

it is found that

$$
\begin{aligned}
& \frac{\epsilon_{\text{f}}}{2\eta} \left(\frac{\omega_{\text{D}}}{\omega} \right)^2 \text{Re}\left\{ \frac{\kappa_{\text{el}}}{(2\text{Re}\{\kappa_{\text{el}}\})^2} \left(\frac{\partial_{\perp}\phi^{\text{b}}(\boldsymbol{s}_0)\partial_{\parallel}\partial_{\perp}\phi^{\text{b}*}(\boldsymbol{s}_0)}{\kappa_{\text{el}}^*} - \frac{\text{Re}\{\partial_{\perp}\phi^{\text{b}}(\boldsymbol{s}_0)\partial_{\parallel}\partial_{\perp}\phi^{\text{b}*}(\boldsymbol{s}_0)\}}{\text{Re}\{\kappa_{\text{el}}^*\}} \right) \right\} = \\
& \frac{\epsilon_{\text{f}}}{2\eta} \left(\frac{\omega_{\text{D}}}{\omega} \right)^2 \frac{b_2}{2a_2^2(a_2^2 + b_2^2)} (a_2b_1 - a_1b_2).
\end{aligned}
$$

$$(5.51)$$

Since we are considering $\omega \ll \omega_D$, this is expanded to lowest order in ω/ω_D to find

$$
\frac{\epsilon_f}{2\eta}\left(\frac{\omega_D}{\omega}\right)^2 \text{Re}\left\{\frac{\kappa_{el}}{(2\text{Re}\{\kappa_{el}\})^2}\left(\frac{\partial_\perp \phi^b(\boldsymbol{s}_0)\partial_\parallel\partial_\perp\phi^{b*}(\boldsymbol{s}_0)}{\kappa_{el}^*} - \frac{\text{Re}\{\partial_\perp\phi^b(\boldsymbol{s}_0)\partial_\parallel\partial_\perp\phi^{b*}(\boldsymbol{s}_0)\}}{\text{Re}\{\kappa_{el}^*\}}\right)\right\} \approx
$$
$$
\frac{\epsilon_f}{8\eta}\lambda_D^2\left[\left(\frac{\omega_D}{\omega}\right)\text{Im}\{\partial_\perp\phi^b(\boldsymbol{s}_0)\partial_\parallel\partial_\perp\phi^{b*}(\boldsymbol{s}_0)\} - \frac{1}{2}\text{Re}\{\partial_\perp\phi^b(\boldsymbol{s}_0)\partial_\parallel\partial_\perp\phi^{b*}(\boldsymbol{s}_0)\}\right].
\tag{5.52}
$$

The third term to lowest order in ω/ω_D is found to be

$$
-\frac{\epsilon_f}{2\eta}\text{Re}\left\{\left(\frac{\omega_D}{\omega}\right)\frac{i}{\kappa_{el}}\partial_\perp\phi^b(\boldsymbol{s}_0)\partial_\parallel\phi^{b*}(\boldsymbol{s}_0)\right\} \approx
$$
$$
\frac{\epsilon_f}{2\eta}\lambda_D\left[\left(\frac{\omega_D}{\omega}\right)\text{Im}\{\partial_\perp\phi^b(\boldsymbol{s}_0)\partial_\parallel\phi^{b*}(\boldsymbol{s}_0)\} + \frac{1}{2}\text{Re}\{\partial_\perp\phi^b(\boldsymbol{s}_0)\partial_\parallel\phi^{b*}(\boldsymbol{s}_0)\}\right].
\tag{5.53}
$$

Since $\partial_\perp\phi^b \sim \partial_\parallel\phi^b \sim \phi^b/d$, the last term is found to be an order of d/λ_D larger than the two other terms. To lowest order in λ_D/d, we thus find

$$
\boldsymbol{v}_{slip}^{ICEO} \approx -\hat{\boldsymbol{e}}_\parallel\frac{\epsilon_f\lambda_D}{2\eta}\text{Re}\left\{\left(\frac{\omega_D}{\omega}\right)\frac{i}{\kappa_{el}}\partial_\perp\phi^b(\boldsymbol{s}_0)\partial_\parallel\phi^{b*}(\boldsymbol{s}_0)\right\}
$$
$$
\approx \hat{\boldsymbol{e}}_\parallel\frac{\epsilon_f\lambda_D}{2\eta}\left[\left(\frac{\omega_D}{\omega}\right)\text{Im}\{\partial_\perp\phi^b(\boldsymbol{s}_0)\partial_\parallel\phi^{b*}(\boldsymbol{s}_0)\} + \frac{1}{2}\text{Re}\{\partial_\perp\phi^b(\boldsymbol{s}_0)\partial_\parallel\phi^{b*}(\boldsymbol{s}_0)\}\right].
\tag{5.54}
$$

The dominant term originally came from the parallel derivative in the electric bulk potential acting on the electric charge density. We notice that the imaginary part of $\partial_\perp\phi^b(\boldsymbol{s}_0)\partial_\parallel\phi^{b*}(\boldsymbol{s}_0)$ is multiplied by a factor of ω_D/ω as compared to the real part. Since $\omega \ll \omega_D$ the streaming is dramatically increased if this product has an imaginary part. As mentioned previously, [36] studies a simple spatially and timely harmonic electric potential at the fluid/solid boundary. A single harmonic mode like that cannot have an imaginary part in $\partial_\perp\phi^b(\boldsymbol{s}_0)\partial_\parallel\phi^{b*}(\boldsymbol{s}_0)$, leading to the reported smallness in the time-averaged streaming. This is illustrated in the following, alongside a theoretically simple way of "fixing" this apparent problem of the low streaming amplitude.

Lastly, we write the slip velocity on another form. From Eq. (5.32a) we find the complex amplitude of the charge per surface area $\sigma_{el}(\boldsymbol{r})$ that accumulates in the thin Debye layer.

$$
\sigma_{el}(\boldsymbol{r}) = \int_0^\infty Ze\nu(\boldsymbol{r})\,dZ = i\frac{\omega_D}{\omega}\epsilon_f\partial_\perp\phi^b(\boldsymbol{s}_0).
\tag{5.55}
$$

Defining the electric bulk field tangential to the boundary by $E_\parallel^b(\boldsymbol{s}_0) = -\partial_\parallel\phi^b(\boldsymbol{s}_0)$, the slip velocity in Eq. (5.54) can for $\omega \ll \omega_D$ be written as

$$
\boldsymbol{v}_{slip}^{ICEO} = \hat{\boldsymbol{e}}_\parallel\frac{1}{2\eta}\text{Re}\left\{\frac{1}{\kappa_{el}}\sigma_{el}(\boldsymbol{s}_0)E_\parallel^{b*}(\boldsymbol{s}_0)\right\}
$$
$$
\approx \hat{\boldsymbol{e}}_\parallel\frac{\lambda_D}{\eta}\langle\tilde{\sigma}_{el}(\boldsymbol{s}_0,t)\tilde{E}_\parallel^b(\boldsymbol{s}_0,t)\rangle,
\tag{5.56}
$$

where the notation from Eq. (2.5) has been used. This form is also stated in the early work of Ajdari from 2000 [8] with no derivation.

5.3   Examples of linearised induced charge electroosmosis

We proceed the project by studying some examples of ICEO. We seek intuition about the shape and amplitude of the AC induced steady flow for a given set of boundary conditions for the potential. The effective electrostatic theory and the reduced expression for the slip velocity are used to perform a series of analytical calculations that are compared to numerical simulations. These examples are used for a physical discussion that elaborates on the nature of the streaming induced by ICEO.

5.3.1   Single mode

Yet again, we consider a rectangular fluid channel of dimensions $H_{\text{ch}} \times W_{\text{ch}}$ with an yz-coordinate system centered in the middle of the rectangle as illustrated in figure 5.1. The strategy will be to chose a desired boundary condition on the electric potential at the top and bottom boundaries and then proceed to determine the boundary conditions on the chamber sides afterwards. For a single sinusoidal mode, the boundary conditions on the electric potential are formulated as

$$w(y, z = \pm H_{\text{ch}}/2) = \sin\left(\frac{\pi y}{W_{\text{ch}}}\right), \qquad w(y = \pm W_{\text{ch}}/2, z) = \pm w(z), \qquad (5.57)$$

where $w(z)$ is some symmetrical function that we will choose later. The governing equation for the electric bulk potential is simply the Poisson equation

$$\nabla^2 \phi^{\text{b}}(y, z) = 0. \qquad (5.58)$$

We seek a separable solution of the form $\phi^{\text{b}}(y, z) = Y(y)Z(z)$. A qualified guess for the shape of the function is chosen as

$$\phi^{\text{b}}(y, z) = A \sin\left(\frac{\pi y}{W_{\text{ch}}}\right) \cosh\left(\frac{\pi z}{W_{\text{ch}}}\right). \qquad (5.59)$$

The boundary condition in Eq. (5.29) for $z = \pm H_{\text{ch}}/2$ yields

$$A \cosh\left(\frac{\pi H_{\text{ch}}}{2W_{\text{ch}}}\right) = V_0 \mp i\frac{\omega_{\text{D}}}{\omega} \frac{\pi}{\kappa_{\text{el}} W_{\text{ch}}} A \sinh\left(\pm \frac{\pi H_{\text{ch}}}{2W_{\text{ch}}}\right), \qquad (5.60)$$

or

$$A = \frac{V_0}{\cosh\left(\frac{\pi H_{\text{ch}}}{2W_{\text{ch}}}\right) + i\frac{\omega_{\text{D}}}{\omega} \frac{\pi}{\kappa_{\text{el}} W} \sinh\left(\frac{\pi H_{\text{ch}}}{2W_{\text{ch}}}\right)}. \qquad (5.61)$$

Applying the boundary condition at $y = \pm W_{\text{ch}}/2$, we find that

$$\pm A \cosh\left(\frac{\pi z}{W_{\text{ch}}}\right) = \pm V_0 w(z). \qquad (5.62)$$

Now, choosing that

$$w(z) = \frac{\cosh\left(\frac{\pi z}{W_{\text{ch}}}\right)}{\cosh\left(\frac{\pi H_{\text{ch}}}{2W_{\text{ch}}}\right) + i\frac{\omega_{\text{D}}}{\omega} \frac{\pi}{\kappa_{\text{el}} W_{\text{ch}}} \sinh\left(\frac{\pi H_{\text{ch}}}{2W_{\text{ch}}}\right)}, \qquad (5.63)$$

the solution for the electric bulk potential becomes

$$\phi^{\mathrm{b}}(y,z) = \frac{V_0 \sin\left(\frac{\pi y}{W_{\mathrm{ch}}}\right) \cosh\left(\frac{\pi z}{W_{\mathrm{ch}}}\right)}{\cosh\left(\frac{\pi H_{\mathrm{ch}}}{2W_{\mathrm{ch}}}\right) + \mathrm{i}\frac{\omega_{\mathrm{D}}}{\omega} \frac{\pi}{\kappa_{\mathrm{el}} W_{\mathrm{ch}}} \sinh\left(\frac{\pi H_{\mathrm{ch}}}{2W_{\mathrm{ch}}}\right)}. \tag{5.64}$$

With this, we find that

$$\partial_y \phi^{\mathrm{b}} \partial_z \phi^{\mathrm{b}*}\big|_{y=\pm W_{\mathrm{ch}}/2} = 0, \tag{5.65a}$$

$$\partial_z \phi^{\mathrm{b}} \partial_y \phi^{\mathrm{b}*}\big|_{z=\pm H_{\mathrm{ch}}/2} = \pm |A|^2 \frac{1}{4}\left(\frac{\pi}{W_{\mathrm{ch}}}\right)^2 \sinh\left(\frac{\pi H_{\mathrm{ch}}}{W_{\mathrm{ch}}}\right) \sin\left(\frac{2\pi y}{W_{\mathrm{ch}}}\right). \tag{5.65b}$$

Since $\hat{\boldsymbol{e}}_\parallel(y, z = \pm H_{\mathrm{ch}}/2) = \mp \hat{\boldsymbol{e}}_y$, the slip velocity is given by

$$\boldsymbol{v}_{\mathrm{slip}}^{\mathrm{ICEO}}(y = \pm W_{\mathrm{ch}}/2, z) = \boldsymbol{0}, \tag{5.66a}$$

$$\boldsymbol{v}_{\mathrm{slip}}^{\mathrm{ICEO}}(y, z = \pm H_{\mathrm{ch}}/2) = -\hat{\boldsymbol{e}}_y \frac{\epsilon_{\mathrm{f}} \lambda_{\mathrm{D}}}{16\eta}\left(\frac{\pi}{W_{\mathrm{ch}}}\right)^2 |A|^2 \sinh\left(\frac{\pi H_{\mathrm{ch}}}{W_{\mathrm{ch}}}\right) \sin\left(\frac{2\pi y}{W_{\mathrm{ch}}}\right). \tag{5.66b}$$

The solution has the optimal shape for stopping the classical Rayleigh type streaming, but the amplitude turns out to be vanishingly small. The solution grows towards a maximum and approximately constant value for frequencies in the regime $\omega_{\mathrm{D}}\pi\lambda_{\mathrm{D}}/W_{\mathrm{ch}} \ll \omega \ll \omega_{\mathrm{D}}$. In this limit, it is found that

$$\boldsymbol{v}_{\mathrm{slip}}^{\mathrm{ICEO}}(y, z = \pm H_{\mathrm{ch}}/2) \approx -\hat{\boldsymbol{e}}_y \frac{\epsilon_{\mathrm{f}} \lambda_{\mathrm{D}} V_0^2}{16\eta}\left(\frac{\pi}{W_{\mathrm{ch}}}\right)^2 \frac{\tanh\left(\frac{\pi H_{\mathrm{ch}}}{W_{\mathrm{ch}}}\right)}{\cosh\left(\frac{\pi H_{\mathrm{ch}}}{W_{\mathrm{ch}}}\right)} \sin\left(\frac{2\pi y}{W_{\mathrm{ch}}}\right). \tag{5.67}$$

Going back to the standard $H_{\mathrm{ch}} \times W_{\mathrm{ch}} = 160\,\mu\mathrm{m} \times 375\,\mu\mathrm{m}$ fluid cross section and keeping the remaining parameters from table 5.1, this corresponds to an amplitude of $3.97 \times 10^{-14}\,\mathrm{m/s}$. This can also be validated numerically, although the chosen boundary conditions turn out to produce numerically very unstable solutions, because $\partial_\perp \phi^{\mathrm{b}}(\boldsymbol{s}_0)\partial_\parallel \phi^{\mathrm{b}*}(\boldsymbol{s}_0)$ is strictly real. Since the electric bulk potential is complex, small numerical errors lead to imaginary parts in this term, which cause large deviations from the analytical expression. With such a small predicted streaming amplitude and high instability to small variations, this solution is rather academical and not very interesting for practical purposes.

One should also be aware of the way in which the boundary conditions on the electric potential were chosen to nicely fit the simple mode in the electric bulk potential. The boundary condition on the real electric potential happens to be discontinuous in the corners. As discussed above, this makes the simple mode nonphysical, but one should think of the mode as a guiding calculation for the overall shape of the potential.

We can use the analytical expression to illustrate the physical reasoning behind this vanishingly small streaming. The explanation is found from the expression for the charge density. Since

$$\nu = \mathrm{i}\frac{\omega_{\mathrm{D}}}{\omega} \frac{\epsilon_{\mathrm{f}} \kappa_{\mathrm{el}}}{Ze} \partial_\perp \phi^{\mathrm{b}}(\boldsymbol{s}_0)\, \mathrm{e}^{-\kappa_{\mathrm{el}} Z}, \tag{5.68}$$

and $\kappa_{\mathrm{el}} \approx 1/\lambda_{\mathrm{D}}$ for $\omega \ll \omega_{\mathrm{D}}$, the charge density is almost completely out of phase with $\partial_\perp \phi^{\mathrm{b}}(\boldsymbol{s}_0)$. A single mode will drag electric charge towards the surface through its perpendicular gradient and then vanish before the charge density is established. Thus, the parallel
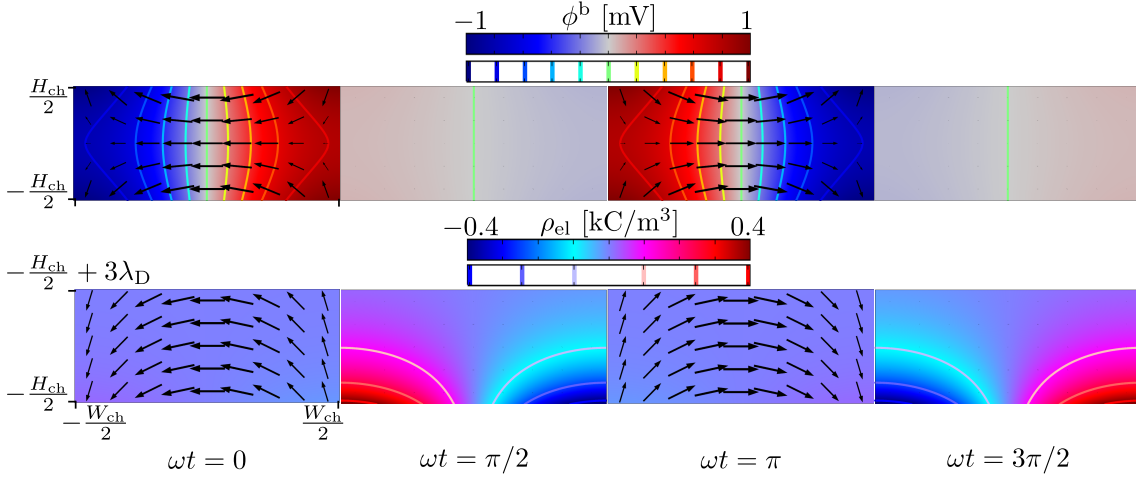
Figure 5.4: Field plots with Debye layer illustrations of a single ICEO mode shown at $\omega = 10\pi\omega_{\mathrm{D}}\lambda_{\mathrm{D}}/W$. The black arrows illustrate the electric bulk field $\boldsymbol{E}^{\mathrm{b}} = -\boldsymbol{\nabla}\phi^{\mathrm{b}}$, and the scaling is identical for all plots. The electric bulk potential ϕ^{b} is illustrated in the full chamber (above), and the electric charge density $\rho_{\mathrm{el}} = Ze\nu$ is illustrated in the thin Debye layer at the bottom boundary (below).

gradient will not get to act on the electric charge density. This is illustrated in figure 5.4, where field plots of the analytical electrostatic solution are shown for $\omega = 10\omega_{\mathrm{D}}\pi\lambda_{\mathrm{D}}/W_{\mathrm{ch}}$. The electric field associated with the bulk potential, $\boldsymbol{E}^{\mathrm{b}} = -\boldsymbol{\nabla}\phi^{\mathrm{b}}$, is also plotted alongside $\rho_{\mathrm{el}} = Ze\nu$ contours calculated from Eq. (5.32a) at the bottom boundary for the solution found above. Notice how the electric field lines vanish just as the Debye layer is fully established. To circumvent this, one could imagine running another mode in phase with the electric charge density. This possibility is explored in the following subchapter, where a linear mode is superimposed on a sinusiodal mode.

5.3.2   Double mode

To generate a desired double mode in the electric field, a boundary condition is chosen as the sum of a sinusoidal and a linear mode at the top and bottom boundaries. The calculation essentially goes like in the last example. The boundary conditions on the full electric potential are formulated as

$$
w(y, \pm H_{\mathrm{ch}}/2) = \left[\sin\left(\frac{2\pi y}{W_{\mathrm{ch}}}\right) + \mathrm{e}^{\mathrm{i}\theta}\frac{2y}{W_{\mathrm{ch}}}\right],
$$

$$
w(\pm W_{\mathrm{ch}}/2, z) = \pm\left[\left(1 + \mathrm{i}\frac{\omega_{\mathrm{D}}}{\omega}\frac{2}{\kappa_{\mathrm{el}}W_{\mathrm{ch}}}\right)\mathrm{e}^{\mathrm{i}\theta} - \mathrm{i}\left(\frac{\omega_{\mathrm{D}}}{\omega}\right)\frac{2\pi}{\kappa_{\mathrm{el}}W_{\mathrm{ch}}}\frac{\cosh\left(\frac{2\pi z}{W_{\mathrm{ch}}}\right)}{\cosh\left(\frac{\pi H_{\mathrm{ch}}}{W_{\mathrm{ch}}}\right) + \mathrm{i}\frac{\omega_{\mathrm{D}}}{\omega}\frac{2\pi}{\kappa_{\mathrm{el}}W_{\mathrm{ch}}}\sinh\left(\frac{\pi H_{\mathrm{ch}}}{W_{\mathrm{ch}}}\right)}\right],
$$
$$
(5.69)
$$

where θ is the phase constant of the linear mode. The Poisson equation with the boundary condition in Eq. (5.29) then yields the following solution for the electric bulk potential

$$\phi^{\mathrm{b}}(y,z) = \frac{V_0 \cosh\left(\frac{2\pi z}{W_{\mathrm{ch}}}\right) \sin\left(\frac{2\pi y}{W_{\mathrm{ch}}}\right)}{\cosh\left(\frac{\pi H_{\mathrm{ch}}}{W_{\mathrm{ch}}}\right) + \mathrm{i}\frac{\omega_{\mathrm{D}}}{\omega}\frac{2\pi}{\kappa_{\mathrm{el}}W_{\mathrm{ch}}}\sinh\left(\frac{\pi H_{\mathrm{ch}}}{W_{\mathrm{ch}}}\right)} + V_0 \frac{2y}{W_{\mathrm{ch}}}\mathrm{e}^{\mathrm{i}\theta}. \tag{5.70}$$

In the limit of $\omega \ll \omega_{\mathrm{D}}$ where $\kappa_{\mathrm{el}} \approx 1/\lambda_{\mathrm{D}}$, we approximately have

$$\partial_y \phi^{\mathrm{b}} \partial_z \phi^{\mathrm{b}*}\big|_{y=\pm W_{\mathrm{ch}}/2} = 0 \tag{5.71}$$

$$\partial_z \phi^{\mathrm{b}} \partial_y \phi^{\mathrm{b}*}\big|_{z=\pm H_{\mathrm{ch}}/2} = \pm \left(\frac{\pi V_0}{W_{\mathrm{ch}}}\right)^2 \frac{\sinh\left(\frac{2\pi H_{\mathrm{ch}}}{W_{\mathrm{ch}}}\right)\sin\left(\frac{4\pi y}{W_{\mathrm{ch}}}\right)}{\left|\cosh\left(\frac{\pi H_{\mathrm{ch}}}{W_{\mathrm{ch}}}\right) + \mathrm{i}\frac{\omega^*}{\omega}\sinh\left(\frac{\pi H_{\mathrm{ch}}}{W_{\mathrm{ch}}}\right)\right|^2}$$
$$\pm \frac{4\pi V_0^2}{W_{\mathrm{ch}}^2}\mathrm{e}^{\mathrm{i}\theta}\left[\frac{\frac{1}{2}\sinh\left(\frac{2\pi H_{\mathrm{ch}}}{W_{\mathrm{ch}}}\right)\sin\left(\frac{2\pi y}{W_{\mathrm{ch}}}\right) - \mathrm{i}\frac{\omega^*}{\omega}\sinh^2\left(\frac{\pi H_{\mathrm{ch}}}{W_{\mathrm{ch}}}\right)\sin\left(\frac{2\pi y}{W_{\mathrm{ch}}}\right)}{\cosh^2\left(\frac{\pi H_{\mathrm{ch}}}{W_{\mathrm{ch}}}\right) + \left(\frac{\omega^*}{\omega}\sinh\left(\frac{\pi H_{\mathrm{ch}}}{W_{\mathrm{ch}}}\right)\right)^2}\right], \tag{5.72}$$

where we defined $\omega^* = \omega 2\pi\lambda_{\mathrm{D}}/W_{\mathrm{ch}}$ following the notation in [36]. We notice that one of the real terms has a factor ω^*/ω, which could make it much larger than the imaginary terms for small frequencies $\omega \ll \omega^*$ with certain choices of θ. However, when inserted in Eq. (5.54) the imaginary term is multiplied by the factor $\omega_{\mathrm{D}}/\omega$. Because ω_{D} is a factor d/λ_{D} larger than ω^*, the imaginary part will indeed always dominate the slip velocity. Keeping only the imaginary term, we find the slip velocity

$$\boldsymbol{v}_{\mathrm{slip}}^{\mathrm{ICEO}}(\pm W_{\mathrm{ch}}/2, z) = \boldsymbol{0}, \tag{5.73a}$$

$$\boldsymbol{v}_{\mathrm{slip}}^{\mathrm{ICEO}}(y, \pm H_{\mathrm{ch}}/2) = \hat{\boldsymbol{e}}_y \frac{\epsilon_{\mathrm{f}}V_0^2}{\eta W_{\mathrm{ch}}}\sin\left(\frac{2\pi y}{W_{\mathrm{ch}}}\right)\frac{\frac{\omega^*}{\omega}\sinh^2\left(\frac{2\pi H_{\mathrm{ch}}}{W_{\mathrm{ch}}}\right)\cos(\theta) + \sinh\left(\frac{\pi H_{\mathrm{ch}}}{W_{\mathrm{ch}}}\right)\cosh\left(\frac{\pi H_{\mathrm{ch}}}{W_{\mathrm{ch}}}\right)\sin(\theta)}{\cosh^2\left(\frac{\pi H_{\mathrm{ch}}}{W_{\mathrm{ch}}}\right)\left(\frac{\omega}{\omega^*}\right) + \sinh^2\left(\frac{\pi H_{\mathrm{ch}}}{W_{\mathrm{ch}}}\right)\left(\frac{\omega^*}{\omega}\right)}. \tag{5.73b}$$

Again, the slip velocity is of the desired shape. However, this time it is of much larger amplitude than the expression derived in the previous subchapter. It should be noted that the direction of the streaming rolls may reverse depending on the chosen value of θ.

The peak amplitude of the slip velocity at $y = \pm W_{\mathrm{ch}}/4$ will of course vary with θ. We will denote the value of θ leading to the maximal peak amplitude by θ_{opt}. The expression $v_{y,\mathrm{slip}}^{\mathrm{ICEO}}(-W_{\mathrm{ch}}/4, \pm H_{\mathrm{ch}}/2)$ is differentiated with respect to θ and by setting this equal to zero at θ_{opt}, it is found that

$$\theta_{\mathrm{opt}} = \tan^{-1}\left[\frac{\omega}{\omega^*\tanh\left(\frac{\pi H_{\mathrm{ch}}}{W_{\mathrm{ch}}}\right)}\right] + n\pi, \qquad n \in \mathbb{N}. \tag{5.74}$$

It turns out that $n = $ even gives the Rayleigh slip velocity, and $n = $ odd produces a reversed Rayleigh slip velocity. We insert $n = 1$, and at this choice of θ the slip velocity becomes

$$\boldsymbol{v}_{\mathrm{slip}}^{\mathrm{ICEO}}(\pm W_{\mathrm{ch}}/2, z) = \boldsymbol{0}, \tag{5.75a}$$

$$\boldsymbol{v}_{\mathrm{slip}}^{\mathrm{ICEO}}(y, \pm H_{\mathrm{ch}}/2) = -\hat{\boldsymbol{e}}_y v^{\mathrm{ICEO}}\frac{\sin\left(\frac{2\pi y}{W_{\mathrm{ch}}}\right)}{\sqrt{1 + \frac{\omega^2}{\omega^{*2}\tanh^2\left(\frac{\pi H_{\mathrm{ch}}}{W_{\mathrm{ch}}}\right)}}}, \qquad v^{\mathrm{ICEO}} = \frac{\epsilon_{\mathrm{f}}V_0^2}{\eta W_{\mathrm{ch}}}. \tag{5.75b}$$

For the usual parameters, this means that at $\omega \ll \omega^* \tanh\left(\frac{\pi H_{\mathrm{ch}}}{W_{\mathrm{ch}}}\right) = 1.5\,\mathrm{kHz}$ the peak
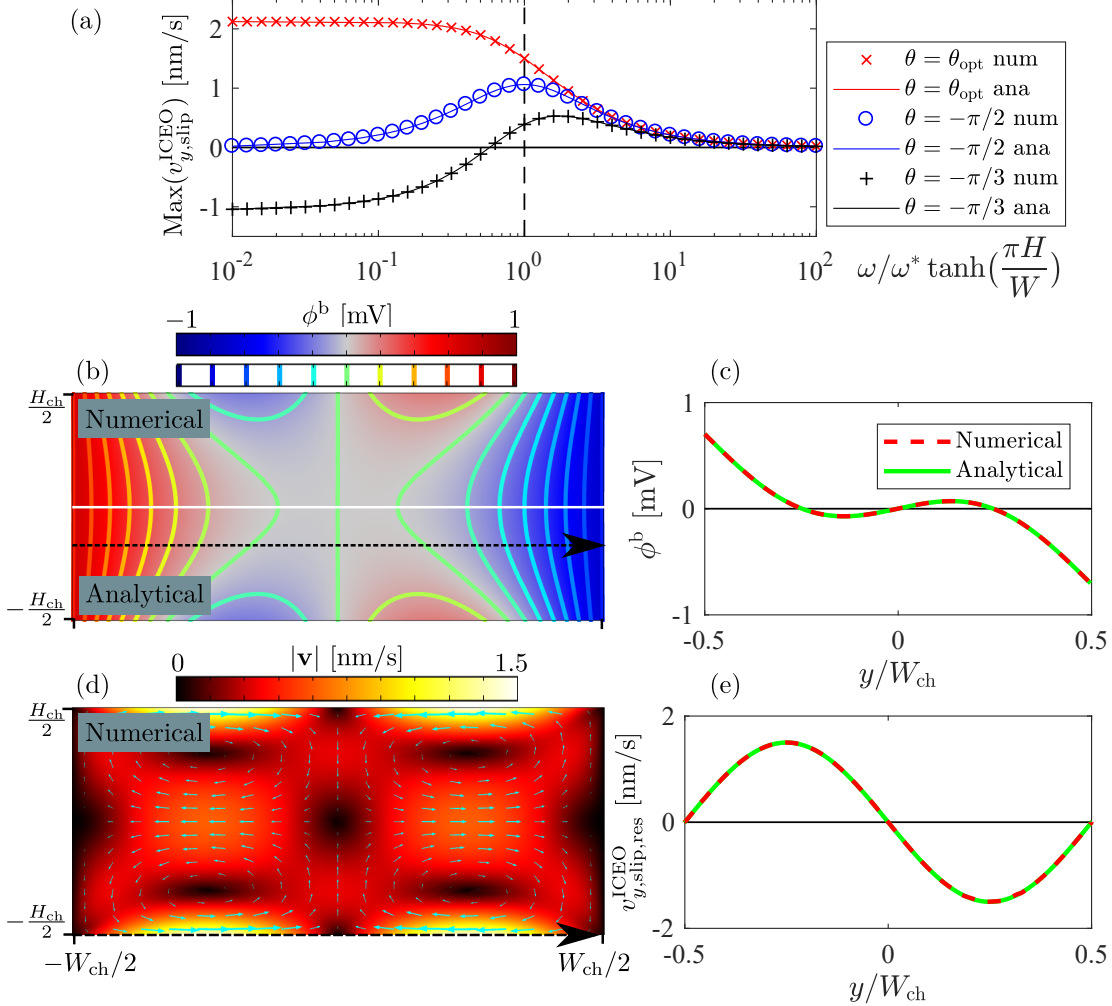

Figure 5.5: Analytical and numerical calculations for a simple ICEO double mode. (a) the peak amplitude of the parallel slip velocity at the top and the bottom walls of the fluid channel. (b) numerical and analytical field plots of the electric bulk potential with added contour lines shown at resonance. (c) numerical and analytical line plots of the electric bulk potential shown along the black dashed arrow indicated in (b). (d) field plots of the steady streaming at resonance. (e) parallel slip velocity plotted along the bottom boundary as indicated by the black dashed arrow in (d).

amplitude of the slip velocity will be $v^{\mathrm{ICEO}} = 2.1\,\mathrm{nm/s}$. This is a factor of $d/\lambda_{\mathrm{D}} \approx 10^5$ larger than what was found for the single mode. However, some care should be taken in terms of this result. Turning back to the boundary condition in Eq. (5.69), we see that the amplitude of the applied potential at the chamber sides will be much larger
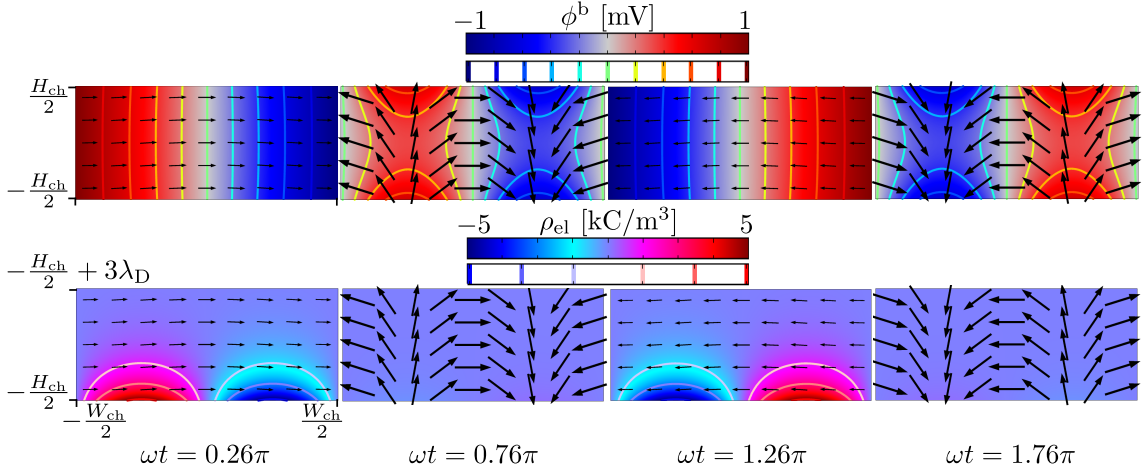
Figure 5.6: Field plots with Debye layer illustrations of a double ICEO mode shown at $\omega = \omega^* \tanh\left(\frac{\pi H_{\mathrm{ch}}}{W_{\mathrm{ch}}}\right)$. The black arrows illustrate the electric bulk field $\boldsymbol{E}^{\mathrm{b}} = -\boldsymbol{\nabla}\phi^{\mathrm{b}}$, and the scaling is identical for all plots. The electric bulk potential ϕ^{b} is illustrated in the full chamber (above), and the electric charge density $\rho_{\mathrm{el}} = Ze\nu$ is illustrated in the thin Debye layer at the bottom boundary (below).

than V_0 for $\omega \ll \omega^*$. Luckily, the amplitude of the streaming does not drop particularly fast for increasing ω, and at e.g. $\omega = \omega^* \tanh\left(\frac{\pi H_{\mathrm{ch}}}{W_{\mathrm{ch}}}\right)$ we still have a slip velocity of $v^{\mathrm{ICEO}}/\sqrt{2} = 1.5\,\mathrm{nm/s}$ for $|\phi(\boldsymbol{s}_0)| \sim V_0 = 1\,\mathrm{mV}$.

For different choices of θ, there can be finite and non-zero resonance frequencies, and the direction of the rolls may switch depending on the frequency. This is illustrated in figure 5.5, where the analytical solution is compared to numerics for different θ and varying ω. Furthermore, field plots of the optimal phase solution are also shown at $\omega = \omega^* \tanh\left(\frac{\pi H_{\mathrm{ch}}}{W_{\mathrm{ch}}}\right)$. Excellent agreement is seen between the numerical solutions and the analytical expressions for both the potential and the slip velocity. It turns out that $\omega^* \tanh\left(\frac{\pi H_{\mathrm{ch}}}{W_{\mathrm{ch}}}\right)$ is the resonance frequency for $\theta = -\pi/2$. This result is easily shown analytically by inserting $\theta = -\pi/2$ into Eq. (5.75b) and optimising the amplitude with respect to ω.

The physics behind this much increased streaming is presented in figure 5.6 through another series of field plots with the Debye layer illustrated. The electrostatic fields are plotted at $\omega = \omega^* \tanh\left(\frac{\pi H_{\mathrm{ch}}}{W_{\mathrm{ch}}}\right)$ for $\theta = \theta_{\mathrm{opt}}$. Now we notice that the linear mode is present alongside the charge density established by the sinusoidal mode. As the charge density switches sign, the electric field from the linear mode also turns, leading to a body force constantly directed towards the center of the chamber. Changing the phase by π will of course simply reverse this pattern.

Another way of generating the reverse Rayleigh slip velocity is to combine sinusoidal modes out of phase. When the modes deviate by a full wavelength, a Rayleigh or reverse Rayleigh streaming pattern is generated depending on their phase difference. These solutions do not add much new to the analysis above, and the discussion is left to the appendix.

5.4   Higher voltages

To linearise the theory of ICEO and eventually develop the effective theory presented above, we had to assume that $V_0 \ll V_\mathrm{T}$. This led to streaming velocities around $1.5\,\mathrm{nm/s}$ at $V_0 = 1\,\mathrm{mV}$. Extrapolating the linearised theory to higher voltages, Eq. (5.75b) suggests that one would need around $V_0 = 260\,\mathrm{mV}$ or $V_0 \approx 10V_\mathrm{T}$ to generate streaming of the order of $100\,\mathrm{\mu m/s}$. We notice that the required voltage is close to the critical potential calculated in Eq. (4.22) thus bringing us into the steric regime.

We will not take into account steric effects in this thesis. The guiding value of $|\boldsymbol{v}| \approx 100\,\mathrm{\mu m/s}$ is not a strict limit either way, and one could significantly lower this by using weaker acoustical fields. However, this will also cause a corresponding decrease in the acoustic radiation force accountable for the wanted particle sorting. Certainly, one will need to at least leave the linear regime for many experimental purposes. Thus, it is necessary to study the fully non-linear problem. In the following, we will simulate the full time-dependent electrokinetic problem, and it is explored how well the linear approximation describes the qualitative behaviour of the system, when the non-linear effects become significant.

5.4.1   Numerical implementation

We now implement the full non-linear and time-dependent electrokinetic problem stated in Eq. (5.1) in COMSOL. Going from a linearised frequency domain calculation to a fully non-linear and time-dependent calculation will not only complicate analytical calculations, as numerical computations start to become unstable for increasing non-linearities. The following study is largely inspired by the work presented in [22].

The oscillation period is denoted by T and given by

$$T = \frac{2\pi}{\omega}. \tag{5.76}$$

We consider the same mode that we just treated with the boundary conditions in Eq. (5.69). For the full time-dependent simulations, the phasor notation is discarded, and everything is implemented as real and time-dependent fields. The optimal phase difference $\theta = \theta_\mathrm{opt}$ and $\omega = \omega^* \tanh\!\left(\frac{\pi H_\mathrm{ch}}{W_\mathrm{ch}}\right)$ are implemented in all simulations. The only varying parameter will thus be V_0 that is gradually increased into the non-linear regime.

To help the full simulations converge, the inconsistency in the boundary condition at the corners is fixed. Rounded corners of radius $R = 1000\lambda_\mathrm{D} \approx 9.7\,\mathrm{\mu m}$ are implemented, and the two symmetry planes in the problem are utilised to simulate only a quarter of the geometry as illustrated in figure 5.7.

The boundary condition on the potential follows the form from Eq. (5.69) outside of the curved corner. The potential values at the two edges of the quarter circular corner marked with red dots in figure 5.7 are denoted ϕ_1 and ϕ_2. From these points, the potential is "stitched" together by a smooth interpolation function on the quarter circle. The function is chosen to generate a surface potential, which is both continuous and has a continuous first-order derivative along the boundary. For this, a third-order polynomial in the corner

angle φ is chosen. The potential values at the two edges are

$$\phi_1 = \phi(W_{\text{ch}}/2, H_{\text{ch}}/2 - R, t) = \text{Re}\left\{V_0 e^{-i\omega t}\left[\left(1 + i\frac{\omega_{\text{D}}}{\omega}\frac{2}{\kappa_{\text{el}}W_{\text{ch}}}\right)e^{i\theta}\right.\right. \tag{5.77a}$$

$$\left.\left. - i\left(\frac{\omega_{\text{D}}}{\omega}\right)\frac{2\pi}{\kappa_{\text{el}}W_{\text{ch}}}\frac{\cosh\left(\frac{2\pi(H_{\text{ch}}/2-R)}{W_{\text{ch}}}\right)}{\cosh\left(\frac{\pi H_{\text{ch}}}{W_{\text{ch}}}\right) + i\frac{\omega_{\text{D}}}{\omega}\frac{2\pi}{\kappa_{\text{el}}W_{\text{cg}}}\sinh\left(\frac{\pi H_{\text{ch}}}{W_{\text{ch}}}\right)}\right]\right\},$$

$$\phi_2 = \phi(W_{\text{ch}}/2 - R, H_{\text{ch}}/2, t) = \text{Re}\left\{V_0 e^{-i\omega t}\left[\sin\left(\frac{2\pi(W_{\text{ch}}/2 - R)}{W_{\text{ch}}}\right) + e^{i\theta}\frac{2(W_{\text{ch}}/2 - R)}{W_{\text{ch}}}\right]\right\}. \tag{5.77b}$$

Correspondingly, we have the first-order derivatives along the boundaries

$$\phi_1' = \partial_z\phi(W_{\text{ch}}/2, H_{\text{ch}}/2 - R, t) = -\text{Re}\left\{V_0\, e^{-i\omega t}\left(\frac{\omega_{\text{D}}}{\omega}\right)\frac{i}{\kappa_{\text{el}}}\frac{\left(\frac{2\pi}{W_{\text{ch}}}\right)^2\sinh\left(\frac{2\pi(H_{\text{ch}}/2-R)}{W_{\text{ch}}}\right)}{\cosh\left(\frac{\pi H_{\text{ch}}}{W_{\text{ch}}}\right) + i\frac{\omega_{\text{D}}}{\omega}\frac{2\pi}{\kappa_{\text{el}}W_{\text{ch}}}\sinh\left(\frac{\pi H_{\text{ch}}}{W_{\text{ch}}}\right)}\right\}, \tag{5.78a}$$

$$\phi_2' = \partial_y\phi(W_{\text{ch}}/2 - R, H_{\text{ch}}/2, t) = \text{Re}\left\{V_0\, e^{-i\omega t}\left[\frac{2\pi}{W_{\text{ch}}}\cos\left(\frac{2\pi(W_{\text{ch}}/2 - R)}{W_{\text{ch}}}\right) + e^{i\theta}\frac{2}{W_{\text{ch}}}\right]\right\}. \tag{5.78b}$$

Between the two edges of the rounded corner, the potential takes the form

$$\phi_{\text{corner}}(\varphi) = C_0 + C_1\varphi + C_2\varphi^2 + C_3\varphi^3, \qquad \varphi = \arctan\left(\frac{z - H_{\text{ch}}/2 + R}{y - W_{\text{ch}}/2 + R}\right). \tag{5.79}$$

Now, requiring that

$$\phi_{\text{corner}}(\varphi = 0) = \phi_1, \qquad\qquad \phi_{\text{corner}}\left(\varphi = \frac{\pi}{2}\right) = \phi_2, \tag{5.80}$$

$$\partial_\varphi\phi_{\text{corner}}(\varphi = 0) = R\phi_1', \qquad\qquad \partial_\varphi\phi_{\text{corner}}\left(\varphi = \frac{\pi}{2}\right) = -R\phi_2',$$

we find that

$$C_0 = \phi_1, \qquad\qquad\qquad\qquad C_1 = R\phi_1', \tag{5.81}$$

$$C_2 = -\frac{2(2\pi R\phi_1' - \pi R\phi_2' + 6[\phi_1 - \phi_2])}{\pi^2}, \qquad C_3 = \frac{4\pi R(\phi_1' - \phi_2') + 16(\phi_1 - \phi_2)}{\pi^3}.$$

To enable COMSOL to get a grasp of the solution, the voltage is gradually ramped up during the first oscillation period through the function

$$V_0(t) = V_0^\infty\frac{1}{2}\left(1 + \tanh\left[\frac{\omega t}{0.2} - 3\right]\right). \tag{5.82}$$

Furthermore, the advective term in the Nernst–Planck equation $c_\pm\boldsymbol{v}$ is only implemented for $t > 0.1T$. Hopefully, this does not influence the solutions significantly, as the streaming is rather low for initial time steps. The generalized alpha solver is used in COMSOL with
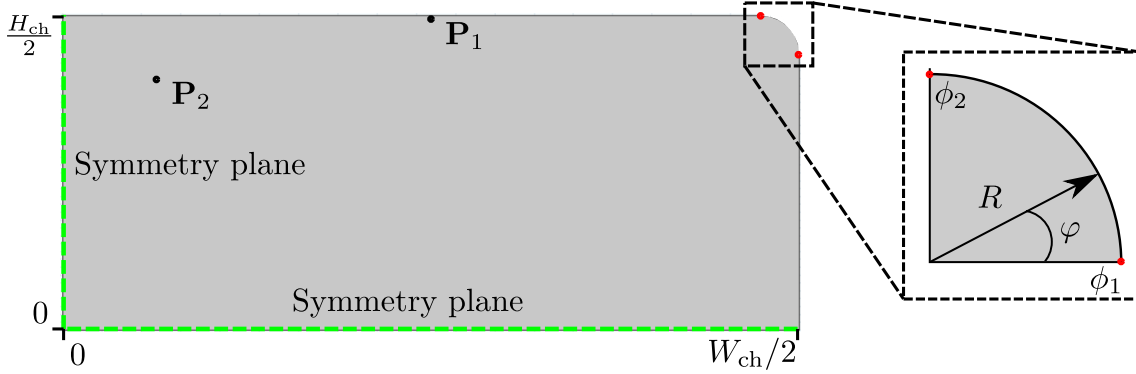
Figure 5.7: Geometry for full non-linear and time-dependent simulations. The two symmetry planes of the problem are utilised to lower computational footprint, and the top right corner is rounded. The red dots mark the bounds of the interpolation function used to generate a consistent boundary condition on the potential.

constant time stepping set to $dt = T/128$ and a damping factor of 0.5. For voltages above $V_0^\infty = 1\,\text{mV}$, the Jacobian of the system was set to update at every iteration to increase stability.

In the voltage range where the linearised theory is valid, we assume the velocity to follow the form

$$\boldsymbol{v}(\boldsymbol{r}, t) = \boldsymbol{v}^0(\boldsymbol{r}, t) + \boldsymbol{v}^{2\omega}(\boldsymbol{r}, t)\cos(2\omega t), \qquad (5.83)$$

where the time-dependencies of $\boldsymbol{v}^0$ and $\boldsymbol{v}^{2\omega}$ describe an initial transient period until the flow is fully built up. The solutions can then be time-averaged, and after the transient period we would expect to find a $\boldsymbol{v}^0$ that is essentially equal to a solution found in the frequency regime with the linearised theory. This is similar to the method in [22], where around 1000 oscillation periods were needed to reach a stable solution. In this article, the transient study was performed for an acoustic resonance that builds up gradually in time due to constructive interference of waves. We do not expect that nearly as many oscillations are needed to develop the electrokinetic flow, since this is not resonating in nature. In the remaining part of the chapter, solutions found in the transient simulations are denoted with explicit time-dependency $\phi(\boldsymbol{r}, t)$ and $\boldsymbol{v}(\boldsymbol{r}, t)$, whereas the solutions found in the linearised frequency regime are denoted $\phi(\boldsymbol{r})$ and $\boldsymbol{v}(\boldsymbol{r})$.

The time-average of a field $\boldsymbol{A}(\boldsymbol{r}, t)$ is given by

$$\langle \boldsymbol{A}(\boldsymbol{r}, t)\rangle = \int_{t-T/2}^{t+T/2} \boldsymbol{A}(\boldsymbol{r}, t')\,dt'. \qquad (5.84)$$

The integration is performed in Matlab as a fifth-order Romberg integration scheme adapted from the supplementary material of [22].
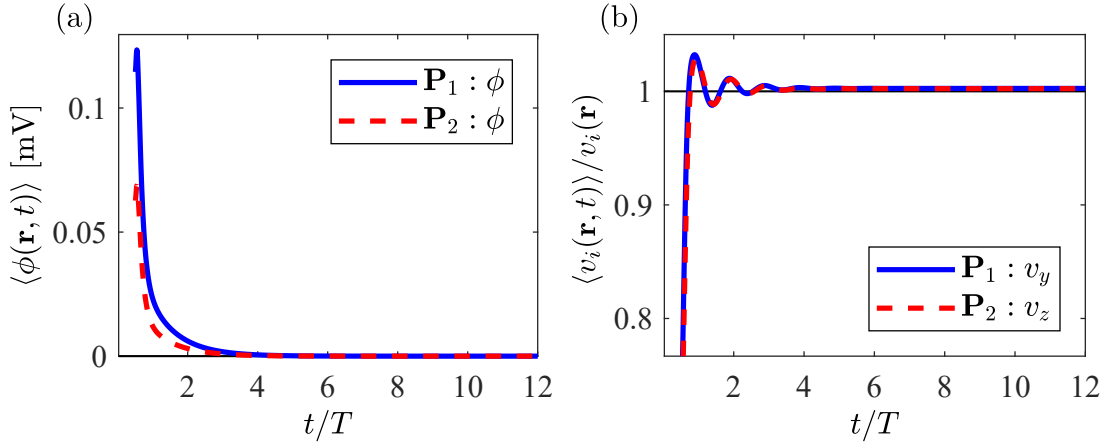
Figure 5.8: Test of the transient period of our ICEO flow at $V_0^\infty = 1\,\text{mV}$. (a) the time-averaged electric potential $\langle \phi(\boldsymbol{r}, t) \rangle$ in the two points $\boldsymbol{P}_1$ and $\boldsymbol{P}_2$. (b) time-averaged and normalised fluid velocity components $\langle v_i(\boldsymbol{r}, t) \rangle / v_i(\boldsymbol{r})$ in the two points.

5.4.2   Results

First, we check whether or not we can reproduce a frequency domain result with a transient simulation at $V_0^\infty = 1\,\text{mV}$. For this, we simulate the above mentioned geometry and boundary conditions in the frequency regime and for the full equations. To check when a stable solution is reached, we plot the time-average of the physical fields $\phi(\boldsymbol{r}, t)$ and $\boldsymbol{v}(\boldsymbol{r}, t)$ in two different points of the solution for different times. The two chosen points are $\boldsymbol{P}_1 = (y_1, z_1) = (W_\text{ch}/4, H_\text{ch}/2 - 5\lambda_\text{D})$ and $\boldsymbol{P}_2 = (y_2, z_2) = (W_\text{ch}/8, H_\text{ch}/2.5)$, which are also illustrated in figure 5.7. The resulting time-averaged fields are found in figure 5.8, where the velocity field components are normalised with respect to those found in the frequency domain $v_i(\boldsymbol{r})$. We notice some initial oscillations in the time-averaged velocity field that dampen out exponentially in time. Simultaneously, the time-averaged electric potential goes towards zero as expected. After 4 to 5 oscillations, the flow appears to be very stable. The described simulation took approximately 12 minutes per oscillation period. Unfortunately, this increases to around 8 hours per oscillation period, when the Jacobian has to update at every iteration for higher voltages. Due to limitations in time, we go close to the limit of the steady area and only simulate the first four oscillations corresponding to a best possible time-averaged value evaluated at $t = 3.5T$. For the case of $V_0^\infty = 1\,\text{mV}$, this still brings us well within 1% of the steady level of the time-averaged fields, and the assumption will be that this trend continuous for higher voltages.

The time-averaged velocity field at $t = 3.5T$ for the transient $V_0^\infty = 1\,\text{mV}$ simulation is shown alongside the corresponding frequency domain simulation in figure 5.9. We see a remarkably close resemblance between the fields, which serves as a validation of the compatibility of the respective theories. Both the analytical expression for the electric potential without the rounded corners and the corresponding effective simulation of the vertical velocity component are also plotted in the line plots. We notice that the solution

only got slightly perturbed by fixing the boundary conditions.

Next, the voltage was gradually increased, and the time-averaged velocity was probed in P_1 and P_2 as a function of the applied voltage. The resulting values are plotted in figure 5.10, and the expected scaling of $(V_0^\infty)^2$ from the linearised theory is plotted on top. We notice that the linearised theory appears to predict the quantitative values very well even at $V_0^\infty = 75\,\text{mV}$, where the theory was expected to have broken down. This was the highest voltage where a solution was attained. A field plot of the transient time-averaged solution compared to the frequency regime calculation can be found in the appendix. The figure is completely analogue to the one found in figure 5.9, where strong qualitative and quantitative agreement between the simulations is seen. Further inspection reveals that the transient theory predicts streaming velocities approximately 1% lower than the linearised theory at this point.

Higher voltages were also attempted, but for $V_0^\infty = 100\,\text{mV}$ the described procedure did not converge. A change to the BFL solver, which should be more stable and well suited for diffusion/advection problems [37], was also attempted with no resulting convergence. Due to limitations in time, no further numerical schemes were attempted to solve the convergence problem for higher voltages.
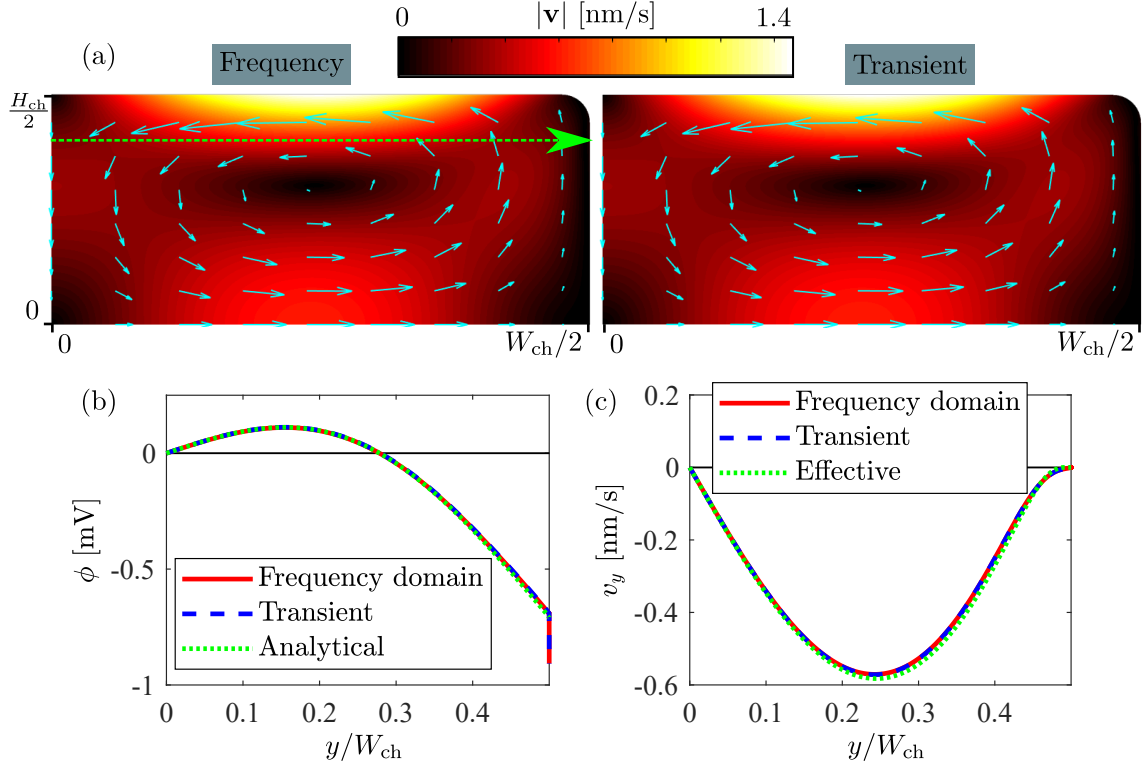
Figure 5.9: 1 mV ICEO flow calculated transient and in the frequency domain. (a) field plots of the velocity fields. Both the frequency domain simulation and the time-averaged transient results are shown. Line plots are shown along the green dashed arrow at $z = H/2.5$. (b) the electric potential calculated with the transient simulations and in the frequency domain shown at $\omega t = 3T$ (the beginning of the fourth oscillation, corresponding to the real part of the frequency domain $\phi(\boldsymbol{r})$). The analytical result without the curved corners from Eq. (5.70) is plotted on top. (c) horizontal component of the time-averaged velocity field from the transient simulation and from the frequency domain calculation. The effective simulation without the curved corners is shown on top.
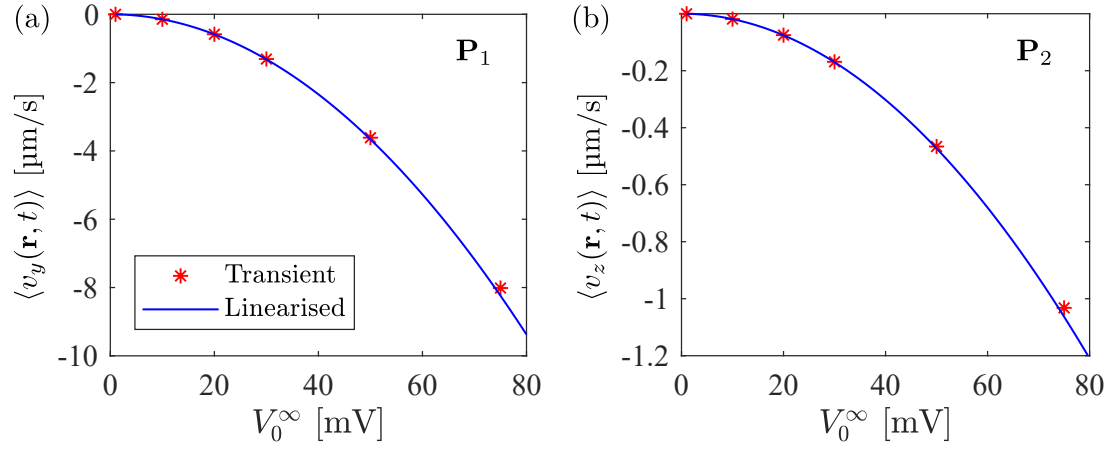
Figure 5.10: Time-averaged ICEO streaming amplitudes plotted for varying applied voltages at $\boldsymbol{P}_1$ and $\boldsymbol{P}_2$. (a) $\langle v_y(\boldsymbol{r}, t)\rangle$ plotted in $\boldsymbol{P}_1$. (b) $\langle v_z(\boldsymbol{r}, t)\rangle$ plotted in $\boldsymbol{P}_2$. The predicted values from the linearised theory are shown on top.

6 | Combined acoustics and induced charge electroosmosis

In the previous chapter, our theory of ICEO was based on some surface potential $\phi(\boldsymbol{s}_0, t)$ that is evaluated on the stationary chamber walls at $\boldsymbol{s}_0$. When acoustics are applied, the electric surface potential will be evaluated on a surface shifting its position in time. Because we now have two separate frequencies (the acoustic and the electric), the notation ω_{ac} is introduced for the acoustic angular frequency, whereas ω remains to be the frequency of the alternating current. The boundary condition on the potential thus becomes

$$\phi(\boldsymbol{s}_0 + \tilde{\boldsymbol{s}}_1) = \mathrm{Re}\{V_0 w(\boldsymbol{s}_0 + \tilde{\boldsymbol{s}}_1) \exp(-\mathrm{i}\omega t)\}, \qquad \tilde{\boldsymbol{s}}_1 = \mathrm{Re}\{\boldsymbol{s}_1 \exp(-\mathrm{i}\omega_{\mathrm{ac}} t)\}, \qquad (6.1)$$

where w is some function of the wall position. To take into account the motion of the wall in the acoustic boundary layer theory, Bach and Bruus [4] made a Taylor expansion in $\boldsymbol{v}(\boldsymbol{s}_0 + \tilde{\boldsymbol{s}}_1)$, where they assumed smallness of $\boldsymbol{s}_1$ compared to the boundary layer thickness. The expected wall deflections in microchannels under acoustic actuation are typically of the order of nanometer, which make them comparable to the thickness of the Debye layer. This could make for a quite complicated theory of ICEO if the wall motion was to be taken into account.

Luckily, we found that the desired operating frequency of ICEO, $\omega \sim 1500$ rad/s, is around four orders of magnitude lower than the typical acoustic resonance frequency, $\omega_{\mathrm{res}} \sim 10^7$ rad/s. Thus, we can reasonably assume the two phenomena to be separated so heavily in time that they will not influence each other. Physical phenomena on the timescale of the electric oscillations will happen during thousands of acoustic oscillations. Due to this, they will appear to happen at the time-averaged wall position. The time-averaged wall position is of course simply $\boldsymbol{s}_0$ for time-harmonic acoustic actuations.

The non-linear advective term in the Nernst–Planck equation did not influence the DC electroosmotic problem, but for ICEO at $|\boldsymbol{v}| \sim 100\,\mu\mathrm{m/s}$ this term can heavily influence the problem. One could then worry that the acoustic streaming would also couple into the electrokinetic problem through this term. Because the Debye layer is much thinner than the viscous boundary layer, the acoustic streaming has only reached a fraction of its maximum value in the Debye layer. As long as equally large acoustic and electroosmotic streaming is assumed, the electroosmotic streaming will dominate the behaviour of the ionic advection. The theory of ICEO for streaming velocities of similar magnitude to the acoustic streaming was formulated as a Stokes flow with a non-linear electric body force.

With the separation in length- and timescales, the two theories should combine trivially to the sum of the acoustic streaming and the ICEO streaming.

The highest voltage ICEO streaming we managed to simulate at $V_0^\infty = 75\,\mathrm{mV}$ reached a peak streaming amplitude of a little over $8\,\mu\mathrm{m/s}$. Compared to typical acoustic streaming velocities, this is a bit in the low end but within an order of magnitude of typical values. The acoustic streaming scales with the square of the driving voltage (or in this thesis the set displacement amplitude d_0), and one can simply lower this to reach an acoustic streaming peak amplitude of $8\,\mu\mathrm{m/s}$. This can at least show us theoretically how well the considered ICEO mode matches the streaming of the acoustic half-wave mode in terms of qualitative patterns. For the acoustics simulations, the corner is rounded to match the ICEO geometry from the end of the previous chapter. The rounded corners remain at rest in the acoustics simulations, and only the vertical sides are actuated. We use the same actuation pattern as for the standard acoustics simulations given in Eq. (3.9). A new resonance frequency is probed for by sweeping in frequency and finding the maximal average acoustic energy density

$$E_{\mathrm{ac}} = \frac{1}{4}\rho_0|\boldsymbol{v}_1|^2 + \frac{1}{4}\kappa_{\mathrm{s}}|p_1|^2. \tag{6.2}$$

The resonance frequency $f_{\mathrm{ac,res}}$ only changes slightly from $1.993\,\mathrm{MHz}$ to 1.996 MHz. On resonance, the acoustic first-order pressure and the acoustic streaming qualitatively resemble that of the standard acoustics simulation with the amplitude being slightly lowered. Lastly, the value of d_0 is changed to match the horizontal component of the acoustic streaming with that of the time-averaged ICEO simulation at $V_0^\infty = 75\,\mathrm{mV}$ in the point $(y, z) = (W_{\mathrm{ch}}/4, H_{\mathrm{ch}}/2.5)$.

The separate streaming patterns are shown together with the sum of the two in figure 6.1. Contours are shown for areas where the streaming amplitude exceeds $0.5\,\mu\mathrm{m/s}$. For the combined phenomena, this only happens at the boundaries, where we have a mismatch between the length scales of the establishment of acoustic streaming and ICEO. Line plots are also presented of the streaming with a zoom-in on the boundary layer. We notice how the rapid growth of the velocity field in the Debye layer ends up acting as an offset for the acoustic streaming that tends close to zero at the end of the viscous boundary layer. This is of course exactly what was previously captured by using two separate slip velocities in our study of DC electroosmosis combined with acoustic streaming.
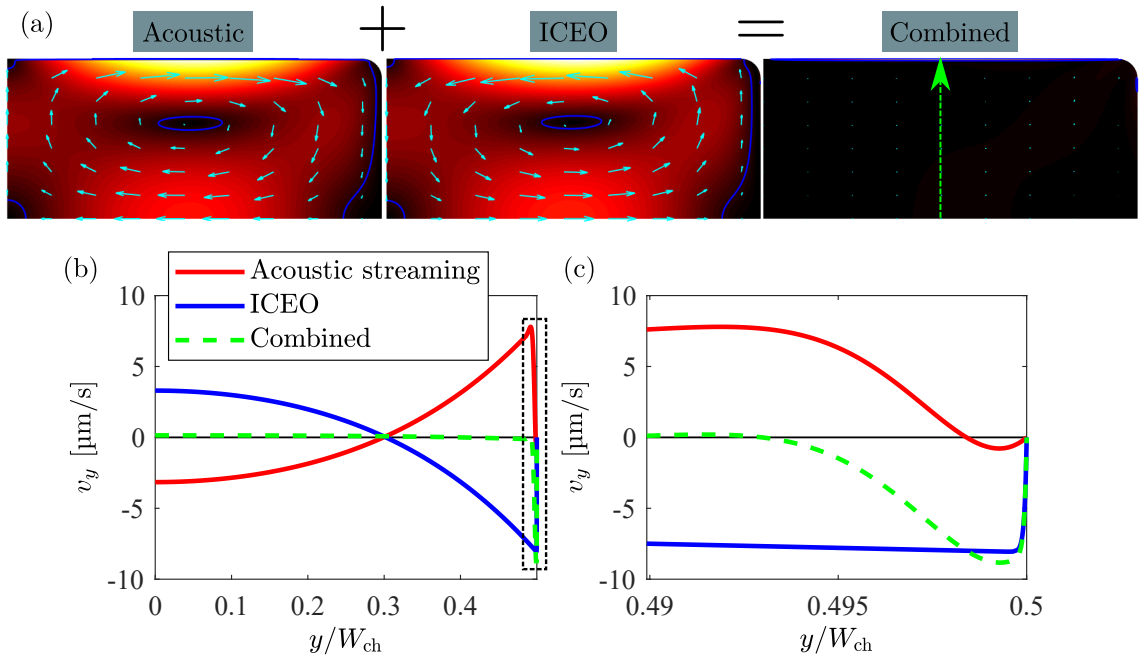
Figure 6.1: Acoustic streaming combined with ICEO double mode. (a) equally scaled field plots of the acoustic streaming, the ICEO double mode, and the combined streaming, respectively. (b) the horizontal velocity component v_y (or v_{2y} in case of the acoustic streaming) plotted along the green dashed arrow in (a). (c) zoom-in on the boundary layer region marked in (b).

7 | Conclusion and outlook

The two separate physical phenomena of acoustic streaming and electroosmotic flows were discussed. We used the Stokes flow formulations of acoustic streaming and DC electroosmosis alongside a fast relaxation time of ions due to convection to argue that the two phenomena combine trivially.

Due to the boundary driven nature of both electroomosis and acoustic streaming, we were able to suggest potential microfluidic designs with integrated acoustics and controlled electroomosis that could drastically reduce acoustic streaming. We demonstrated how optimisation algorithms could be integrated into numerical simulations to optimise the setups.

We then discussed a series of problems that may be associated with the use of DC electroosmosis. The problems related to a generation of a tranverse electric field appear rather tedious to resolve experimentally. A more thorough theoretical study of the potential solutions to this electrokinetic problem and their influence on the acoustic problem could be conducted in future work. To circumvent the trouble of the complete electrode screening, we then turned to a study of induced charge electroosmosis.

We analytically and numerically validated an effective slip velocity for the low voltage limit of ICEO theory. The effective theory was in turn used to perform analytical calculations that guided us towards the working principles of an ICEO reverse Rayleigh streaming pattern. This study led us towards the exploration of multi-mode ICEO, where optimal phase-differences between the separate modes could be found analytically. The physics behind a significantly increased streaming through the combination of modes was revealed to be a manifestation of phase-matching between the electric field of one mode and the electric charge density generated from the other mode.

The work done in the low voltage regime was extended into the more non-linear regime through full numerical simulations. These simulations showed strong agreement between the linearised theory and the time-average of the full non-linear dynamics at unexpectedly high voltages. We successfully simulated transient electrokinetic flows close to $3V_{\mathrm{T}}$.

Lastly, we argued that also ICEO combines trivially with acoustic streaming for experimentally relevant driving frequencies due to a vast seperation in timescales. A combination of a standard acoustics simulation and the strongest simulated ICEO flow suggested that a significant streaming reduction could be attained through a simple ICEO double mode.

In future work, one could look into the reasoning behind the unexpectedly high area of validity for the linearised ICEO theory. Furthermore, it would be of practical interest to extend further into the non-linear regime to reach higher streaming velocities. It would also

be of interest to gradually increase the realism of the system to include external electrodes. One could also take into account the presence of a chemically generated surface potential.

For both DC electroomosis and ICEO, we could introduce mechanical vibrations and a piezoelectric transducer in future work to simulate fully functional microfluidic systems with integrated acoustics and electroosmosis. With the established effective boundary layer models, one could also attempt to model full three-dimensional systems to increase realism. Lastly, we should undergo a more thorough study of optimal materials for said designs. Our hope is that more elaborate models of these systems could eventually motivate an experimental study and lead to effective control over the often problematic acoustic streaming.

A | Analytical Stokes flow above infinite half-plane

We here show an interesting analytical calculation connected to the external electrode tests in chapter 4.2, which turned out not to be very relevant for the project. When the externally applied potential is low enough that

$$\frac{Ze\lambda_D}{2k_BT}\frac{\epsilon_{\rm s}}{\epsilon_{\rm f}}\partial_\perp\phi_{\rm eq}^{\rm s}(\boldsymbol{s}_0) \ll 1, \tag{A.1}$$

we find from Eq. (4.13) that

$$\boldsymbol{v}_{2,\rm slip}^{\rm EO} \approx \frac{\lambda_{\rm D}\epsilon_{\rm f}}{\eta}\partial_\perp\phi_{\rm eq}^{\rm s}(\boldsymbol{s}_0)\boldsymbol{E}_{\rm ext\parallel}(\boldsymbol{s}_0). \tag{A.2}$$

Considering an infinite half-plane at $z = 0$ over an external cylindrical wire, we find an approximate slip velocity of the shape

$$\boldsymbol{v}_2(y,0) = \hat{\boldsymbol{e}}_y\frac{A}{y^2 + B^2}. \tag{A.3}$$

For at simple incompressible Stokes flow governed by

$$0 = \boldsymbol{\nabla}\cdot\boldsymbol{v}_2, \tag{A.4a}$$

$$\boldsymbol{0} = -\boldsymbol{\nabla}p_2 + \eta\nabla^2\boldsymbol{v}_2, \tag{A.4b}$$

this can be solved analytically. The classical Rayleigh calculation for a Stokes flow with boundary condition

$$\boldsymbol{v}_2^{\rm Rayleigh}(y,0) = \hat{\boldsymbol{e}}_yA\cos(ky), \tag{A.5}$$

yields the solution

$$\boldsymbol{v}_2^{\rm Rayleigh}(y,z) = Ae^{-kz}\big[\hat{\boldsymbol{e}}_y\cos(ky)(1-kz) + \hat{\boldsymbol{e}}_z\sin(kz)kz\big]. \tag{A.6}$$

We now use the following Fourier transformation

$$\mathcal{F}\{\frac{A}{y^2 + B^2}\} = \frac{A}{\sqrt{2\pi}}\int_{-\infty}^{\infty}\frac{\exp(\mathrm{i}ky)}{y^2 + B^2}\,\mathrm{d}y = \frac{A}{B}\sqrt{\frac{\pi}{2}}e^{-B|k|}. \tag{A.7}$$

From the inverse Fourier transform, we find that

$$\frac{A}{y^2 + B^2} = \frac{A}{B} \int_0^\infty \cos(ky) \mathrm{e}^{-Bk} \, \mathrm{d}k. \tag{A.8}$$

The boundary condition in Eq. (A.3) can thus be formulated as an integral over the Rayleigh slip velocity, and the full solution can correspondingly be formulated as an integral over the Rayleigh solutions.

$$v_{2y}(y, 0) = \frac{A}{y^2 + B^2} = \frac{A}{B} \int_0^\infty \cos(ky) \, \mathrm{e}^{-Bk} \, \mathrm{d}k, \tag{A.9}$$

and for arbitrary z-values

$$v_{2y}(y, z) = \frac{A}{B} \int_0^\infty \cos(ky) \mathrm{e}^{-kz} \mathrm{e}^{-Bk} (1 - kz) \, \mathrm{d}k \tag{A.10a}$$

$$= \frac{A}{B} \frac{(B^3 + 2B^2 z + (y^2 + z^2)B + 2y^2 z)}{B^2 + 2Bz + y^2 + z^2}$$

$$v_{2z}(y, z) = \frac{A}{B} \int_0^\infty \sin(ky) \, \mathrm{e}^{-kz} \mathrm{e}^{-Bk} kz \, \mathrm{d}k \tag{A.10b}$$

$$= \frac{A}{B} \frac{2yz(B + z)}{(B^2 + 2Bz + y^2 + z^2)}.$$

For the cylindrical wire potential, we have that

$$A = -\frac{\lambda_{\mathrm{D}} \epsilon_{\mathrm{s}}}{\eta} \frac{2\phi_0 B}{\mathrm{arccosh}\left(\frac{d}{a}\right)} |\boldsymbol{E}_{\mathrm{ext}\|}|, \qquad B^2 = d^2 - a^2. \tag{A.11}$$

This solution only resembles that of a finite geometry very close to the Lorentzian slip actuation. This is illustrated in figure A.1, where the analytical calculation is shown beside that of a numerical calculation for the finite $H_{\mathrm{ch}} \times W_{\mathrm{ch}} = 160 \times 375 \, \mu\mathrm{m}$ geometry. For the shown simulation, $a = 0.1 \, \mu\mathrm{m}$, $d = 0.2 \, \mu\mathrm{m}$ and $\phi_0 = 1 \, \mathrm{V}$ were chosen. We notice that the qualitative features of the two solutions differ significantly, even for $a, d \ll W_{\mathrm{ch}}, H_{\mathrm{ch}}$. The analytical solution simply shoves fluid from left to right, whereas the fluid flow turns into a roll in the finite geometry. The quantitative features of the high velocity contours are, however, similar.
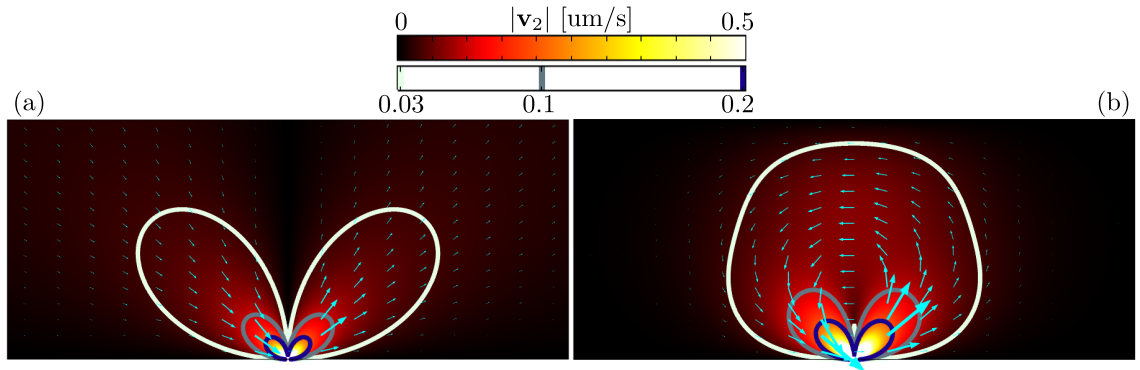
Figure A.1: Flow from a cylindrical wire potential for a finite and infinite geometry. (a) the analytical solution in Eq. (A.10). (b) numerical solution in the finite geometry.

B | Combining sinusoidal modes in ICEO

We consider the ICEO streaming generated by two superimposed sinusoidal modes. From the effective ICEO theory we see that we essentially want to consider

$$\nabla^2 \phi^{\mathrm{b}} = 0, \tag{B.1a}$$

$$\phi^{\mathrm{b}}(\boldsymbol{s}_0) = V_0 w(\boldsymbol{s}_0) + \mathrm{i}\frac{\omega_{\mathrm{D}}}{\omega}\frac{1}{\kappa_{\mathrm{el}}}\partial_\perp \phi^{\mathrm{b}}(\boldsymbol{s}_0), \tag{B.1b}$$

$$\boldsymbol{v}_{\mathrm{slip}}^{\mathrm{ICEO}} = (\boldsymbol{s}_0) = \hat{\boldsymbol{e}}_\| \frac{\epsilon_{\mathrm{f}}\lambda_{\mathrm{D}}}{2\eta}\left(\frac{\omega_{\mathrm{D}}}{\omega}\right)\mathrm{Im}\{\partial_\perp \phi^{\mathrm{b}}(\boldsymbol{s}_0)\partial_\| \phi^{\mathrm{b}*}(\boldsymbol{s}_0)\}. \tag{B.1c}$$

The following constants are defined

$$A_k = \frac{1}{\cosh\left(\frac{k\pi H_{\mathrm{ch}}}{W_{\mathrm{ch}}}\right) + \mathrm{i}\frac{\omega_{\mathrm{D}}}{\omega}\frac{k2\pi}{\kappa_{\mathrm{el}}W}\sinh\left(\frac{k\pi H_{\mathrm{ch}}}{W_{\mathrm{ch}}}\right)}. \tag{B.2}$$

We apply the boundary conditions

$$w(y, \pm H_{\mathrm{ch}}/2) = \left[\sin\left(\frac{n2\pi y}{W_{\mathrm{ch}}}\right) + \mathrm{i}\sin\left(\frac{m2\pi y}{W_{\mathrm{ch}}}\right)\right], \tag{B.3a}$$

$$w(\pm W_{\mathrm{ch}}/2, z) = \mathrm{i}\frac{\omega_{\mathrm{D}}}{\omega}\frac{2\pi}{\kappa_{\mathrm{el}}W_{\mathrm{ch}}}\left[nA_n\cosh\left(\frac{n2\pi z}{W_{\mathrm{ch}}}\right)(-1)^n + \mathrm{i}mA_m\cosh\left(\frac{m2\pi z}{W_{\mathrm{ch}}}\right)(-1)^m\right]. \tag{B.3b}$$

This leads to the following form of the electric bulk potential

$$\phi^{\mathrm{b}}(y, z) = V_0\left[A_n\cosh\left(\frac{n2\pi z}{W_{\mathrm{ch}}}\right)\sin\left(\frac{n2\pi y}{W_{\mathrm{ch}}}\right) + \mathrm{i}A_m\cosh\left(\frac{m2\pi z}{W_{\mathrm{ch}}}\right)\sin\left(\frac{m2\pi y}{W_{\mathrm{ch}}}\right)\right]. \tag{B.4}$$

With this electriv bulk potential, we find the slip velocity

$$\boldsymbol{v}_{\mathrm{slip}}^{\mathrm{ICEO}}(y = \pm H_{\mathrm{ch}}/2, z) = \boldsymbol{0}, \tag{B.5a}$$

$$\boldsymbol{v}_{\mathrm{slip}}^{\mathrm{ICEO}}(y, z = \pm H_{\mathrm{ch}}/2) = \hat{\boldsymbol{e}}_y\frac{\epsilon_{\mathrm{f}}\lambda_{\mathrm{D}}}{2\eta}\left(\frac{\omega_{\mathrm{D}}}{\omega}\right)\left(\frac{2\pi V_0}{W_{\mathrm{ch}}}\right)^2\frac{mn}{2}\mathrm{Re}\{A_n A_m^*\} \tag{B.5b}$$

$$\left[\sinh\left(\frac{(m+n)\pi H_{\mathrm{ch}}}{W_{\mathrm{ch}}}\right)\sin\left(\frac{2\pi y}{W_{\mathrm{ch}}}(m-n)\right)\right.$$

$$\left. + \sinh\left(\frac{(m-n)\pi H_{\mathrm{ch}}}{W_{\mathrm{ch}}}\right)\sin\left(\frac{2\pi y}{W_{\mathrm{ch}}}(m+n)\right)\right].$$

In the case of $|m - n| = 1$, we find a mixture of two sinusoidal modes, where one of them has the desired Rayleigh slip form. For increasing values of m, n, this form becomes more and more dominant. This is illustrated in figure B.1, where the normalised slip velocity is plotted for varying values of m, n. Already at $(m, n) = (2, 3)$, an almost perfect reverse Rayleigh pattern is reached.
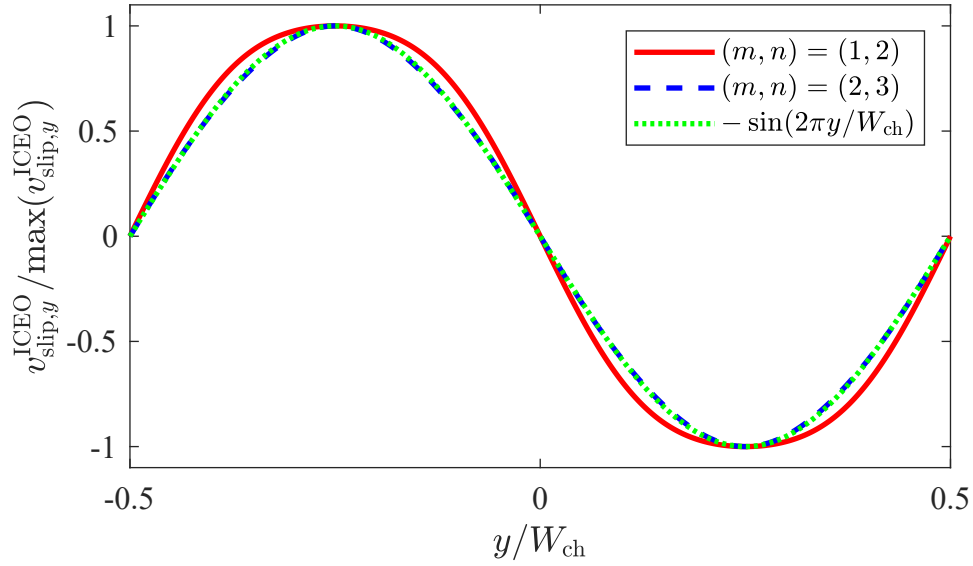

Figure B.1: Normalised slip velocity for sinusoidal mode combinations.
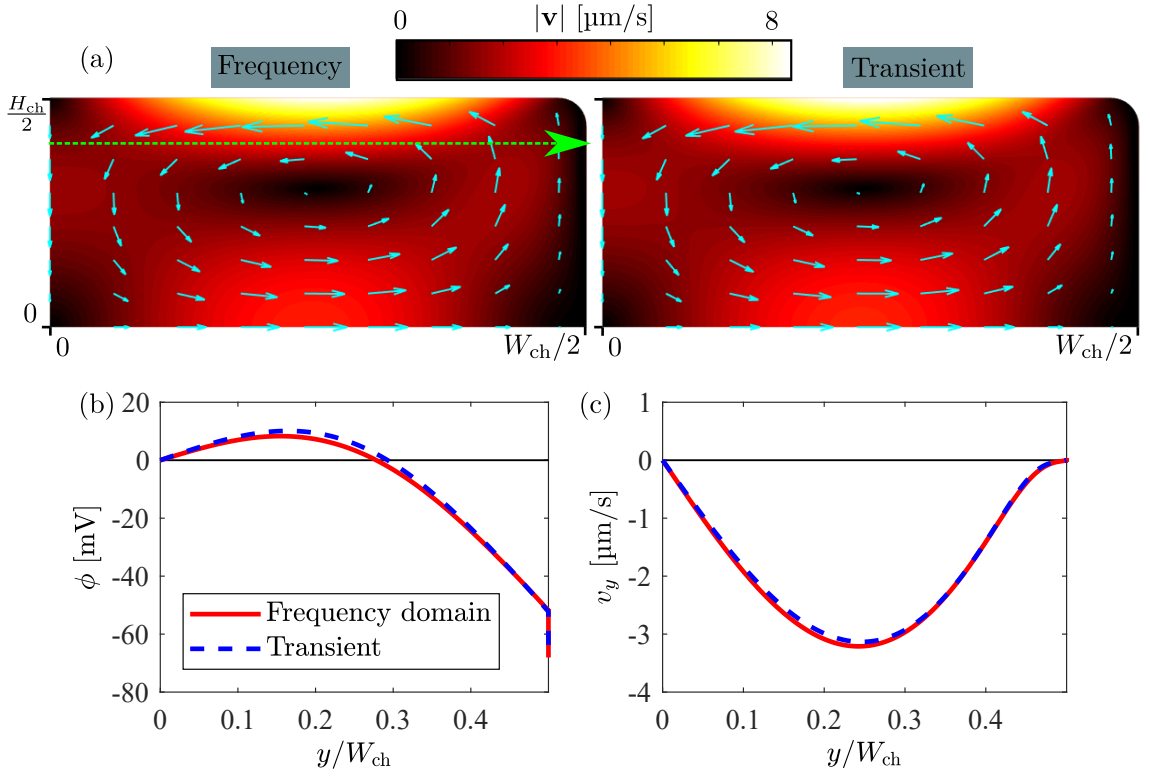
C │ Plot of 75 mV ICEO streaming.

Figure C.1: 75 mV ICEO flow calculated transient and in the frequency domain. (a) fields plots of the velocity field. Both the frequency domain simulation and the time-averaged transient result are shown. Line plots are shown along the green dashed arrow at $z = H/2.5$. (b) the electric potential calculated in frequency domain as well as transient shown at $\omega t = 3T$ (the beginning of the fourth oscillation, corresponding to the real part of the frequency domain $\phi(\boldsymbol{r})$) (c) horizontal component of the time-averaged velocity field calculated in frequency domain as well as transient.

Bibliography

[1] P. Augustsson, C. Magnusson, M. Nordin, H. Lilja, and T. Laurell, *Microfluidic, label-free enrichment of prostate cancer cells in blood based on acoustophoresis.* Anal. Chem. **84**(18), 7954–7962 (2012).

[2] P. Ohlsson, M. Evander, K. Petersson, L. Mellhammar, A. Lehmusvuori, U. Karhunen, M. Soikkeli, T. Seppa, E. Tuunainen, A. Spangar, P. von Lode, K. Rantakokko-Jalava, G. Otto, S. Scheding, T. Soukka, S. Wittfooth, and T. Laurell, *Integrated acoustic separation, enrichment, and microchip polymerase chain reaction detection of bacteria from blood for rapid sepsis diagnostics.* Analytical Chemistry **88**(19), 9403–9411 (2016).

[3] F. Petersson, A. Nilsson, C. Holm, H. Jönsson, and T. Laurell, *Separation of lipids from blood utilizing ultrasonic standing waves in microfluidic channels.* Analyst **129**(10), 938–43 (2004).

[4] J. S. Bach and H. Bruus, *Theory of pressure acoustics with viscous boundary layers and streaming in curved elastic cavities.* J. Acoust. Soc. Am. **144**, 766–784 (2018).

[5] J. S. Bach and H. Bruus, *Bulk-driven acoustic streaming at resonance in closed microcavities.* Phys. Rev. E **100**, 023104 (2019).

[6] R. Barnkob, *Physics of microparticle acoustophoresis.* Ph.D. thesis, Technical University of Denmark (2012).

[7] M. Settnes and H. Bruus, *Forces acting on a small particle in an acoustical field in a viscous fluid.* Phys. Rev. E **85**, 016327 (2012).

[8] A. Ajdari, *Pumping liquids using asymmetric electrode arrays.* Phys Rev E **61**(1), 45–48 (2000).

[9] A. B. D. Brown, C. G. Smith, and A. R. Rennie, *Pumping of water with ac electric fields applied to asymmetric pairs of microelectrodes.* Phys Rev E **63**(1), 016305 (2000).

[10] A. Brask, J. P. Kutter, and H. Bruus, *Long-term stable electroosmotic pump with ion exchange membranes.* Lab Chip **5**, 730–738 (2005).

[11] A. Brask, D. Snakenborg, J. P. Kutter, and H. Bruus, *Ac electroosmotic pump with bubble-free palladium electrodes and rectifying polymer membrane valves*. Lab Chip **6**, 280–288 (2006).

[12] P. Glynne-Jones and M. Hill, *Acoustofluidics 23: acoustic manipulation combined with other force fields*. Lab Chip **13**, 1003–1010 (2013).

[13] J. D. Adams, P. Thevoz, H. Bruus, and H. T. Soh, *Integrated acoustic and magnetic separation in microfluidic channels*. Appl Phys Lett **95**(25), 254103–1 (2009).

[14] J. S. Bach and H. Bruus, *Suppression of acoustic streaming in shape-optimized channels*. Phys. Rev. Lett. **124**, 214501 (2020).

[15] J. T. Karlsen, W. Qiu, P. Augustsson, and H. Bruus, *Acoustic streaming and its suppression in inhomogeneous fluids*. Phys. Rev. Lett. **120**(5), 054501 (2018).

[16] H. Bruus, *Theoretical Microfluidics* (Oxford University Press, Oxford) (2008).

[17] COMSOL Multiphysics 5.4. http://www.comsol.com (2018).

[18] H. Bruus, *Numerical studies in physics* (Technical University of Denmark, http://www.staff.dtu.dk/bruus) (2018).

[19] P. B. Muller, R. Barnkob, M. J. H. Jensen, and H. Bruus, *A numerical study of microparticle acoustophoresis driven by acoustic radiation forces and streaming-induced drag forces*. Lab Chip **12**, 4617–4627 (2012).

[20] P. B. Muller, M. Rossi, A. G. Marin, R. Barnkob, P. Augustsson, T. Laurell, C. J. Kähler, and H. Bruus, *Ultrasound-induced acoustophoretic motion of microparticles in three dimensions*. Phys. Rev. E **88**(2), 023006 (2013).

[21] P. B. Muller and H. Bruus, *Numerical study of thermoviscous effects in ultrasound-induced acoustic streaming in microchannels*. Phys. Rev. E **90**(4), 043016 (2014).

[22] P. B. Muller and H. Bruus, *Theoretical study of time-dependent, ultrasound-induced acoustic streaming in microchannels*. Phys. Rev. E **92**, 063018 (2015).

[23] N. R. Skov, J. S. Bach, B. G. Winckelmann, and H. Bruus, *3D modeling of acoustofluidics in a liquid-filled cavity including streaming, viscous boundary layers, surrounding solids, and a piezoelectric transducer*. AIMS Mathematics **4**, 99–111 (2019).

[24] Lord Rayleigh, *On the circulation of air observed in Kundt's tubes, and on some allied acoustical problems*. Philos. Trans. R. Soc. London **175**, 1–21 (1884).

[25] R. H. D. Narottam P. Bansal, N. P. Bansal, *Handbook of Glass Properties* (Elsevier LTD) (1986).

[26] J. N. Israelachvili, *4 - interactions involving polar molecules*. In J. N. Israelachvili (ed.), *Intermolecular and Surface Forces (Third Edition)*, 71 – 90 (Academic Press, San Diego), third edition edn. (2011).

[27] John D'Errico. Matlab file exchange (2020), https://www.mathworks.com/matlabcentral/fileexchange/8277-fminsearchbnd-fminsearchcon, accessed 11 March 2020.

[28] R. T. Davies, J. Kim, S. C. Jang, E. J. Choi, Y. S. Gho, and J. Park, *Convergence properties of the nelder - mead simplex method in low dimensions.* Society for Industrial and Applied Mathematic **9**(1), 112–147 (1998).

[29] C. P. Nielsen and H. Bruus, *Sharp-interface model of electrodeposition and ramified growth.* Phys. Rev. E **92**, 042302 (2015).

[30] M. S. Kilic, M. Z. Bazant, and A. Ajdari, *Steric effects in the dynamics of electrolytes at large applied voltages. i. double-layer charging.* Phys Rev E **75**(2), 021502 (2007).

[31] D. R. Lide, *CRC Handbook of Chemistry and Physics.* (Internet Version 2011) (CRC Press/Taylor and Francis, Boca Raton, FL), 97th edn. (2016).

[32] B. Kirby and E. Hasselbrink, *Zeta potential of microfluidic substrates: 1. theory, experimental techniques, and effects on separations.* Electrophoresis **25**, 187–202 (2004).

[33] M. B. Andersen, J. Frey, S. Pennathur, and H. Bruus, *Surface-dependent chemical equilibrium constants and capacitances in bare and 3-cyanopropyldimethylchlorosilane coated silica nanochannels.* J Colloid Interface Sci **353**, 301–310 (2011).

[34] H. Liu, S. Dharmatilleke, D. Maurya, and A. Tay, *Dielectric materials for electrowetting-on-dielectric actuation.* Microsystem Technologies **16**, 449–460 (2009).

[35] N. G. Green, A. Ramos, A. González, H. Morgan, and A. Castellanos, *Fluid flow induced by nonuniform ac electric fields in electrolytes on microelectrodes. III. observation of streamlines and numerical simulation.* Phys Rev E **66**(2), 026305 (2002).

[36] N. Mortensen, L. Olesen, L. Belmon, and H. Bruus, *Electrohydrodynamics of binary electrolytes driven by modulated surface potentials.* Physical review. E, Statistical, nonlinear, and soft matter physics **71**, 056306 (2005).

[37] COMSOL Multiphysics, *BDF, Generalized Alpha, and Runge-Kutta Methods.* https://www.comsol.com/support/knowledgebase/1062 (2020).